



Università degli Studi di Ferrara

DOTTORATO DI RICERCA IN
SCIENZE DELL'INGEGNERIA

CICLO XXIII

COORDINATORE Prof. Trillo Stefano

MONITORING OF THE THRESHING PROCESS QUALITY BY
USING ADVANCED VIBRO-ACOUSTIC INDICATORS

Settore Scientifico Disciplinare ING-IND/13

Dottorando
Dott. Fiorati Stefano

Tutore
Prof. Dalpiaz Giorgio

Anni 2008/2010



Università degli Studi di Ferrara

DOTTORATO DI RICERCA IN
SCIENZE DELL'INGEGNERIA

CICLO XXIII

COORDINATORE Prof. Trillo Stefano

MONITORING OF THE THRESHING PROCESS QUALITY BY
USING ADVANCED VIBRO-ACOUSTIC INDICATORS

Settore Scientifico Disciplinare ING-IND/13

Dottorando

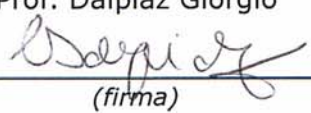
Dott. Fiorati Stefano



(firma)

Tutore

Prof. Dalpiaz Giorgio



(firma)

Anni 2008/2010

Università degli Studi di Ferrara
Engineering Department in Ferrara

Dottorato di Ricerca in Scienze dell'Ingegneria
XXIII ciclo

Doctoral Program: Engineering
Curriculum: Industrial Engineering
Branch of study: Mechanics of Machines

Title: Monitoring of the threshing process quality by using advanced
vibro-acoustic indicators

Author: Ing. Stefano Fiorati

Supervisor: Prof. Giorgio Dalpiaz

Printed: March 2011

PhD Coordinator

Prof. Stefano Trillo

Università degli Studi di Ferrara

PhD Jury

Prof. Giorgio Dalpiaz

Università degli Studi di Ferrara, Italy

Prof. Franco Bonollo

Università degli Studi di Padova, Italy

Prof. Gian Luca Morini

Università degli Studi di Bologna, Italy

Prof. Dr. Ir. Paul Sas

Katholieke Universiteit Leuven, Belgium

Final exam

2011 March, 28th

Riassunto

L'argomento affrontato in questa tesi riguarda l'uso di tecniche avanzate di processamento del segnale vibro-acustico per il monitoraggio del processo di trebbiatura in macchine mietitrebbia a flusso assiale. Questa ricerca rappresenta uno step importante verso lo sviluppo di un sistema di controllo on-line finalizzato a massimizzare l'efficienza del processo e la qualità del prodotto trebbiato.

Attraverso l'utilizzo di tecniche avanzate di analisi del segnale è possibile analizzare il legame che intercorre tra la distribuzione di materiale nel gruppo di trebbiatura e la risposta vibro-acustica della macchina stessa. Entrando nello specifico, il processo di trebbiatura è principalmente dovuto a due meccanismi: la trebbiatura del materiale che impatta il controbattitore e il cosiddetto "grain over grain effect". L'obiettivo di questa ricerca è quello di usare la firma vibro-acustica del gruppo di trebbiatura per dare un'interpretazione dettagliata dei due meccanismi caratteristici del processo. In particolare, tali meccanismi vengono descritti utilizzando l'approccio ciclostazionario utile a valutare i contenuti ciclostazionari del primo e secondo ordine del segnale di vibrazione.

I risultati ottenuti mostrano che gli indicatori estratti dall'analisi nei domini temporale ed angolare e dall'approccio ciclostazionario sono ben correlati con i parametri operativi e di efficienza della macchina. Tali indicatori potrebbero essere usati per lo sviluppo di un sistema di controllo on-line del processo di trebbiatura.

Abstract

This PhD thesis concerns the vibro-acoustic monitoring of the threshing process in an axial flow harvesting machine. This research is a step towards the development of online control systems finalized to maximize the process efficiency and the product quality.

By using different signal processing tools it is possible to analyse the link between sound/vibration and material distribution in the threshing unit. In more details, the threshing process is mainly given by two principal mechanisms: the threshing between kernels and concave and “grain over grain” effect. The goal of this research is to use vibro-acoustic signature in order to interpret in detail these two mechanisms of the threshing process. In particular, they have been explained by means of the cyclostationary approach useful to evaluate the first and second order cyclostationary contents of the signal.

Moreover, the presented results show that some features obtained from the time and angular domains and from the cyclostationary approach are well correlated to the efficiency and operational parameters. Thus, they could be used for the development of an online control system.

Preface

I started my PhD in Mechanical Vibration in the 2008 after the discussion of my master thesis in Mechanical Vibration developed under the supervision of Prof. Ing. Giorgio Dalpiaz.

The first activity that I carried out, in the first 6 months of my PhD has dealt with the modal analysis of marine Diesel engines with the aim to obtain the inertia properties of these bodies. This activity is described in the following publications:

- E. Mucchi, S. Fiorati, R. Di Gregorio, G. Dalpiaz, “**Determining the rigid-body inertia properties of cumbersome systems: comparison of techniques in time and frequency domain**”. Paper n. 32, IMAC-XXVII, Conference & Exposition on Structural Dynamics, 2009, Orlando (USA).
- E. Mucchi, S. Fiorati, R. Di Gregorio, G. Dalpiaz, “**Determining the rigid-body inertia properties of cumbersome systems: comparison of techniques in time and frequency domain**”. EXPERIMENTAL TECHNIQUES; ISSN: 0732-8818, DOI: 10.1111/j.147-1567.2009.00603.

At the same time, I had a short experience carried out in cooperation with VM Motori (Cento, Ferrara, Italy), on the vibro-acoustic signature analysis of industrial Diesel engine. The goal was to study the effect of the gear quality over the vibro-acoustic signature of the gear train.

I spent 15 months of my doctoral training at the Department of Mechanical Engineering at KUL (Katholieke Universiteit Leuven) in Leuven (Belgium) within the Noise and Vibration group. The topic of this research activity, was the analysis of the relationship between the threshing process in an axial flow harvesting machine and its vibro-acoustic behaviour.

Moreover, the detailed physical explanation of the threshing process mechanisms and the correlation among vibro-acoustic features and “efficiency” parameters was another goal of the research.

The results of this activity are summarised in this thesis and in the following technical report and publication:

- S. Fiorati, “**Condition monitoring of the threshing process in harvesting machine by means of vibro-acoustic analysis**”. Technical report 2009, Katholieke Universiteit Leuven, Department of Mechanical Engineering, PMA Division, Noise and Vibration Group.
- S. Delvecchio, S. Fiorati, B. Missotten, P. Sas, “**Vibro-acoustic signature analysis of the threshing process in harvesting machine**”, Paper n. 105, ISMA International Conference on Noise and Vibration Engineering, 2010, Leuven (Belgium).

Another research activity I carried out during the last 9 months concerns the multibody dynamic model of a planar manipulator (MP) in cooperation with FUTURA Robotica (Alseno PC). The model takes into account the mass and inertia properties of all the bodies. Moreover, by finite element analysis of the frame, the flexibility is introduced into the model in order to achieve greater accuracy. The model has been assessed by experiments and it could be used in order to interpret the dynamic behaviour of the system for design optimization of the robot.

Finally, I wish to give a special and sincere thanks to Prof. Ing. Giorgio Dalpiaz, my supervisor, for his guidance during my PhD studies. I would like to give a very special thanks to Prof. Dr. Ir. Paul Sas for his help and trust he gave me during the long period I spent at KUL. Moreover, I wish to thank Dr. Ir. Bart Missotten from CNH, all the academic stuff and colleagues from the Department of Biomechanics Engineering of KUL for their fundamental co-operation.

The last but not least important is the sincere thanks to my friend and colleague Dr. Simone Delvecchio who proposed me to continue his research activity on the combine harvester.

Contents

| | |
|---|--------------|
| Riassunto | vii |
| Abstract | ix |
| Preface | xi |
| Contents | xv |
| List of Figures | xvii |
| List of Tables | xxi |
| List of Abbreviations | xxiii |
| Chapter 1 | |
| INTRODUCTION | 25 |
| 1.1 State of the art and research objective..... | 25 |
| 1.2 Vibro-acoustic condition monitoring | 27 |
| 1.2.1 Time domain techniques | 28 |
| 1.2.2 Cyclostationary approach..... | 29 |
| 1.3 Overview of the Thesis..... | 29 |
| Chapter 2 | |
| THE COMBINE HARVESTERS AND THE EXPERIMENTAL SET-UP | 31 |
| 2.1 Introduction | 31 |
| 2.2 The non-conventional harvesting machine | 31 |
| 2.3 Threshing zone: description of the mechanical parts | 35 |
| 2.4 Process efficiency indicators | 38 |
| 2.4.1 Grain tank sample..... | 38 |
| 2.4.2 Grain losses..... | 40 |
| 2.5 Experimental set-up in the combine harvester | 44 |
| 2.5.1 Sensor overview | 44 |
| 2.6 Indoor and outdoor test campaigns | 48 |

| | |
|---|------------|
| Chapter 3 | |
| SIGNAL PROCESSING TECHNIQUES..... | 51 |
| 3.1 Introduction..... | 51 |
| 3.2 Cyclostationary approach..... | 52 |
| 3.2.1 Background theory..... | 52 |
| 3.2.2 Indicators of Cyclostationarity..... | 56 |
| 3.3 Sound quality metrics..... | 57 |
| 3.3.1 Stationary Loudness ISO 532 B..... | 57 |
| 3.3.2 Aures's model of Tonality..... | 64 |
| 3.4 Approximate Entropy (AppEn)..... | 67 |
| 3.5 Application to a synthesized signal..... | 69 |
| 3.5.1 Cyclostationary approach..... | 71 |
| 3.5.2 Aures's tonality algorithm..... | 74 |
| 3.5.3 Approximate entropy algorithm..... | 79 |
| Chapter 4 | |
| VIBRO-ACOUSTIC ANALYSIS OF THE THRESHING PROCESS..... | 85 |
| 4.1 Introduction..... | 85 |
| 4.2 Time domain features..... | 86 |
| 4.2.1 Influence of the capacity..... | 87 |
| 4.2.2 Influence of the concave distance..... | 89 |
| 4.3 Preliminary angular domain analysis..... | 98 |
| 4.3.1 Time Synchronous Average (TSA) estimation..... | 98 |
| 4.3.2 Identification of the periodical interaction events..... | 100 |
| 4.3.3 Effect of the crop in the threshing zone..... | 104 |
| 4.4 Threshing process interpretation by means of the cyclostationary approach..... | 105 |
| 4.5 Correlation between signal features and efficiency parameters..... | 112 |
| 4.5.1 Time domain features..... | 113 |
| 4.5.2 Angular domain features..... | 117 |
| Chapter 5 | |
| CONCLUSIONS..... | 131 |
| References..... | 137 |

List of Figures

| | |
|--|----|
| Fig. 1-1 - An axial flow rotary combine utilizing twin rotors: (1) rotor, (2) rasp bars, (3) threshing concave, (4) separating concave. | 27 |
| Fig. 2-1 - Frontal rotors in conventional combine harvesters. | 32 |
| Fig. 2-2 – Process diagram of a combine harvester [16]. | 33 |
| Fig. 2-3 - An axial flow rotary combine utilizing twin rotors: (1) rotor, (2) rasp bars, (3) threshing concave, (4) separating concave, (4) discharge beater, (6) beater grate, (7) cleaning shoe, (8) feeder housings, (9) tailings auger [16]. | 33 |
| Fig. 2-4 – Field tests: concave grate for wheat crop (a) and corn crop (b). | 35 |
| Fig. 2-5 – Threshing unit: mechanical parts involved in the threshing process. | 36 |
| Fig. 2-6 – Threshing unit: threshing and separation zones..... | 37 |
| Fig. 2-7 – Parts of the plant..... | 41 |
| Fig. 2-8 – Product of the threshing process. | 41 |
| Fig. 2-9 – Stationary tests: measure of threshing and separation losses. | 43 |
| Fig. 2-10 –Field tests: measurement of the total loss. | 43 |
| Fig. 2-11 – Field tests: measurement of the threshing loss..... | 43 |
| Fig. 2-12 – Test rig: accelerometers and microphones mounted on the machine. | 45 |
| Fig. 2-13 – magnetic pick up and triaxial accelerometer concave middle. | 46 |
| Fig. 2-14 – the feedrate sensor (white rectangle in (a)) and the feedrate signal measured in (b). | 47 |
| Fig. 2-15 – Indoor test rig: (a) harvesting machine, (b) belt conveyor. .. | 48 |
| Fig. 2-16 – Outdoor tests condition: (a) barley field, (b) corn field..... | 49 |
| Fig. 2-17 – Different varieties of corn crop | 49 |
| Fig. 3-1 - Loudness calculation according to Zwicker’s method [8]. | 58 |
| Fig. 3-2 - General procedures for calculating stationary loudness according to method B. | 61 |
| Fig. 3-3 - loudness function of 1 kHz tone (solid line) and uniform-exciting noise (dotted); loudness is given as a function of the sound pressure level. Approximations using power laws are indicated as broken and as dashed-dotted lines together with their corresponding Equations [8]. | 63 |

| | |
|--|----|
| Fig. 3-4 - Stationary Loudness test spectrum for a pure tone at 1 kHz 40 dB with Matlab code. | 64 |
| Fig. 3-5 - Aures's model of tonality [11]. | 65 |
| Fig. 3-6 – Steps in the Approximate Entropy calculation [13]. | 68 |
| Fig. 3-7 - Synthesized signal: (a) $x_p(t)$, (b) $x_R(t)$, (c) $x_s(t)$ | 70 |
| Fig. 3-8 – Influence of the amplitude value: A(i)x1 (test A): (a) numerator ICS _{1x} , (b) numerator ICS _{2x} , and A(i)x3 (test G): (c) numerator ICS _{1x} , (d) numerator ICS _{2x} | 72 |
| Fig. 3-9 – Influence of the R value: R = 0.1 (test A): (a) numerator ICS _{1x} , (b) numerator ICS _{2x} , (c) and R = 0.9 (test E): (c) numerator ICS _{1x} , (d) numerator ICS _{2x} | 73 |
| Fig. 3-10 – Aures's algorithm tested on the signal model..... | 74 |
| Fig. 3-11 - Tonality algorithm results for two frequency resolution values: (a) 1 Hz, (b) 10 Hz. | 75 |
| Fig. 3-12 – Tonality algorithm results in function of the value of Equation (3.28): (a) 1, (b) 10..... | 76 |
| Fig. 3-13 - Tonality algorithm results in function of the random noise gain G: (a) G = 1, (b) G =3..... | 78 |
| Fig. 3-14 - Tonality algorithm results in function of the amplitude A(i): (a) A(i)x0.5, (b) A(i)x3..... | 78 |
| Fig. 3-15 – Synthesized signal: influence of the amplitude $A(i)$ (see Tab. 3-4) (a) test A, (b) test G. | 80 |
| Fig. 3-16 - Synthesized signal: influence of the coefficient R (see Tab. 3-4) (a) test A, (b) test E..... | 81 |
| Fig. 3-17 - Synthesized signal: influence of the random noise gain G (see Tab. 3-4) (a) test A, (b) test C. | 82 |
| Fig. 3-18 – Synthesized signals: (a) without bursts, (b) with bursts..... | 83 |
| Fig. 3-19 – Effect of k on the AppEn values for two amplitude values of the synthesized signal with $G = 1$ and $R = 0.1$ | 84 |
| Fig. 3-20 - Effect of k on the AppEn values for three gain values of the synthesized signal with A(i)x1 and $R = 0.1$ | 84 |
| Fig. 3-21 - Effect of k on the AppEn values for three different coefficient R values of the synthesized signal with A(i)x1 and $G = 1$ | 84 |
| Fig. 4-1 – Features vs. capacity (field nr. 2): (a) Av. RMS at middle position, (b) Av. Loudness cabin microphone, (c) Av. Tonality cabin microphone. | 88 |
| Fig. 4-2 – Av. RMS vs. concave distance: (a) Av. RMS at middle position, (b) wheat field tests nr. 1 and (c) wheat field tests nr. 2. | 92 |

| | |
|---|-----|
| Fig. 4-3 – Time signals comparison for two concave distance values: (a) field tests nr. 1 (runs E and I), (b) field tests nr. 2 (runs A and D), (c) STFT of the signal depicted in (b)..... | 93 |
| Fig. 4-4 - Features vs. concave distance (field nr. 2): (a) Av. Loudness cabin microphone, (b) Av. Tonality cabin microphone, (c) AppEn at the middle position..... | 94 |
| Fig. 4-5 – Threshing microphone, runs at 1420 rpm and 400 V average feedrate: (a) Tonality vs. concave distance, (b) tonality algorithm results for the runs marked by the arrows. | 95 |
| Fig. 4-6 – Cabin microphone, runs at 1420 rpm and 400 V average feedrate: (a) Tonality vs. concave distance, (b) tonality algorithm result for the run marked by the arrow..... | 96 |
| Fig. 4-7 – Sound pressure level at 15 mm concave distance: (a) process microphone, (b) cabin microphone. | 97 |
| Fig. 4-8 – Tachometer signals: (a) 1 pulse/rev sampled at 6 kHz, (b) 100 pulse/rev sampled at 51 kHz. | 99 |
| Fig. 4-9 – Instantaneous speed fluctuations..... | 100 |
| Fig. 4-10 – Rotor sections. | 100 |
| Fig. 4-11 – Field tests rotor drawing. | 101 |
| Fig. 4-12 - Field test nr. 1, test run: (a) rasp bars signals rear section and (b) front section. | 102 |
| Fig. 4-13 – Field test nr. 1 test run: (a) concave middle radial TSA signal, (b) threshing microphone middle TSA signal, (c) threshing microphone right TSA signal..... | 103 |
| Fig. 4-14 – Comparison based on TSA signals with and without crop for field tests (a) concave middle radial, (b) threshing microphone right. | 104 |
| Fig. 4-15 – RMS TSA vs. concave distance: (a) field test nr. 1 and (b) field test nr. 2. | 106 |
| Fig. 4-16 – Front view of the threshing zone: (a) minimum concave distance, (b) maximum concave distance..... | 106 |
| Fig. 4-17 – Influence of the concave distance on the TSA signal: (a) field test nr.1 (A, B and D), (b) field tests nr. 2 (E, G and I) and (c) FFT of the TSA signals in (b)..... | 108 |
| Fig. 4-18 – Material direction inside the threshing zone..... | 109 |
| Fig. 4-19 – Material distribution for: (a) minimum concave distance and (b) maximum concave distance. | 110 |
| Fig. 4-20 – Pressure given by the material compression on the concave. | 111 |
| Fig. 4-21 – Cyclic power: (a) field test nr. 1 and (b) field test nr. 2. | 111 |
| Fig. 4-22 – Variation of un-threshed grains in an axial unit..... | 113 |

| | |
|--|-----|
| Fig. 4-23 - Efficiency parameter: threshing loss for the field nr. 1. (a) RMS vs. concave distance and (b) RMS vs. threshing loss with $R^2 = 0.90$ | 114 |
| Fig. 4-24 - Efficiency parameter: threshing loss for the field nr. 2. (a) RMS vs. concave distance and (b) RMS vs. threshing loss with $R^2 = 0.45$ | 115 |
| Fig. 4-25 - Efficiency parameter: broken grain for the corn field nr. 1: Av. RMS vs. broken grain with $R^2 = 0.95$ | 116 |
| Fig. 4-26 - Efficiency parameter: broken grain for the corn field nr. 2: Av. RMS vs. broken grain with $R^2 = 0.87$ | 117 |
| Fig. 4-27 - Efficiency parameter: threshing loss for the field nr. 1. (a) RMS TSA vs. concave distance and (b) RMS TSA vs. threshing loss with $R^2 = 0.66$ | 119 |
| Fig. 4-28 - Efficiency parameter: threshing loss for the field nr. 2: (a) RMS TSA vs. concave distance and (b) RMS TSA vs. threshing loss with $R^2 = 0.80$ | 120 |
| Fig. 4-29 - Influence of the feedrate over the minimum point detected on the RMS correlation vs. concave distance, (a) wheat field tests, (b) barley field tests. | 121 |
| Fig. 4-30 - Efficiency parameter: broken grain for the corn field nr. 1: RMS TSA vs. broken grain with $R^2 = 0.96$ | 122 |
| Fig. 4-31 - Efficiency parameter: broken grain for the corn field nr. 2: RMS TSA vs. broken grain with $R^2 = 0.86$ | 123 |
| Fig. 4-32 - Efficiency parameter: threshing loss for the field nr. 1. (a) ICS_{1x} vs. concave distance, (b) ICS_{2x} vs. concave distance, (c) $ICS_{1x} - ICS_{2x}$ vs. threshing loss with $R^2 = 0.57$ and 0.58 | 126 |
| Fig. 4-33 - Efficiency parameter: threshing loss for the field nr. 2. (a) ICS_{1x} vs. concave distance, (b) ICS_{2x} vs. concave distance, (c) $ICS_{1x} - ICS_{2x}$ vs. threshing loss with $R^2 = 0.95$ and 0.16 | 127 |
| Fig. 4-34 - Efficiency parameter: threshing loss for the field nr. 1. (a) ICS_{1x} vs. concave distance, (b) ICS_{2x} vs. concave distance, (c) $ICS_{1x} - ICS_{2x}$ vs. broken grain with $R^2 = -0.73$ and 0.22 | 128 |
| Fig. 4-35 - Efficiency parameter: threshing loss for the field nr. 2. (a) ICS_{1x} vs. concave distance, (b) ICS_{2x} vs. concave distance, (c) $ICS_{1x} - ICS_{2x}$ vs. threshing loss with $R^2 = -0.63$ and 0.7 | 129 |

List of Tables

| | |
|--|-----|
| Tab. 2-1 - Different combine configurations for different types of crop [15]. | 39 |
| Tab. 3-1 - Parameters related to the test signal. | 70 |
| Tab. 3-2 – Synthesized signal parameters and ICS values. | 71 |
| Tab. 3-3 - Tonality values for simulated signals with noise amplitude increasing. | 78 |
| Tab. 3-4 - AppEn values of test signal under various parameters. | 79 |
| Tab. 4-1 – Order tracking parameters. | 99 |
| Tab. 4-2 - Machine settings wheat field tests. | 113 |
| Tab. 4-3 – Machine settings corn field tests. | 116 |
| Tab. 4-4 – Comparison between R^2 values from correlation in the time and angular domains. | 118 |
| Tab. 4-5 – Comparison between R^2 values from correlation in the time and angular domains. | 122 |
| Tab. 4-6 - Signal parameters and ICS values. | 124 |
| Tab. 4-7 - R^2 values from RMS and ICS correlation. | 125 |
| Tab. 4-8 – R^2 values from RMS and ICS correlation. | 125 |

List of Abbreviations

| | |
|-------|--------------------------------|
| AppEn | Approximate Entropy |
| FFT | Fast Fourier Transform |
| ICS | Indicator of Cyclostationarity |
| MIP | Mean Instantaneous Power |
| PSD | Power Spectral Density |
| RMS | Root Mean Square |
| TSA | Time Synchronous Average |

INTRODUCTION

1.1 State of the art and research objective

This PhD thesis deals with the condition monitoring of the threshing process in combine harvesters by means of vibration signature techniques. This research is a step towards the development of online control systems for these machines, able to adjust the machine setting in order to maximize the process efficiency. In this context, several outdoor measurements have been performed in various operational conditions in order to pick up a big amount of data, used to interpret the mechanical phenomena and to establish the correlations between signal parameters and operational/efficiency parameters.

In literature there have been many developments in the use of vibration measurements and analysis for the condition monitoring of rotating machinery (i.e. gears, bearings and Diesel engines) while in operation [1]-[2] and [3]. In this thesis, the subject is still a rotating machine, but here the aim is the monitoring of the threshing process performed in order to automate the process control and maximize its efficiency. Published studies on this topic are not numerous: only works [4], [5] can be found.

The aim of these previous works is to verify if non-redundant features physically related to the threshing process can be extracted by means of the analysis of the vibro-acoustic signature and can provide information about the influence of the process operational parameters, namely:

- rotor speed: rpm of the two counter rotating rotors;
- concave distance: radial distance between rotor and concave;
- capacity: amount of crop processed.

Furthermore the features extracted from time domain signals are used, as first tentative, in order to predict the efficiency parameters of the threshing process. In particular, the concave vibration has been proved to be well correlated to the concave distance (i.e. radial distance between rotor and concave in Fig. 1-1) that is tuneable by the user during threshing operations.

The aim of this thesis is not only to confirm the results obtained in [4] and [5] but to point out the effects of the different excitation sources due to the threshing process.

In particular, the use of the cyclostationary approach combined with the angular domain analysis arises from the need to understand more in detail the two characteristic mechanisms of the threshing process (that influence the machine efficiency): (1) the threshing between kernels and concave and (2) the “grain over grain” effect.

Taking advantage of the above mentioned analysis, it is possible to obtain simple metrics related to the efficiency of the process, such as Root Mean Square (RMS) evaluated in the time and angular domains and Indicator of Cyclostationarity (ICS_{nx}) outlined in [6] and [7].

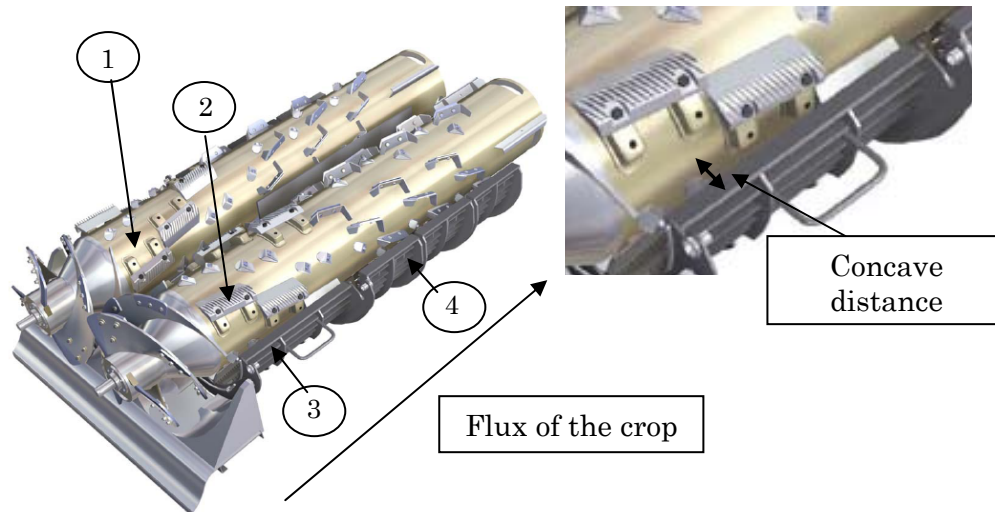


Fig. 1-1 - An axial flow rotary combine utilizing twin rotors: (1) rotor, (2) rasp bars, (3) threshing concave, (4) separating concave.

1.2 Vibro-acoustic condition monitoring

The vibrations and noise measured on operating machines contain much information about their condition. Thus, the vibro-acoustic analysis is a way of getting information from the inside of operating machines without having to shut them down. Generally, the signal processing techniques are used in the field of the condition monitoring of rotating machinery for detecting and diagnosing faults as reported in 0. In the case of the combine harvesters, the changes in the vibro-acoustic signature can be used to understand the physics of the process in order to improve the efficiency of the machine.

In general machine condition monitoring involves three main steps:

- acquisition of the signals by means of accelerometers and microphones;
- post-processing of the data collected in order to extract the part of the signal related to the process under investigation (i.e. digital filtering and selection of the time histories);
- application of signal processing techniques.

There are a large number of signal processing techniques that can be used in order to obtain interesting information from the measured vibro-acoustic signals. In this thesis, the signals measured in harvester machines are processed according to two approaches – time domain and cyclostationary techniques – that are outlined in the following paragraphs.

1.2.1 Time domain techniques

The features extracted from the time domain signals have been applied in [4] and [5] in order to achieve information about the influence of the operational parameters of the combine harvester (i.e. rotor speed, concave distance and amount of crop processed). In order to confirm the results depicted in [4] and [5], and provide information about the process, the following features are extracted from the signals:

- Root Mean Square (RMS) reflecting the energy of the signal;
- Sound Quality metrics (see [8], [9], [10] and [11]) such as Loudness and Tonality, in order to keep into account the human ear non-linearity;
- Approximate Entropy (AppEn), outlined in [12] and [13], which is a statistical parameter that quantifies the regularity of a time series in multiple dimensions.

Since the time domain features do not permit to separate the effects of the characteristic mechanisms of the threshing process, the cyclostationary approach has been introduced.

1.2.2 Cyclostationary approach

In the case that a signal presents periodic energy variations, synchronous with the machine cycle, a particular class of non-stationary signals can be defined: the cyclostationary signals [6]-[14]. The conventional spectral analysis could be not sufficient to reveal the presence of periodicity. Thus, the hidden periodicity could be revealed by investigating how the signal energy is propagating in time [6].

In practice, since the threshing unit of the combine harvester is a rotating machine, the hidden periodicities are related to the rotor angle instead of the time. As consequence, the use of the angular domain (i.e. Time Synchronous Average) gives a detailed description of the threshing process and permits to separate its different mechanisms.

Moreover, the author takes advantages of the cyclostationary approach to obtain simple metrics that can be related to the first and the second cyclostationary contents of the signal.

1.3 Overview of the Thesis

Chapter 2 gives a description of the non-conventional harvesting machine and in particular of the so-called “threshing unit”, in order to have an overview of the mechanical parts involved in the threshing process. Then, the description of the efficiency parameters is reported: these indicators are used to characterise the machine performances. Moreover, a short explanation about the efficiency parameter estimation is reported. Finally, the test set-up is illustrated; the vibro-acoustic sensors and the ones used to acquire the so-called operational parameters (i.e. capacity, rotor speed and ground speed) are listed.

Chapter 3 presents the theoretical background and properties of the signal processing techniques applied in this research, in order to point out their limits and capabilities in obtaining useful information from the threshing unit.

As introduced in the previous paragraphs, time domain techniques and cyclostationary techniques in the angle domain have been considered. Finally, all the techniques have been applied to a synthesized signal reflecting the physics of the threshing process, in order to verify their effectiveness.

In **Chapter 4** the results achieved in applying different signal processing techniques to the real vibro-acoustic signals are reported, as well as their sensitivity to the threshing process parameters.

On one hand, a detailed physical explanation of the mechanisms occurring during the threshing process is given by means of the cyclostationary approach. On the other hand, the correlations between signal features and efficiency/operational parameters are studied with the aim of selecting the features most strongly correlated to the efficiency of the threshing process.

Finally the conclusions and the future perspectives are outlined in **Chapter 5**.

THE COMBINE HARVESTERS AND THE EXPERIMENTAL SET-UP

2.1 Introduction

The purpose of grain harvesting is to collect cereal grass from the field and separate grains from the rest of the crop material in a timely manner with minimum grain loss while maintaining highest grain quality. The methods and equipment used for harvesting depend upon the type of grain crop, planting method, and climate. The most important grain crops are rice, wheat, corn, soybeans, barley, oats, sorghum, and dry beans (navy beans, pinto beans, etc.). Many other grain crops, such as oil-seed crops, are harvested using the methods and equipment described in this chapter. For the experiments (field and stationary tests) of this PhD a New Holland CR combine harvester was used [15].

2.2 The non-conventional harvesting machine

The combine harvester, is a machine that "combines" the tasks of harvesting, threshing, and cleaning grain plants [16]. The desired result is the seed or grain (including corn, soybeans, flax, oats, wheat, or rye among others).

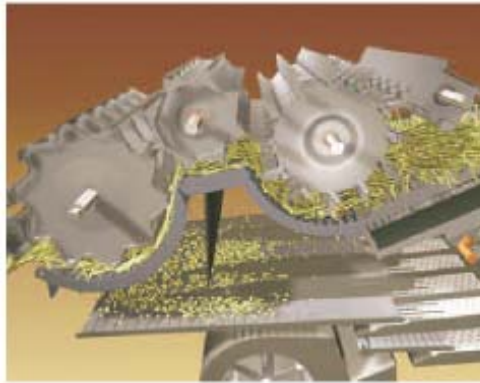


Fig. 2-1 - Frontal rotors in conventional combine harvesters.

For a considerable time, combine harvesters with conventional design have been used (see Fig. 2-1). This kind of design has taken advantage of three rotating cylinders at the front-end which knocked the seeds out of the heads, and then used the rest of the machine to separate the straw from the chaff, and the chaff from the grain.

The adoption of the non conventional design is mainly related to the fact that the threshing and separation processes are more related to the centrifugal force and less on gravity alone.

By the early eighties, most of the major manufacturers had settled on a design with much larger longitudinal threshing cylinders to do most of the work. Advantages were faster grain harvesting and gentler treatment of fragile seeds, which were often cracked by the faster rotational speeds of conventional combine threshing cylinders. The non conventional machines use a straightforward driveline layout. By using fewer belts more power is available for threshing, separation and cleaning.

Extreme threshing efficiency and huge kernel separation are the major characteristics of the non conventional "two rotors" technology (see Fig. 2-2).

A modern grain combine performs many functional processes. These are gathering and cutting, threshing, separation, and cleaning.

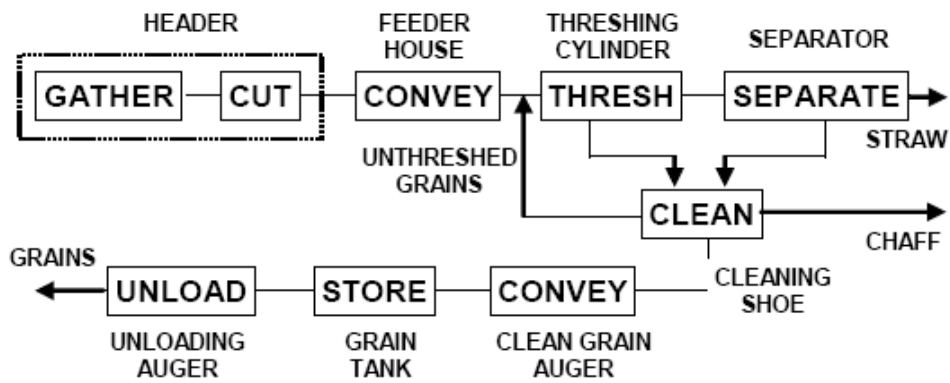


Fig. 2-2 – Process diagram of a combine harvester [16].

The combines that do not use the oscillating action of a straw walker use rotary action to accomplish threshing and separation, and are thus called rotary combines. Fig. 2-3 is a picture of a non-conventional or axial flow combine utilizing twin rotors.

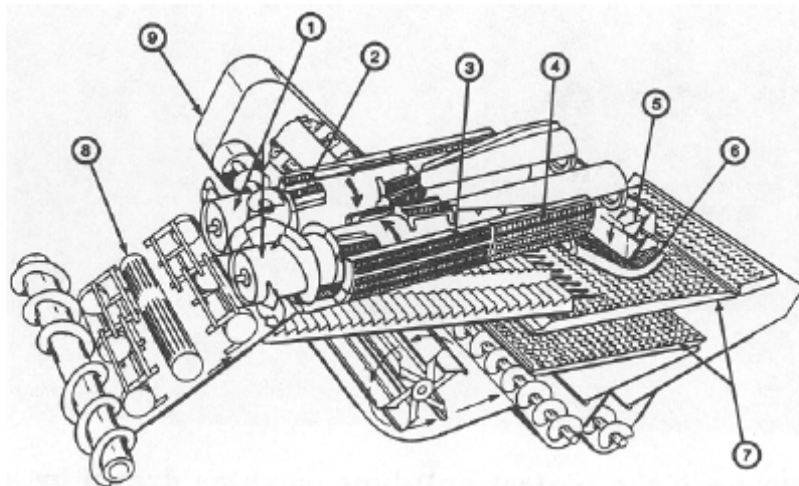


Fig. 2-3 - An axial flow rotary combine utilizing twin rotors: (1) rotor, (2) rasp bars, (3) threshing concave, (4) separating concave, (4) discharge beater, (6) beater grate, (7) cleaning shoe, (8) feeder housings, (9) tailings auger [16].

In an axial combine harvester, as the crop spiral around the rotor, rasp bars mounted on the rotor rub the grains out through the concave grate which is smaller for wheat than corn (Fig. 2-4). An helicoidally flux of the crop is favoured by splitting the incoming crop flow over two counter rotating rotors. The threshing process is mainly given by two principal effects:

- "grain to grain effect" (i.e. the threshing of the grain kernels among themselves);
- threshing between the concave and the rotor (i.e. rotor cage).

The factors that have the most influence over the process are:

- the environmental crop conditions;
- the variety of the crop;
- the setting of the cutter bar;
- grain to straw ratio;
- the rotor speed;
- the ground speed;
- the concave clearance (radial distance between the concave and the rotor);
- the quantity of the crop processed (capacity).

Thus, due to the "grain to grain effect", if the capacity increases the threshing efficiency increases. A wider cutting bar permits a faster work speed and productivity, lower loss and higher crop quality. A faster rotor speed and a lower concave clearance assure the complete crop separation (the centrifugal force consequently increases) but make the threshing more aggressive causing an inferior crop quality.

In conclusion, the three most important useful parameters used to evaluate the quality of the threshing process are:

- the loss amount;
- the grain integrity;
- the amount of the grain remain thrust upon the straw after the process.

2.3 Threshing zone: description of the mechanical parts

The crop processing unit of an axial flow harvesting machine performs the following operations:

- after cutting the crop the threshing unit performs the threshing and separation activities making the kernels free from chaff and straw;
- the cleaning unit cleans the crop separating the kernels from other small particles like chaff and short straw.

The above described mechanical parts involved in the threshing process are illustrated in Fig. 2-4 and Fig. 2-5. The first operations are performed by the rotor that induce an helicoidal flux of crop. Spirally arranged rasp bars and friction elements mounted on the rotors favour the friction of the crop against the concaves.

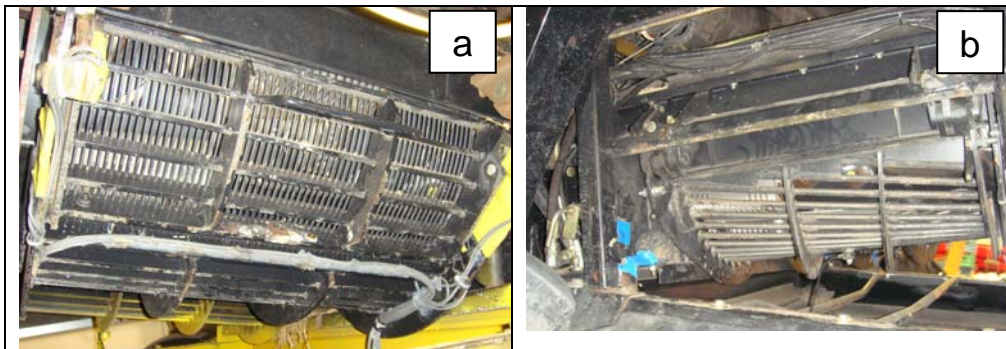


Fig. 2-4 – Field tests: concave grate for wheat crop (a) and corn crop (b).

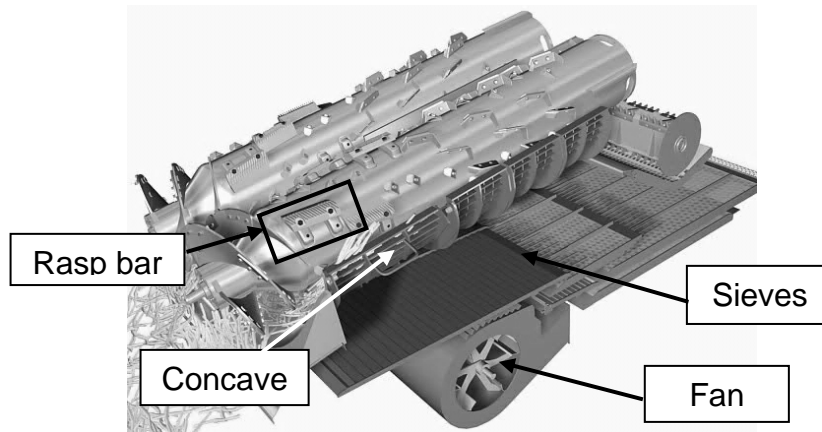


Fig. 2-5 – Threshing unit: mechanical parts involved in the threshing process.

It is possible to distinguish two different zones (Fig. 2-6) along the rotor length: the threshing zone and the separation zone. There are four concaves, two for each rotor, two mounted adjacent to the threshing zone and two adjacent to the separation zone. The concave size, the number as well as the shape of the rasp bars changes as they go from the threshing zone to the separation zone.

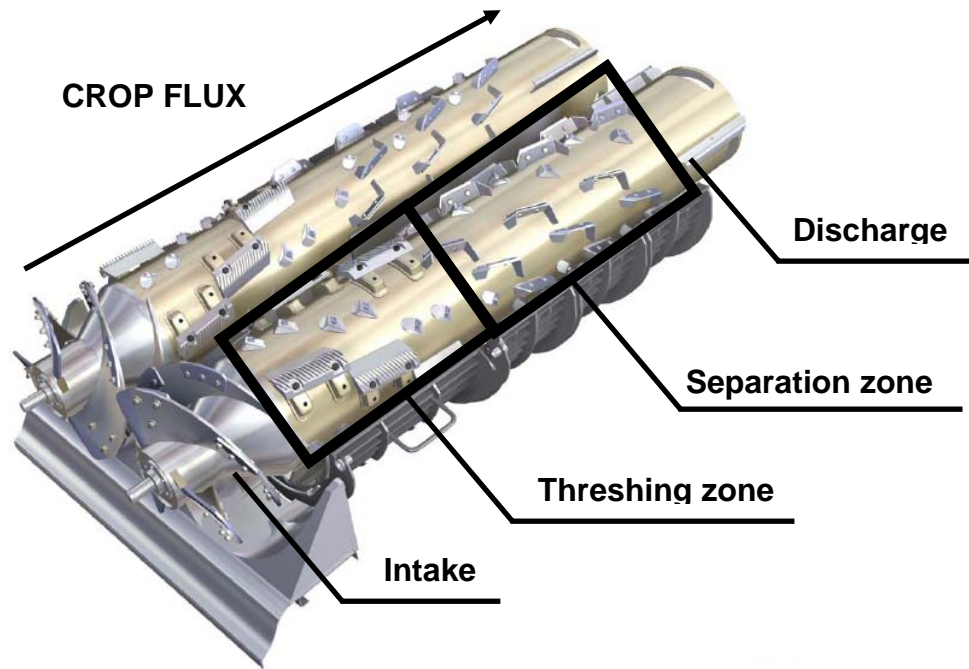


Fig. 2-6 – Threshing unit: threshing and separation zones.

The most of the crop leaves the straw within the threshing zone where the concaves are expected to show the highest vibration.

On the other hand, within the separation zone the rotors tries to loosen the kernels still trapped into the straw. When the grains are already been threshed, it is cleaned under the rotors by means of the fan air and the reciprocating sieve displacement.

2.4 Process efficiency indicators

This part deals with the description of the setting modifications in order to figure out the influences of the different parameters over the quality of the threshed.

There are four indicators [16], which tell how well the combine is performing.

These four indicators are:

- Grain tank sample;
- Distribution of material on the grain pan and upper sieve;
- Type and amount of returns;
- Losses.

The indicator depends on different parameters. These parameters may be changed in function of different kinds of crop harvested.

2.4.1 Grain tank sample

A large amount of trash in the grain tank indicates the crop is being over-threshed and/or the cleaning fan speed is too slow. The first step to correct this problem is to increase the concave clearance and/or reduce the rotor speed. This reduces or eliminates the material break-up caused by over threshing.

Cracked or damaged grain can be caused by a concave setting that is too close to the rotors. Increasing the concave clearance and then reducing the rotor speed are ways of solving this problem.

Tab. 2-1 - Different combine configurations for different types of crop
[15].

| Crop | Straw elevator front drum | Rotor speed | | Rotor Configuration | Concaves | | |
|--------------------|---------------------------|-------------|-----------|---------------------|----------------|--------------------------|--------------------|
| | | CR960 17" | CR980 22" | | Clearance | Type | Extension position |
| Barley | 2 | 1200 | 1100 | Standard | 14 mm (9/16") | Small grain | Out |
| Canola | 3 | 880 | 630 | Standard | 23 mm (15/16") | Small grain | Out |
| Corn | 5 | 800 | 500 | Standard | 23 mm (15/16") | Universal or Round bar | Out |
| Flax | 2 | 1350 | 980 | Standard | 8 mm (5/16") | Small grain | In |
| Bermuda grass | 2 | 1730 | 1350 | Standard | 5 mm (3/16") | Small grain | In |
| Blue grass | 1 | 1330 | 1030 | Standard | 13 mm (1/2") | Small grain | Out |
| Milo/Sorghum | 1 | 1000 | 750 | Agitator pins | 21 mm (13/16") | Small grain or universal | Out Out |
| Mustard | 3 | 880 | 680 | Standard | 17mm (11/16") | Small grain | Out |
| Oats | 2 | 1200 | 930 | Standard | 14 mm (9/16") | Small grain | Out |
| Peas/ Edible Beans | 3 | 800 | 700 | Standard | 21 mm (13/16") | Universal or Round bar | Out |
| Rice | 2 | 1300 | 1000 | Rice | 21mm (13/16") | Universal | Out |
| Rye | 2 | 1500 | 1180 | Standard | 14 mm (9/16") | Small grain | Out |
| Soybeans | 2 | 750 | 600 | Standard | 23 mm (15/16") | Universal or Round bar | Out |
| Sunflower | 3 | 750 | 600 | Standard | 23 mm (15/16") | Universal or Round bar | Out |
| Triticale | 2 | 1450 | 1100 | Standard | 14 mm (9/16") | Small grain | Out |
| Wheat normal | 2 | 1500 | 1150 | Standard | 13 mm (1/2") | Small grain | Out |
| Wheat Hard red | 2 | 1700 | 1330 | Standard | 8 mm (5/16") | Small grain | In |
| Wheat Soft | 2 | 1250 | 980 | Standard | 13 mm (1/2") | Small grain | Out |

2.4.2 Grain losses

Grain losses are expressed as percentages of total grain entering the combine. Combine losses considered in this thesis are divided into (1) threshing losses, (2) separation losses and (3) cleaning losses.

Threshing or cylinder losses are those un-threshed grain heads that escape the combine at the rear with straw and are expressed as the percentage of total grain entering the combine.

Separation losses are lost grain expressed as the percentage of total grain entering the combine.

Cleaning losses, also called shoe losses, are the grain lost with chaff expressed as the percentage of the total grain entering the combine.

As wrote before, the efficiency parameters try to numerically describe the efficiency of the threshing process. Some of the efficiency parameters have been obtained directly from measurements (i.e. losses and broken grain percentage used in this thesis as efficiency parameters) and others from probability function calculations (i.e. distribution of the crop over the threshing zone used in [4]). The performance of the threshing mechanism is expressed by the threshing efficiency and separation efficiency. The first is the percentage of the threshed kernels calculated on the basis of the total kernels entering the threshing mechanism. The second one is defined as the percentage of the kernels separated in the threshing zone of the rotor, to the kernels in the crop entering the threshing mechanism.

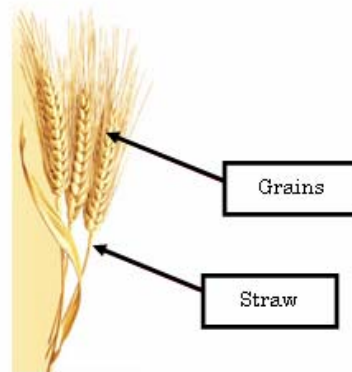


Fig. 2-7 – Parts of the plant.

The total threshing process is given by two sub-process: threshing and separation.

During the first part of the process, which take place at th threshing zone, the kernels are separated by the straw ear. However, some kernels remain attached to the straw: this amount of kernels is threshed within the separation zone.

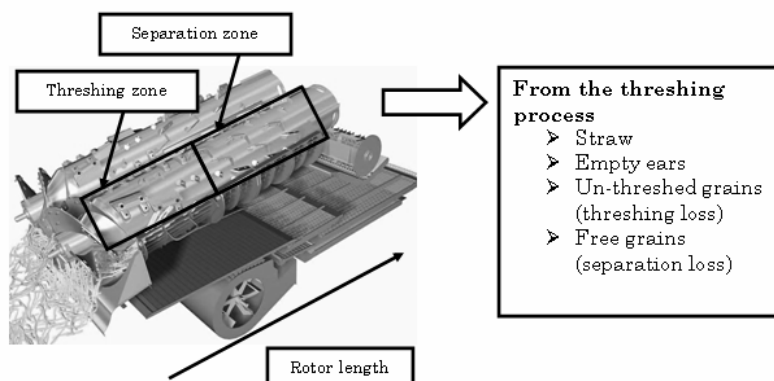


Fig. 2-8 – Product of the threshing process.

The total threshing process yields straw, empty ears, un-threshed grains (threshing loss) and free grains (separation loss). The kernels that are not threshed constitute the so-called threshing loss; the free grains that leave the machine together with the straw constitute the separation loss. The total amount of threshing and separation losses give the so-called total loss.

Hereafter the techniques to obtain the efficiency parameters for stationary (Fig. 2-9) and field (Fig. 2-10 and Fig. 2-11) tests have been reported.

During the stationary tests the products coming from the threshing unit are shaken in order to obtain the free grains that constitute the separation loss. The straw and the grain still attached to the plant are re-threshed obtaining the threshing loss, straw and empty ears as reported in the diagram of Fig. 2-9.

Concerning the field tests, for several runs, the total and threshing losses have been evaluated by two types of measurements:

- Total loss: a second combine behind the first one is used to re-thresh the crop that comes from the first combine in order to collect the total loss as shown in Fig. 2-10;
- Threshing loss: a raking machine can separate the free grains that fall down on the ground (separation loss) and the grain still attached to the plant (threshing loss). After this separation, the material is re-threshed by the second combine in order to obtain the threshing loss (Fig. 2-11).

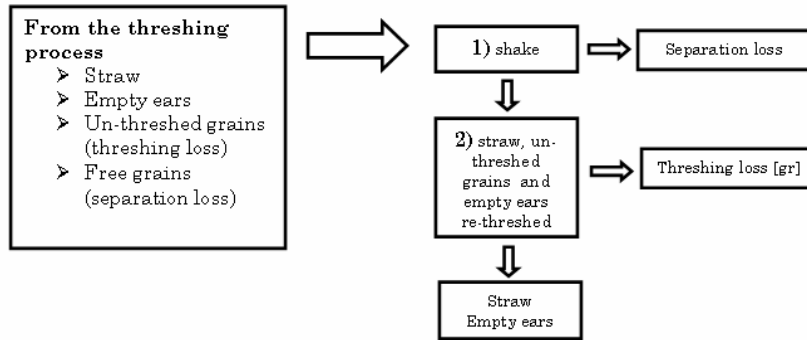


Fig. 2-9 – Stationary tests: measure of threshing and separation losses.



Fig. 2-10 –Field tests: measurement of the total loss.



Fig. 2-11 – Field tests: measurement of the threshing loss.

2.5 Experimental set-up in the combine harvester

2.5.1 Sensor overview

Piezoelectric accelerometers and condenser microphones have been used for all the tests in stationary (i.e. indoor laboratory test rig) and field conditions (i.e. outdoor during field operations). The main part of the results shown in the next sections have been achieved by means of field tests. Both indoor and outdoor set-up have been built in order to test the machine under different setting conditions by varying capacity (i.e. total crop entering the machine), concave distance (i.e. radial distance between the concave and the rotor), rotor speed, grain to straw ratio (i.e. length of the plant) and degree of moisture.

Both test rigs are designed taking some important constraints into account:

- measure signals from points located in both threshing and separation zones in order to understand if differences in excitation occur between these two zones;
- measure the vibration signal from the machine frame in order to understand which is the contribution of the machine vibration to the total vibration measured on the concaves;
- measure the vibration of the concave in order to understand how the crop distribution affects the concave vibration;
- mounting transducers in points where the transmission path is less intricate;
- verify the effectiveness of the microphone signals acquired from both threshing and separation zones in explaining the crop distribution between the rotor and the concave; verify if the microphone outside cabin can simulate the user ear linking the threshing performances with the sound perceived.

In the outdoor tests the vibration signals (sampling frequency 6 kHz) have been measured by means of piezoelectric accelerometers (frequency range: 1-10 kHz) in six following positions (Fig. 2-12): concave middle and rear positions (tri-axial accelerometers) in the threshing zone; and at the front and rear of the rotor cover (mono-axial accelerometers).

The sound pressure signals (sampling frequency 6 kHz for field tests) have been acquired by means of three condenser microphones mounted in the following positions: close to the threshing (threshing and threshing middle microphones in Fig. 2-12) and separation (separation microphone in Fig. 2-12) zones, considered as process microphones, and outside the cabin used to simulate the user ear in linking the threshing performances with the sound perceived.

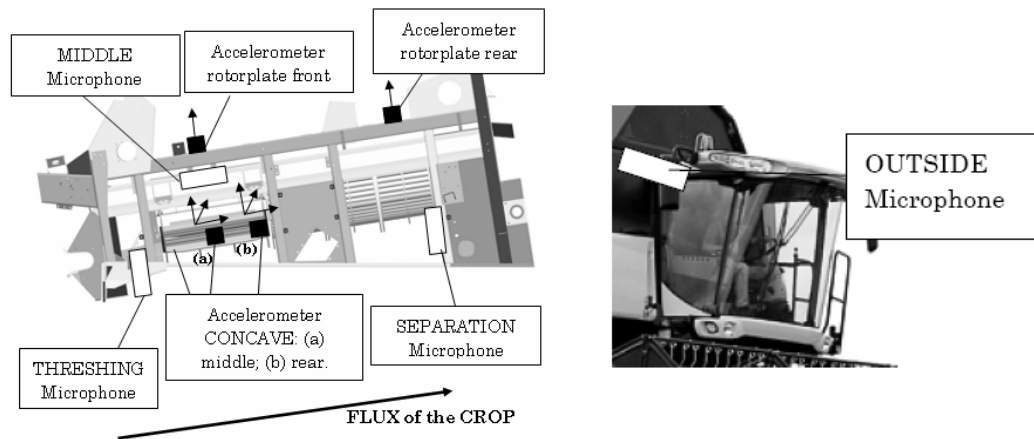


Fig. 2-12 – Test rig: accelerometers and microphones mounted on the machine.

In order to use signal processing approaches in the angular domain a tachometer signal (1 pulse/rev) has been used as revolution reference (Fig. 2-13).

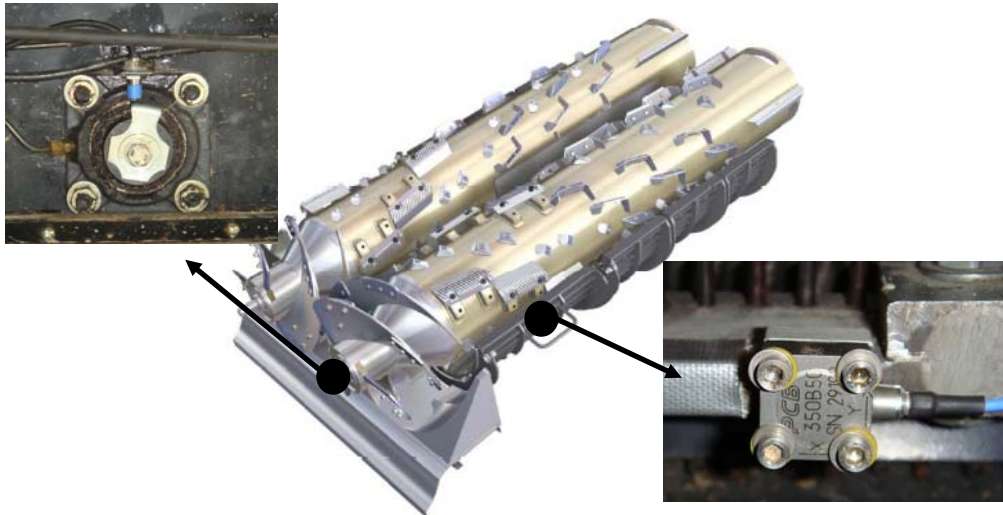


Fig. 2-13 – magnetic pick up and triaxial accelerometer concave middle.

As measurement platform a PXI system from National Instrument has been used. The PXI system is actually an industrial computer, which can be programmed in LabView. The PXI can directly be connected to the CAN network of the machine in order to acquire all the signals coming from the combine process related to:

- Machine speed: the rotation speed of the driving wheels is commonly used to estimate the ground speed.
- Crop throughput: the total amount of crop material [t/h] entering the machine is a mixture of grain kernels and other material. This crop throughput directly determines the work load of the combine harvester. There are several possibilities to measure the crop throughput:
 - the engine load in combine harvester is estimated by registering the instantaneous fuel consumption;

- the driving torque on the auger and the straw elevator does not only include the torque which is necessary to transport the crop material from the feeding auger to the threshing drum (the torque driving the straw elevator), but additionally contains the driving torque on the feeding auger and the pick-up reel. As result, a better signal-to-noise ratio is achieved than when only the torque in the straw elevator is measured. (patented by Case New Holland (Strubbe and Missotten, 1999), Fig. 2-14 (a)). The feedrate signal has been taken as reference for the selection of the stationary part of the signal. As shown in Fig. 2-14 (b), a run of the machine is typically made up of various parts. A first part where the machine runs empty (1), a second part where the amount of crop is process increases (2), a third part where the crop is processed (3) and a final part where the amount of crop decreases (4). The third part is obviously the main subject of investigation. The averaged value of the third part will be used as reference for the feature correlation and runs selection.

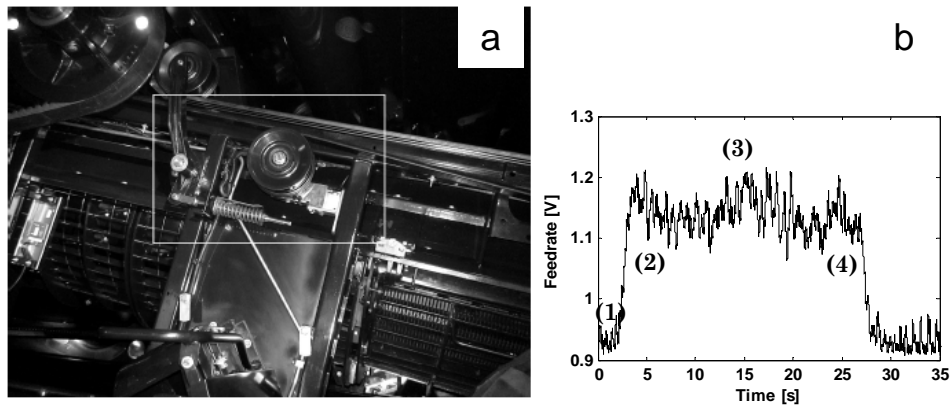


Fig. 2-14 – the feedrate sensor (white rectangle in (a)) and the feedrate signal measured in (b).

- Crop moisture: a high moisture content does not permit a good separation of the kernels from the straw causing lower efficiency performances of the threshing process. In order to take into account this effect a humidity and temperature transducer has been used.

2.6 Indoor and outdoor test campaigns

In order to analyze the influence of the operational parameters and the vibro-acoustic behaviour of the threshing unit, several controlled measurements on an indoor test set-up are performed. Moreover tests on the field under various setting conditions are carried out. The position of the transducers is the same for indoor and outdoor tests. Hereafter a description of the two kind of tests will be reported:

- Indoor tests:

The indoor tests (Fig. 2-15) have been conducted by using wheat crop. A belt conveyor has used for the crop transportation to the combine harvester. Then the crop has been processed by the machine without grain tank. The crop processed was collected in several bins under the machine used to understand the crop distribution. The products of the process, described in Fig. 2-8, have transported by a second belt conveyor to the machine used to obtain the losses.

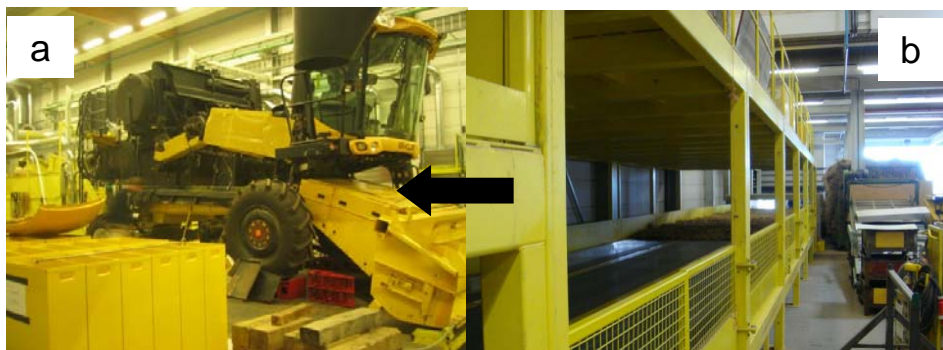


Fig. 2-15 – Indoor test rig: (a) harvesting machine, (b) belt conveyor.

➤ Outdoor tests:

The outdoor tests (Fig. 2-16), taken as reference in this thesis, reproduce the real operative condition of the combine harvesting machine: the influence of the humidity, the presence of “fresh” crop, variable in function of the field threshed (Fig. 2-17) and the possibility to work on different crop (i.e. barley, wheat and corn) are three important environmental factors that have not been considered in the indoor tests.



Fig. 2-16 – Outdoor tests condition: (a) barley field, (b) corn field



Fig. 2-17 – Different varieties of corn crop

SIGNAL PROCESSING TECHNIQUES

3.1 Introduction

In this thesis several processing techniques have been considered in order to evaluate their limits and capabilities in obtaining useful information from vibro-acoustic signals of the threshing unit of the combine harvesting machine. This chapter presents an overview of the theoretical background of the techniques, as well as their application to a synthesized signal model.

The cyclostationary approach combined with the angular domain analysis can make it possible to understand more in detail the characteristic mechanisms of the threshing process. Moreover, taking advantage of these techniques, it will be possible to obtain simple metrics linked to the efficiency indicators of the process.

Sound quality metrics such as Loudness and Tonality are applied in order to keep into account the human ear non-linearity. They can be used in order to simulate the judgment of the user who adjusts the machine setting depending on the sound emitted by the threshing unit.

Moreover, the Approximate Entropy (AppEn) is considered in order to describe the regularity of the acquired acceleration signals.

3.2 Cyclostationary approach

Non-stationary signals can be defined as signals which satisfy a non-property, i.e. they do not satisfy the property of stationarity. It is not possible to define a general theory which treats non-stationary signals. The non-stationary behaviour of each signal has to be individually evaluated.

The theory of the cyclostationarity has been developed by Gardner [14] in the telecommunication field and by Antoni [6] in the mechanical field for the diagnosis of rotating machines.

In this research, the cyclostationary approach has been used, on one hand, in order to evaluate the concave vibration due to the different mechanisms characteristic of the threshing process. On the other hand, the author takes advantages of the cyclostationary approach to obtain simple metrics that can be related to the efficiency of the process, such as the Indicator of Cyclostationarity (ICS_{nx}) outlined in [7].

3.2.1 Background theory

The signal measured from the concave (see Chapter 2) can be considered as a signal generated by a periodic mechanisms. The conventional spectral analysis reveals the signal periodicities but not the energy ones which can be analyzed by using the cyclostationary approach. A short description of several operators [6] will be given.

Let $x(t)$ a generic signal, the operator that extracts the deterministic value of a signal is \mathcal{P}_0 ; the time-average value m_x and the power P_x of the signal are computed as:

$$m_x = \mathcal{P}_0 \{x(t)\} = \lim_{T \rightarrow \infty} \frac{1}{T} \int_T x(t) dt \quad (3.1)$$

$$P_x = \mathcal{P}_0 \{ |x(t)|^2 \} = \lim_{T \rightarrow \infty} \frac{1}{T} \int_T |x(t)|^2 dt \quad (3.2)$$

where $\int_T \bullet dt$ is the summation over an interval of length T.

For decomposing the energy flow of the signal not only into a constant trend, but also into periodic components a new operator is presented. \mathcal{P}_α is the operator that extracts the periodic component at the *cyclic frequency* α of the signal:

$$\mathcal{P}_\alpha \{ \bullet \} = \left(\lim_{T \rightarrow \infty} \frac{1}{T} \int_T \bullet e^{-j2\pi\alpha t} dt \right) e^{j2\pi\alpha t} = \mathcal{P}_0 \{ \bullet e^{-j2\pi\alpha t} \} e^{j2\pi\alpha t} \quad (3.3)$$

The \mathcal{P}_α -operator first computes the Fourier coefficient $\mathcal{P}_0 \{ \bullet e^{-j2\pi\alpha t} \}$ at frequency α and then assign to the periodic component $e^{j2\pi\alpha t}$ in order to reconstruct a pure sinusoidal signal.

The operator that extracts all periodic component in a time function is called \mathcal{P} :

$$\mathcal{P} \{ \bullet \} = \sum_{\alpha \in A} \mathcal{P}_\alpha \{ \bullet \} \quad (3.4)$$

where A is the set of cyclic frequency α associated with non-zero periodic component because if $\alpha = 0$ the operator compute the Power Spectral Density (PSD) of a signal $x(t)$.

The \mathcal{P} -operator shown in the Equation (3.4) reveals the repetitive event that characterizes the signal. The *mean instantaneous power* is depicted in the following Equation:

$$P_x(t) = \mathcal{P} \{ |x(t)|^2 \} \quad (3.5)$$

Since the flux of energy could vary periodically, then $P_x(t)$ will have a Fourier series decomposition with non-zero coefficients. P_x^α is called *cyclic power* of the signal at cyclic frequency α :

$$P_x(t) = \sum_{\alpha \in A} P_x^\alpha e^{j2\pi\alpha t} \quad (3.6)$$

where the cyclic powers are obtained by use of the \mathcal{P}_0 -operator:

$$P_x^\alpha = \mathcal{P}_0 \left\{ |x(t)|^2 \cdot e^{-j2\pi\alpha t} \right\} \quad (3.7)$$

A generic definition of cyclostationarity is the following:

- *a signal is said to exhibit cyclostationarity if there exist a cascade of linear and non-linear transformations that produces a periodic component. It is said to exhibit cyclostationarity at cyclic frequency α if there exists a cascade of linear and non-linear transformations that produces a sine component with frequency α .*

In order to make a distinction between first and second order of cyclostationarities it is important to define the predictable and random components of a signal.

First of all, the mean value of a cyclostationary signal defined as:

$$m_x(t) = \mathcal{P} \{ x(t) \} \quad (3.8)$$

is itself a signal, in contrast to the stationary case where it is always a constant.

The Equation (3.8) means that the mean value of a cyclostationary signal estimates the first-order cyclostationary part of the signal itself, also called predictable part of the signal $x_p(t)$.

By difference, the residual part $x_r(t) = x(t) - x_p(t)$ gives the random part of the signal that estimates the second-order cyclostationary part of the signal. Now it is possible to define:

- *A signal is said purely cyclostationary at order 1 if its residual part $x_r(t)$ does not show cyclostationarity at any order.*
- *A signal is said purely cyclostationary at order 2 if its deterministic part $x_p(t)$ is nil and its residual part is cyclostationary at order 2.*

Until now the signal have been considered in the time domain and all the cyclostationary properties are related to that domain. In practice, the threshing unit of the combine harvester is composed by a rotor and the hidden periodicities are related to its angles of rotation and not to time.

Then, the vibration signals acquired are re-sampled in the angular domain in order to obtain the predictable and residual parts of the signal.

In practice, after the angular re-sampling of the vibration signals the predictable part of the signal $x_p(\theta)$ is estimated by using the Time Synchronous Average (TSA):

$$\hat{x}_p(\theta) = \frac{1}{N} \sum_{k=0}^{N-1} x(\theta + k\Theta) \quad (3.9)$$

where Θ is the angular cycle period length of the signal, N the number of cycles within the signal and L the length of the re-sampled signal in the angular domain.

From Equation (3.9) the residual part of the signal is estimated as wrote before:

$$\hat{x}_R(\theta) = x(\theta) - \hat{x}_p(\theta) \quad (3.10)$$

3.2.2 Indicators of Cyclostationarity

As mentioned in [7] the Indicator of Cyclostationarity (ICS_{nx}) tries to quantify the distance of a cyclostationary process from the closest stationary process having a similar power spectral density. In particular ICS_{1x} and ICS_{2x} give an indication of the presence of first-order and second-order cyclostationarity components within a signal.

Hereafter both ICS indicators are exploited:

$$ICS_{1x} = \sum_{\alpha \in A, \alpha \neq 0} \frac{\left| \mathcal{P}_0 \{ x_p(t) e^{-j2\pi\alpha t} \} \right|^2}{P_{x_R}} = \sum_{\alpha \in A} \frac{\left| \lim_{T \rightarrow \infty} \left(\frac{1}{T} \int x_p(t) e^{-j2\pi\alpha t} dt \right) \right|^2}{\lim_{T \rightarrow \infty} \frac{1}{T} \int |x_R(t)|^2 dt} \quad (3.11)$$

$$ICS_{2x} = \sum_{\alpha \in A, \alpha \neq 0} \frac{|P_{x_R}^\alpha|}{P_{x_R}} = \sum_{\alpha \in A} \frac{\left| \lim_{T \rightarrow \infty} \left(\frac{1}{T} \int |x_R(t)|^2 e^{-j2\pi\alpha t} dt \right) \right|}{\lim_{T \rightarrow \infty} \frac{1}{T} \int |x_R(t)|^2 dt} \quad (3.12)$$

where A is the set of all possible cyclic frequency α , $x_p(t)$ and $x_R(t)$ are the periodic and residual parts of the signal respectively.

Valid estimators of the ICS_{1x} and ICS_{2x} , applied to the signal in the angular domain and for a set ω of cyclic frequency, are defined as:

$$\widehat{ICS}_{1x} = \sum_{\alpha \neq 0, \alpha \in \omega} \frac{|L^{-1}DFT \{ x_p(\theta) \}(\alpha)|^2}{|L^{-1}DFT \{ x_R^2(\theta) \}(0)|} \quad (3.13)$$

$$\widehat{ICS}_{2x} = \sum_{\alpha \neq 0, \alpha \in \omega} \frac{|L^{-1}DFT \{ x_R^2(\theta) \}(\alpha)|}{|L^{-1}DFT \{ x_R^2(\theta) \}(0)|} \quad (3.14)$$

where $DFT\{x(\theta)\}(\alpha)$ is the discrete Fourier transform of the signal $x(\theta)$ and α is the cyclic frequency expressed in order because the angular domain is used to estimate the indicators.

3.3 Sound quality metrics

Machinery noise often contains tonal features because of rotating components and lightly damped structural resonances. Hereafter, the Stationary Loudness and Tonality metrics are introduced. These metrics are extracted from the sound pressure signals measured outside the cabin of the harvester. By using the above mentioned metrics it is possible to take into account the human ear non-linearity; they can be used to simulate the judgment of the user who adjusts the machine setting depending on the sound emitted by the threshing unit.

3.3.1 Stationary Loudness ISO 532 B

The parameter mostly related to the sound intensity perception is loudness. The sensation-stimulus relation of loudness is a subjective relation.

The Loudness Level expressed in Sone is obtained for each time frame using the Zwicker method [8], starting from 1/3 octave band sound pressure level data.

The data can be originated from either a free or diffuse sound field. The Zwicker method is capable of dealing with complex broadband noises and takes masking into account.

The analysis allows distinguishing between unmasked and masked contours. Thus, it can be observed that certain levels are either entirely or completely masked by the previous one.

The total loudness is calculated as the surface under the enveloping partial loudness contours and can be expressed in Sone, or as loudness level in Phones as a function of time.

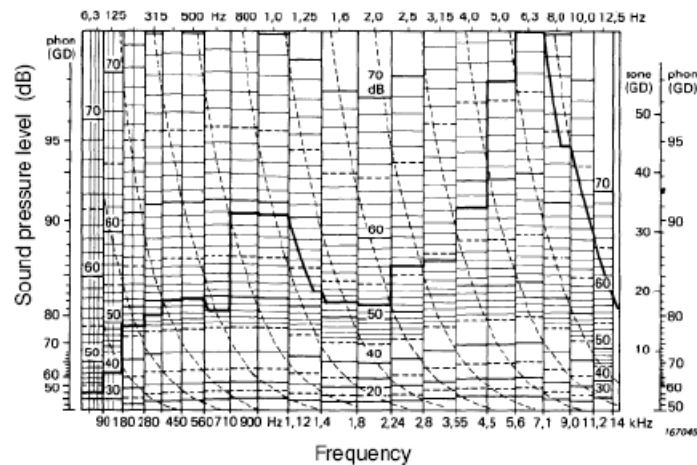


Fig. 3-1 - Loudness calculation according to Zwicker's method [8].

Fig. 3-1 shows the graph used for the loudness calculation procedure. The “loudness distribution” or “loudness patterns” represents specific loudness (loudness in each third octave band) as a function of critical-band rate.

This distribution takes the following aspects into account: (1) the nonlinear relationship between excitation and specific loudness and (2) the non ideal frequency selectivity of the human ear which is expressed in critical bands and in the slopes found in masking patterns.

The inner ear can be considered to act as a set of constant percentage bandwidth filters.

These filters are constant with a Bandwidth of around 110 Hz for frequencies below 500 Hz and are evolving to a constant percentage value (23%) at higher frequencies. These bandwidths are called “Critical bands” and are approximated as third octave bands in the pattern distribution. The critical bands play an important role in the loudness calculation.

It is worth noting that two tones of equal level with a frequency separation larger than the critical band, are ‘louder’ than a single tone with a level equal to the sum of both levels and a frequency equal to the mean of the frequencies. With increasing frequency separation of the two tones, loudness increases.

This means that loudness is not produced from separate spectral components, but rather that two components influence each other, especially if their frequency separation is small.

The fundamental assumption of the model is that loudness is not produced from spectral lines or from the spectral distribution of the sound directly but it is the sum of the specific loudness that are produced at different critical band rates. Both the frequency related transformation into critical-band rate and the amplitude related transformation into specific loudness are of crucial importance for evaluating sound in terms of the human hearing system. In the graph of Fig. 3-1, the shape of the specific loudness is approximated by three parts.

- It starts with a vertical rise up to the third octave band level measured (because the specific loudness slope towards lower frequency is ignored in the calculation).
- It becomes a main value corresponding to the third-octave band level in question and rises again vertically for the next higher third octave band, if its level is larger than that of its neighboring lower third octave band.
- If the next higher third octave band level is lower, the decrease follows the brokenlines, corresponding to the upper slope of specific loudness. The upper slope of the specific loudness corresponds closely to the transformed upper excitation slopes that, for narrowband sounds, contribute strongly to the total loudness. The area surrounded by the thick solid line indicates the total loudness of the noise. This area is approximated by a rectangular area of the same basis but of a height that marks the total loudness on the left scale and the corresponding loudness level on the right scale.

Method A and method B for Stationary Loudness

There are two methods for calculating stationary loudness, according to the international ISO 532.

- The first method A, referred to as Stevens method, utilizes physical measurement obtained from spectrum analysis in terms of octave bands.
- The second method B (used to calculate the Tonality metric), referred to as Zwicker's method, utilizes spectrum analysis in terms of one-third octave bands and it is used for the analysis in this report and described below.

The procedure for standard Stationary Loudness is based on five empirical relations or concepts, according to the stationary loudness standard.

- The widest frequency bands in which the loudness level depends only on the sound pressure level (critical bands).
- A rule relating the total loudness of a sound to the contributions from the critical bands.
- A relation between the part of the loudness appropriate to each band and the centre frequency of that band.
- The difference between the equal-loudness contours from frontal (free) sound and for a diffuse sound field.
- A loudness function relating loudness in sones to loudness level in phons, which is identical to that given in ISO/R 131.

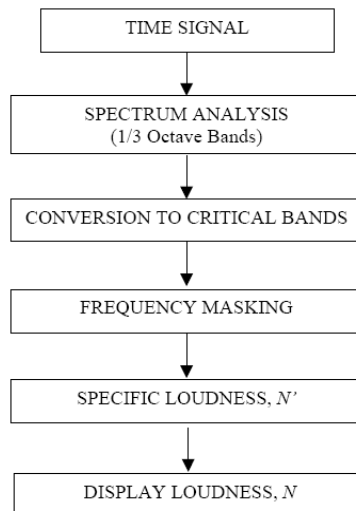


Fig. 3-2 - General procedures for calculating stationary loudness according to method B.

The subsequent steps to calculate the stationary loudness according to the method B are:

- Time signal: time signal that is used to calculate Stationary Loudness.
- Spectrum analysis: 28 1/3 octave filters spectrum analysis covering the frequencies audible by the human being.

- Conversion to critical bands: above 500 Hz, critical bands are approximately one-third octave in width. Since the lower one-third octave filters are narrower than 100 Hz, the bands below 500 Hz are combined to the critical bands. The 28 1/3 octave bands are combined to the critical bands in the following way. In the lowest frequency region, the one-third octave bands with centre frequencies from 25 to 80 Hz are combined to form the first band. The one-third octave bands from 100 to 160 Hz are combined to form the next band. The 200 and 250 Hz bands are combined. The bands from 315 to 12500 Hz are used individually, since their bandwidths approximate critical bands. The DIN 45631 standard describes how to obtain values for critical banded based one-third octave bands.
- Frequency masking: after conversion from 28 1/3 octave bands into critical bands a correction is applied depending whether the environment is a free or diffuse field. The SPL values are then converted into loudness values and frequency masking is applied. The frequency masking is only from the masking of higher critical bands by lower critical bands. The masking of lower critical bands is considered to be negligible.
- Specific loudness, N' : each critical band can be displayed as a specific loudness spectrum N' .
- Display loudness, N : displayed all bands of specific loudness are summed into a single number and as the stationary loudness (total loudness), N .

Loudness function

Using as the reference point the loudness of a 40 dB 1 kHz tone, corresponding to a loudness of 1 sone, the loudness function can be calculated. It is shown in Fig. 3-3 by the solid line. The abscissa is the level of the 1 kHz tone, the ordinate the loudness on a logarithmic scale.

The exponent of the power law that corresponds to a straight line is given by the steepness of the straight line that occurs for levels above 30 dB. At levels below 30 dB of the 1 kHz tone, the power function is no longer usable as an approximation.

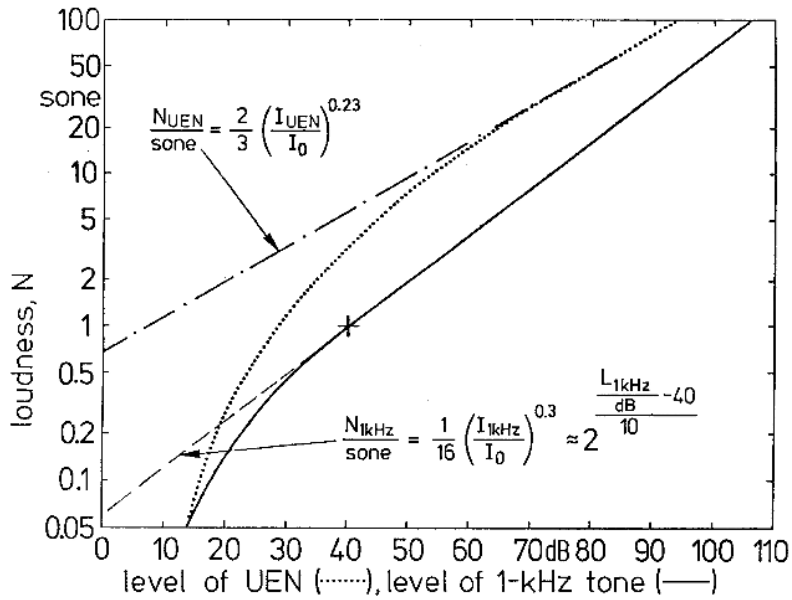


Fig. 3-3 - loudness function of 1 kHz tone (solid line) and uniform-exciting noise (dotted); loudness is given as a function of the sound pressure level. Approximations using power laws are indicated as broken and as dashed-dotted lines together with their corresponding Equations [8].

The difference between the broken line (corresponding to the power law) and the solid line shows the disagreement. At levels below 10 dB, the loudness of the 1 kHz tone decreases drastically and reaches zero at an SPL of 3 dB.

The loudness function is normally given for the 1 kHz tone. Fig. 3-4 shows the loudness value (sones) for a pure tone at 1 kHz and 40 dB, the result is very close to 1 sone (result shown in Fig. 3-3).

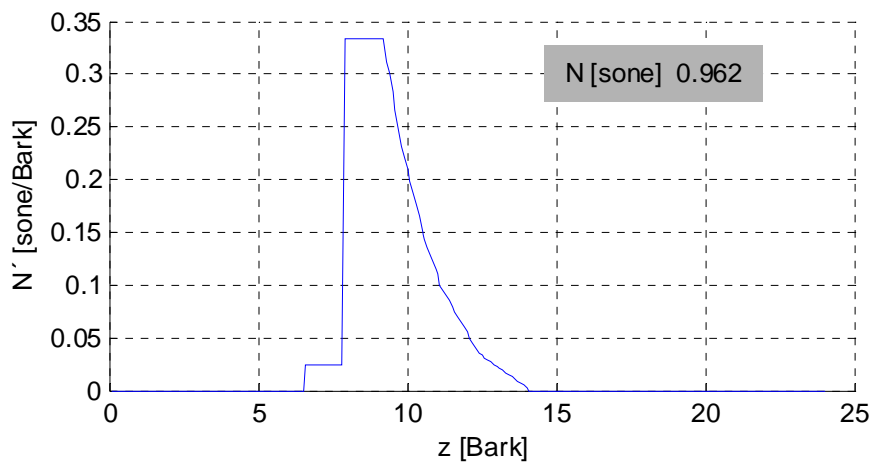


Fig. 3-4 - Stationary Loudness test spectrum for a pure tone at 1 kHz 40 dB with Matlab code.

3.3.2 Aures's model of Tonality

Aures proposed a method [9]-[10] (Fig. 3-5) for the calculation of tonality that takes into account the frequency, bandwidth and level of all tonal components as well as taking into account the effect of noise. Aures formulated Equations ((3.15), (3.16) and (3.17)) to describe the effect of bandwidth, frequency and level of tonal components on the perception of tonality. Hereafter, a diagram of the Aures algorithm [11] used to calculate the tonality metric is reported.

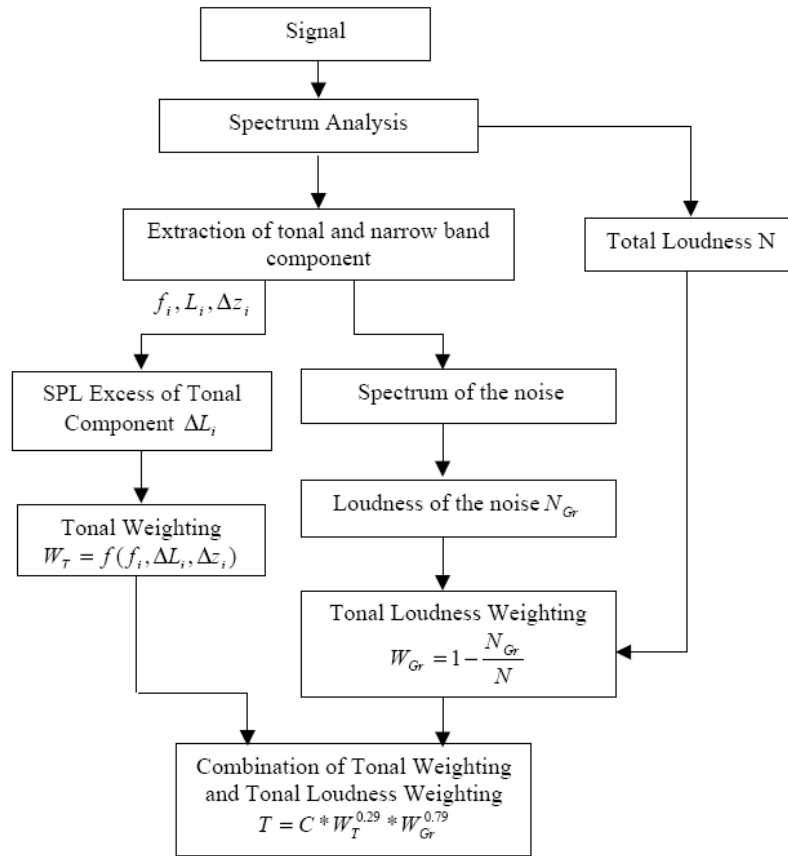


Fig. 3-5 - Aures's model of tonality [11].

The weighting functions w_1, w_2, w_3 are calculated as follows.

$$w_1(\Delta z_i) = \frac{0.13}{(\Delta z_i)/(Bark) + 0.13} \quad (3.15)$$

$$w_2(f_i) = \left(\frac{1}{\sqrt{1 + 0.2 \left(\frac{f_i}{0.7kHz} + \frac{0.7kHz}{f_i} \right)}} \right)^{0.29} \quad (3.16)$$

$$w_3(\Delta L_i) = (1 - \exp^{-\frac{\Delta L_i}{15}})^{0.29} \quad (3.17)$$

In these Equations, Δz is the bandwidth of the component in Bark, f is the center frequency of the tonal component in Hz; and ΔL is the excess level of the tonal component.

ΔL is given by Terhardt as:

$$\Delta L_i = L_i - 10 \log_{10} \left\{ \left[\sum_{k \neq i}^n A_{Ek}(f_i) \right]^2 + E_{Gr}(f_i) + E_{HS}(f_i) \right\} \text{ dB} \quad (3.18)$$

The weighting functions w_1 , w_2 , and w_3 are combined for all components with positive excess levels in the following manner,

$$w_T = \sqrt{\sum_{i=1}^n [w_1'(\Delta z_i) w_2'(f_i) w_3'(\Delta L_i)]^2} \quad (3.19)$$

- Δz is the bandwidth of the component in Bark;
- f_i is the central frequency of tonal component in Hz;
- ΔL_i is the SPL excess of the tonal component.

Aures introduced a correction factor in Equation (3.19) so that the model predicted responses closer to his subjective responses, specifically:

$$w_n' = w_n^{1/0.29} \quad \text{for } n=1,2,3. \quad (3.20)$$

Equation (3.19) represents a weighting due to the tonal characteristics of a sound. Aures also defined a weighting, w_{GR} , based on a loudness signal-to noise ratio:

$$w_{GR} = 1 - \frac{N_{GR}}{N} \quad (3.21)$$

- N is the total loudness

- N_{GR} is the loudness of the spectrum without tonal components

The loudness is calculated according to the Zwicker's algorithm. The Tonality is given by:

$$T = Cw_T^{0.29} w_{GR}^{0.79} \quad (3.22)$$

- C is a calibration term used to give a 1 kHz pure tone with a level of 60 dB a tonality of one.

Aures used the powers 0.29 and 0.79 to get the best agreement with his subjective test data.

3.4 Approximate Entropy (AppEn)

The Approximate Entropy (AppEn), developed by Pincus [12] is a statistical measure that quantifies the regularity of a time series in multiple dimensions. Yan and Gao [13] investigated the utility of AppEn as a measure for characterizing machine operation conditions and studied the effects of several parameters that are of key relevance for the calculation

The AppEn is used in [4] and [5] as a measure for characterising the threshing process, with the aim at introducing a feature linked to the operational and efficiency parameters coming from the combine harvesting machine. In this thesis, the algorithm to calculate the AppEn (the steps are illustrated in Fig. 3-6), is tested over a synthesized signal introduced in the next paragraph in order to check the influence of the tolerance r . As reported in Equation (3.23), the selection of r depends on the k value.

$$r = k \cdot std(S) \quad (3.23)$$

where k is a constant ($k > 0$), and $std(\bullet)$ represents the standard deviation of the time series. Hereafter, the diagram shows the main steps of the AppEn algorithm used in this thesis.

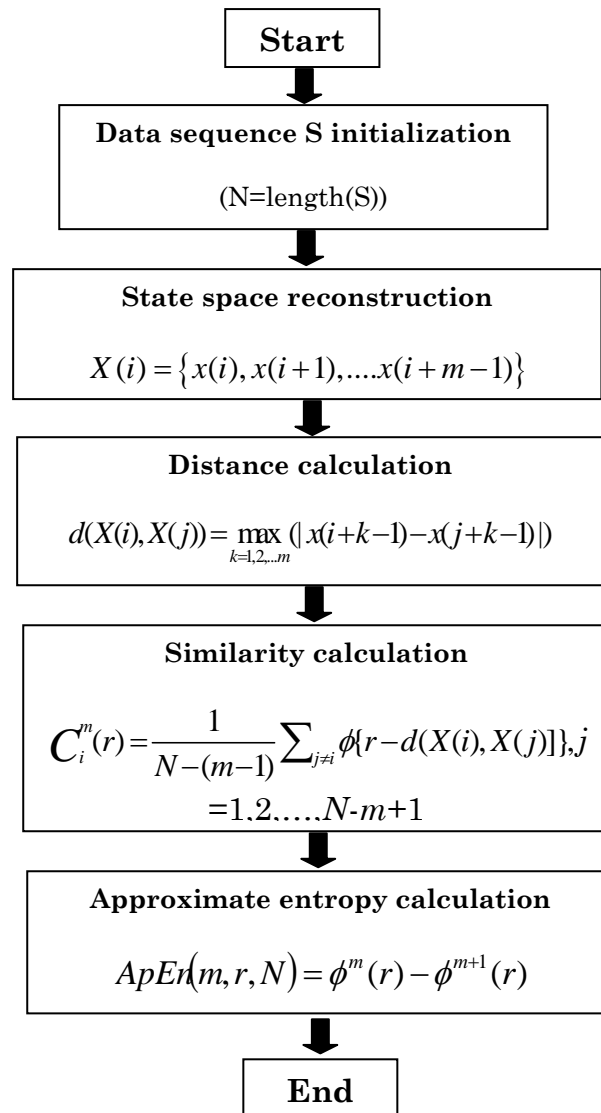


Fig. 3-6 – Steps in the Approximate Entropy calculation [13].

3.5 Application to a synthesized signal

In this paragraph, a synthesized test signal $x_s(t)$ (Equation (3.24)), is formulated in order to verify the capability of the signal processing techniques described in the previous paragraphs. This signal tries to simulate the vibration response of the concave to the mechanical excitations acting during the threshing mechanism. The three major frequency components, reproducing the periodical rasp bar interaction, depicted in $x_p(t)$ (Equation (3.25)), are combined with modulated random noise $x_R(t)$, describing the turbulence of the crop flow passing through the threshing unit (Equation (3.26)).

$$x_s(t) = x_p(t) + x_R(t) \quad (3.24)$$

$$x_p(t) = \sum_{i=1}^3 A(i) \sin(2\pi f(i)t) \quad (3.25)$$

$$x_R(t) = Gx_m(t)(1 + R \sin 2\pi ft) \quad (3.26)$$

where $A(i)$ and $f(i)$ are respectively the amplitude and frequency of the periodic components of $x_p(t)$; $x_m(t)$ is the normally distributed random noise with mean 0 and standard deviation 1 and G its gain; R is the ratio between the amplitude of the modulation and the carrier of the modulated noise $x_R(t)$, having values between 0 and 1; f is the frequency of the noise amplitude modulation.

The synthesized signal is depicted by the following Figures and the synthesized signal model parameters are listed in Tab. 3-1.

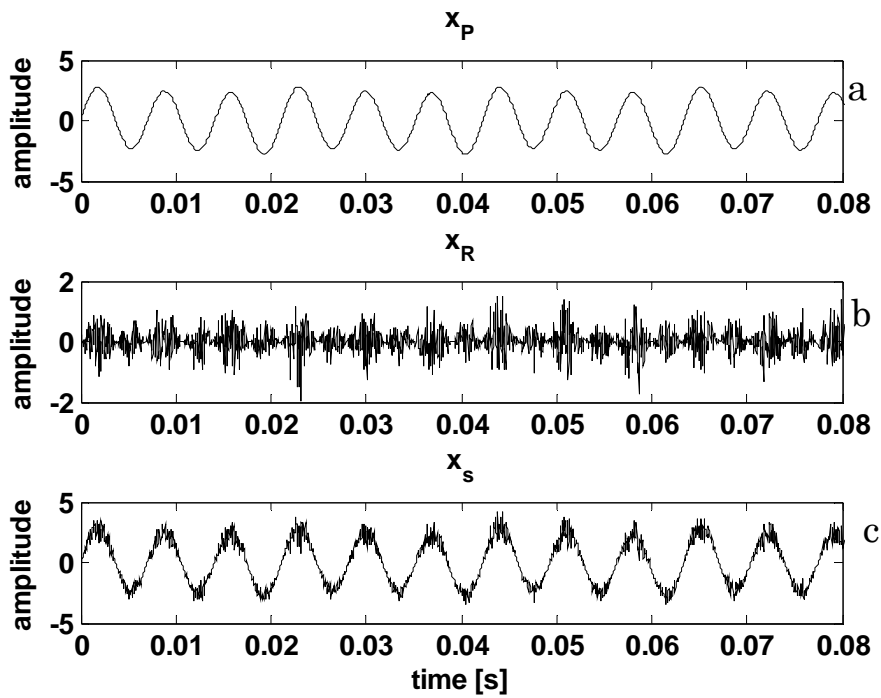


Fig. 3-7 - Synthesized signal: (a) $x_p(t)$, (b) $x_R(t)$, (c) $x_s(t)$.

Tab. 3-1 - Parameters related to the test signal.

| Parameter | Sinusoidal component | | |
|-------------|----------------------|------|-----|
| | 1 | 2 | 3 |
| $A(i)$ | 0.2 | 0.2 | 2.5 |
| $f(i)$ [Hz] | 47.3 | 94.6 | 142 |
| f [Hz] | 142 | | |

3.5.1 Cyclostationary approach

The previously defined ICS indicators have been calculated on the synthesized signal, testing different signal parameters.

The specific values of the parameters used in the synthesized signal and the correspondent values assumed by ICS_{1x} and ICS_{2x} indicators are listed in Tab. 3-2.

Tab. 3-2 – Synthesized signal parameters and ICS values.

| Test | A | G | R | ICS_{1x} | ICS_{2x} |
|-------------|-----------------|----------|------------|-------------------------|-------------------------|
| A | A(i)x1 | 1 | 0.1 | 1.5586 | 0.0098 |
| B | A(i)x1 | 2 | 0.1 | 0.3910 | 0.0105 |
| C | A(i)x1 | 3 | 0.1 | 0.1728 | 0.0099 |
| D | A(i)x1 | 1 | 0.5 | 1.3760 | 0.2003 |
| E | A(i)x1 | 1 | 0.9 | 1.1059 | 0.4111 |
| F | A(i)x2 | 1 | 0.1 | 6.2785 | 0.0086 |
| G | A(i)x3 | 1 | 0.1 | 14.0328 | 0.0101 |
| H | A(i)x0.5 | 1 | 0.1 | 0.3910 | 0.0104 |

As expected, the parameter that mostly affects the ICS_{1x} is the amplitude of the periodic component A whereas ICS_{2x} is mostly affected by the modulation amplitude. It is worth noting that as A increases from 1 to 3 (tests A, F and G keeping $G = 1$ and $R = 0.1$ in Tab. 3-2), the ICS_{1x} increases from 1.55 to 14.03.

Moreover, observing Fig. 3-8, depicting the two numerators of the ICS_{nx} (for $n = 1, 2$), it can be noted an increase of the ICS_{1x} numerator because the amplitude of the deterministic part ($x_p(t)$ in Equation (3.11)) increases as shown in Fig. 3-8 (a) and (c). On the other hand, the amplitude of the ICS_{2x} numerator is the same for the two tests as shown in Fig. 3-8 (b) and (d).

It is worth noting that, an increase of the R ratio (tests A, D and E keeping both A and G equal to 1 in Tab. 3-2), causes an increase of ICS_{2x} from 0.0098 to 0.41.

This is due to the fact that the amplitude of the frequency component at 142 Hz (see Fig. 3-9 (b) and (d)), of the ICS_{2x} numerator ($x_R(t)$) depicted in Equation (3.12)), increases. Thus, the difference between the first component and the one at 142 Hz becomes smaller giving high ICS_{2x} value.

Otherwise, the random noise gain K does not influence the variation of ICS_{2x} .

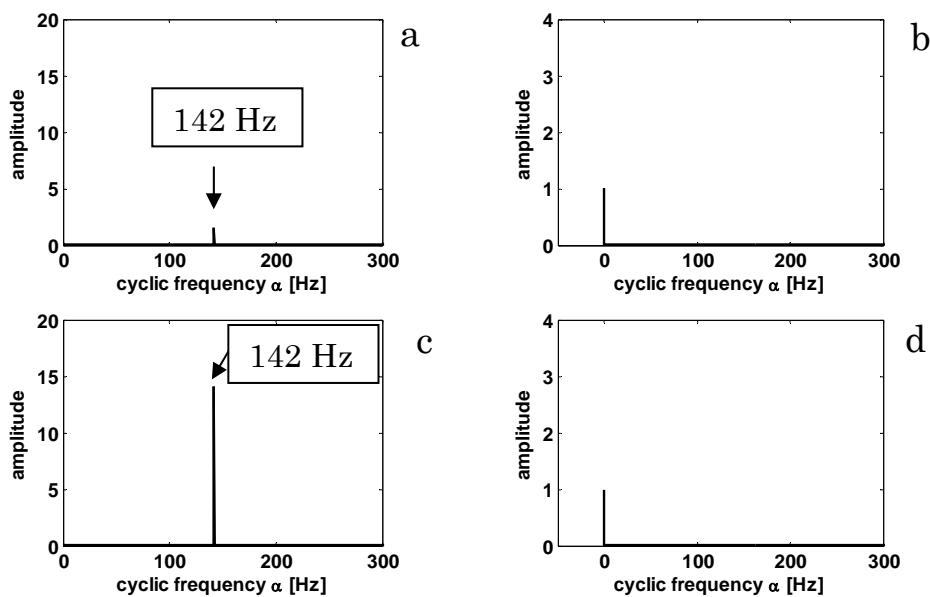


Fig. 3-8 – Influence of the amplitude value: A(i)x1 (test A): (a) numerator ICS_{1x} , (b) numerator ICS_{2x} , and A(i)x3 (test G): (c) numerator ICS_{1x} , (d) numerator ICS_{2x} .

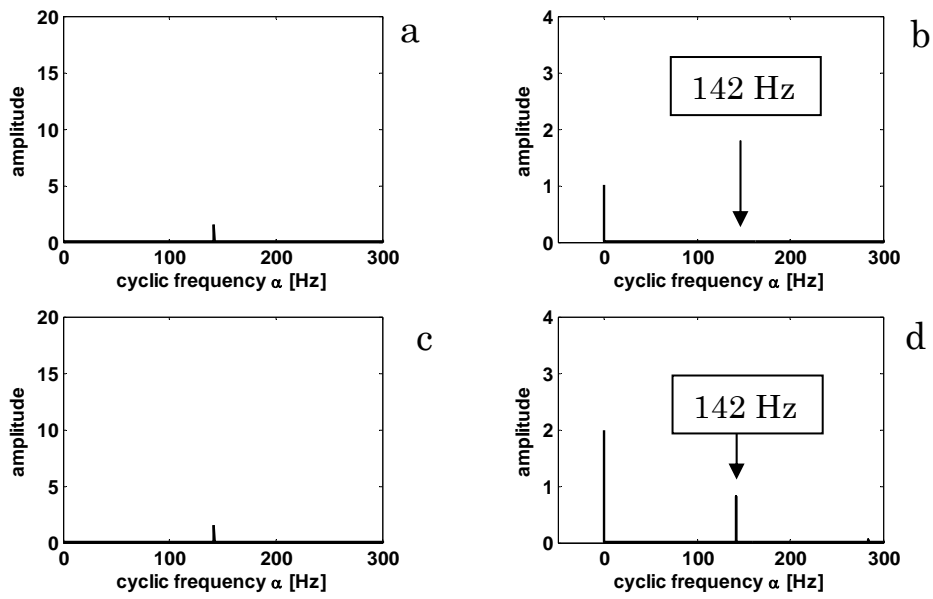


Fig. 3-9 – Influence of the R value: $R = 0.1$ (test A): (a) numerator ICS_{1x} , (b) numerator ICS_{2x} , (c) and $R = 0.9$ (test E): (c) numerator ICS_{1x} , (d) numerator ICS_{2x} .

3.5.2 Aures's tonality algorithm

In order to test the Aures's algorithm [10], hereafter Fig. 3-10 contains 3 plots; (a) represents the power spectrum of the signal, (b) shows the tonal components extracted from the power spectrum and (c) depicts the relevant tonal component whose the SPL excess is larger than zero: in particular looking in Fig. 3-10 (c) the components are the first three listed in

Tab. 3-1. The abscissa of the three plots is frequency [Hz].

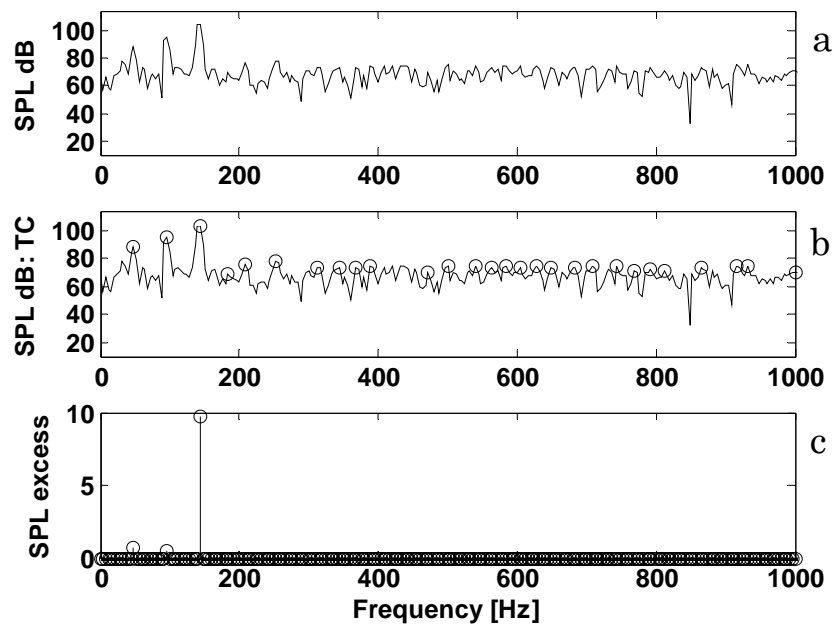


Fig. 3-10 – Aures's algorithm tested on the signal model.

The calculation procedure is based on the pitch-extraction algorithm described by Terhardt [9]. Sometimes, it is possible that not all the peaks in the power spectrum can be extracted as tonal components. Thus is a critical point for the tonality calculation. Only the components which satisfy the requirements in the algorithm, can be extracted.

3.5.2.1 Choose of the algorithm's parameters

The tonality algorithm is tested over the synthesized signal in order to choose the useful parameters (i.e. frequency resolution, the calibration factor used to give a 1 kHz pure tone with a level of 60 dB a tonality of one) that can be used for the tonality calculation of the actual signals.

The frequency resolution, and consequently the calibration factor, are taken equal to 4 Hz and 2.1923 respectively. A accurate frequency resolution (Fig. 3-11 (a)) makes difficult the localization of the tonal components (by using the algorithm) because there are too much candidates as tonal component.

On the other hand, a poor frequency resolution (Fig. 3-11 (b)) generates a spectrum not accurate and consequently the localization of the tonal components (by using the algorithm) does not work correctly.

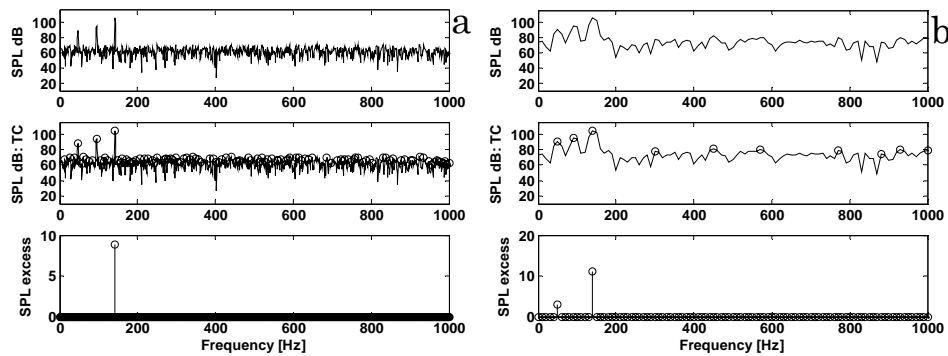


Fig. 3-11 - Tonality algorithm results for two frequency resolution values: (a) 1 Hz, (b) 10 Hz.

The extraction of the tonal components is performed by the algorithm scanning the spectral samples by using the following Equation:

$$L_{i-1} < L_i \geq L_{i+1} \quad (3.27)$$

where:

- L_i is the relative SPL of the i th spectrum sample,
- L_{i-1} is the relative SPL of the next lower sample
- L_{i+1} is the relative SPL of the next higher sample

If the candidate was found by this criterion, it is further tested each of the conditions is fulfilled.

$$L_i - L_{i+j} \geq 1 \text{ dB}; j = -3, -2, +2, +3 \quad (3.28)$$

The value of Equation (3.28) is set equal to 1 (Fig. 3-12 (a)): in this way the spectrum is scanned by the algorithm in detail and, moreover, the tonality code is able to recognize the three tonal components of the signal model. Increasing from 1 to 10 (Fig. 3-12 (b)) the algorithm becomes less accurate; only two of the three tonal components have been detected.

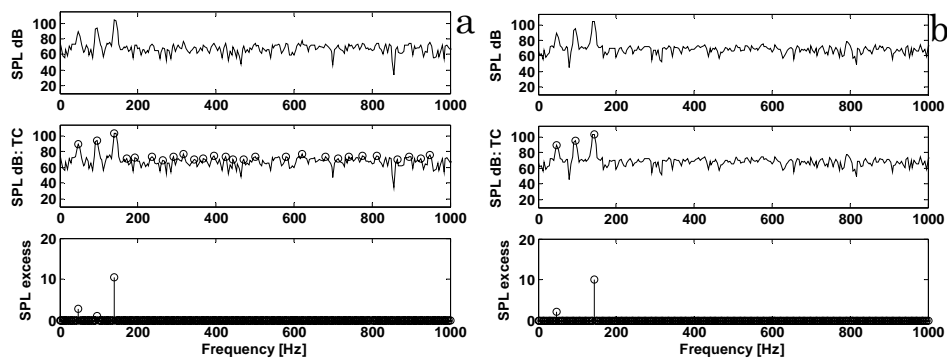


Fig. 3-12 – Tonality algorithm results in function of the value of Equation (3.28): (a) 1, (b) 10.

3.5.2.2 Tonality evaluation for the synthesized signal

The effectiveness of the Aures algorithm for the tonality calculation has been conducted by using the synthesized signal model of Equation (3.24) with different values shown in Tab 3-3. It can be noted that with an increase of R (tests A, D and E) the tonality value T decreases.

The tonality value, as shown in Equation (3.22), is a combination of the tonal (w_T in Equation (3.19)) and noise (w_{GR} in Equation (3.21)) weightings. In particular the noise term is based on a loudness signal-to-noise ratio and it is the most influenced by the synthesized signal parameters depicted in Tab 3-3.

On the other hand, increasing the gain of the random noise G it can be noted a decrease of the tonality (tests A, B and C). As shown in Fig. 3-13 (b) the SPL excess is higher when the gain of the random noise is smaller. As the parameter G decreases the term w_{GR} (in Equation (3.21)) becomes smaller because both loudness values (with and without tonal component) increase. As wrote before, the term w_T is constant thus, it does not influence the final value of the tonality.

Increasing the amplitude of the deterministic part A (tests A, F, G and H keeping constant $G = 1$ and $R = 0.1$ in Tab 3-3) it can be observed an increase of the tonality value caused by the fact that the loudness of the total signal (N in Equation (3.21)) increases while, the loudness evaluated over the spectrum without tonal components (N_{GR} in Equation (3.21)) is constant. As it can be noted in Fig. 3-14 the SPL excess is larger when the amplitude of the tonal components is multiplied by 3 (see Fig. 3-14 (b)).

Finally, the R value of the modulated noise does not influence significantly the tonality values as depicted in Tab 3-3 for the tests A, D and E.

In conclusion the parameter of the synthesized signal model that mainly influence the tonality is the amplitude of the deterministic part.

Tab. 3-3 - Tonality values for simulated signals with noise amplitude increasing.

| Test | A | G | R | T [tu] |
|------|----------|---|-----|--------|
| A | A(i)x1 | 1 | 0.1 | 0.3120 |
| B | A(i)x1 | 2 | 0.1 | 0.2653 |
| C | A(i)x1 | 3 | 0.1 | 0.2424 |
| D | A(i)x1 | 1 | 0.5 | 0.2965 |
| E | A(i)x1 | 1 | 0.9 | 0.2775 |
| F | A(i)x2 | 1 | 0.1 | 0.3454 |
| G | A(i)x3 | 1 | 0.1 | 0.3801 |
| H | A(i)x0.5 | 1 | 0.1 | 0.2670 |

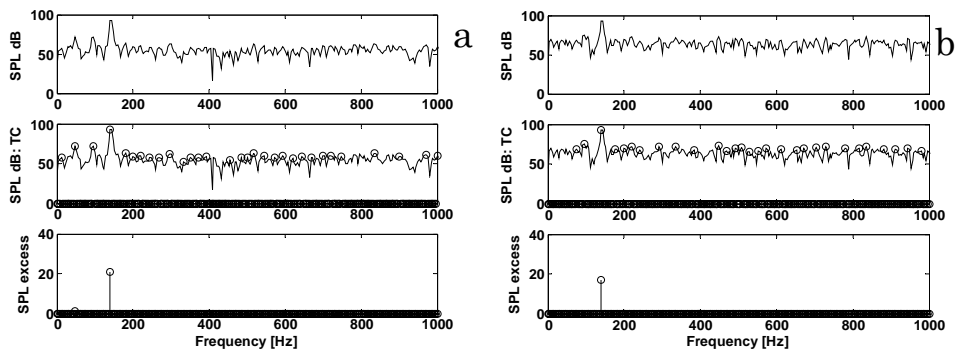


Fig. 3-13 - Tonality algorithm results in function of the random noise gain G : (a) $G = 1$, (b) $G = 3$.

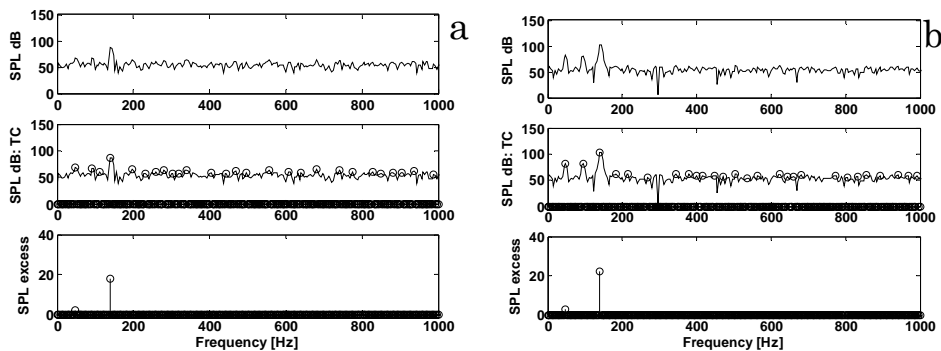


Fig. 3-14 - Tonality algorithm results in function of the amplitude $A(i)$: (a) $A(i)x0.5$, (b) $A(i)x3$.

3.5.3 Approximate entropy algorithm

The synthesized signal model is also used to evaluate the variation of the AppEn values in function of the characteristic parameters of its parameters.

Increasing the amplitude of the deterministic part of the signal (A in Tab. 3-4 for tests A, F, G and H), it is possible to note a decrease of the AppEn because the signal regularity increases as shown in Fig. 3-15.

Moreover, the AppEn is sensitive to the R coefficient of the modulated noise as depicted in Tab. 3-4. Increasing R from 0.1 to 0.9 (keeping constant $A(i)$ and G for the tests A, D and E) the AppEn decreases because the modulation amplitude of the noise (Equation (3.26)) introduces regularity in the time series as depicted in Fig. 3-16 (b).

Increasing the random noise gain G from 1 to 3 (tests A, B and C in Tab. 3-4), and keeping constant the amplitude of the periodic part $A(i)$ and R , it can be observed an increase of the AppEn caused by the increases of the signal randomness as shown in Fig. 3-17 (b).

Tab. 3-4 - AppEn values of test signal under various parameters.

| Test | A | G | R | AppEn |
|------|-------------------|---|-----|--------|
| A | $A(i) \times 1$ | 1 | 0.1 | 1.0627 |
| B | $A(i) \times 1$ | 2 | 0.1 | 1.4242 |
| C | $A(i) \times 1$ | 3 | 0.1 | 1.5380 |
| D | $A(i) \times 1$ | 1 | 0.5 | 1.0105 |
| E | $A(i) \times 1$ | 1 | 0.9 | 0.9245 |
| F | $A(i) \times 2$ | 1 | 0.1 | 0.5883 |
| G | $A(i) \times 3$ | 1 | 0.1 | 0.3259 |
| H | $A(i) \times 0.5$ | 1 | 0.1 | 1.4282 |

The AppEn algorithm is also tested over two signals depicted in Fig. 3-18 in order to observe the effect of the amplitude modulation of the carrier sine signal. In the real signal the amplitude modulation produces bursts. In particular the AppEn assumes values of 1.1, for the signal depicted in Fig. 3-18 (a), and 0.96 for the signal in Fig. 3-18 (b). Introducing an amplitude modulation on the signal, the regularity increases giving a smaller AppEn value.

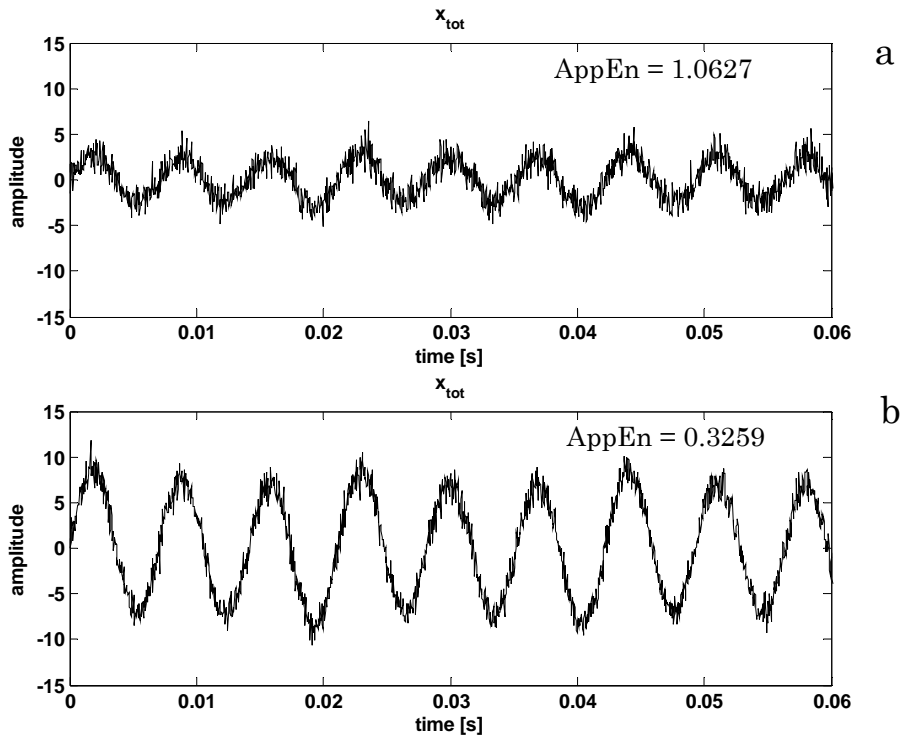


Fig. 3-15 – Synthesized signal: influence of the amplitude $A(i)$ (see Tab. 3-4) (a) test A, (b) test G.

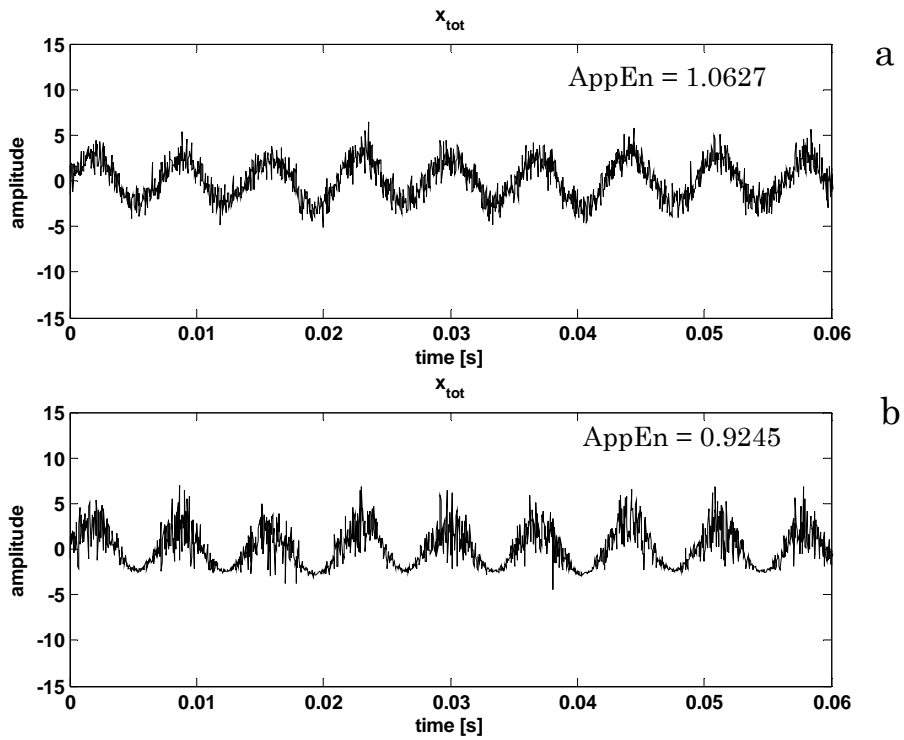


Fig. 3-16 - Synthesized signal: influence of the coefficient R (see Tab. 3-4) (a) test A, (b) test E.

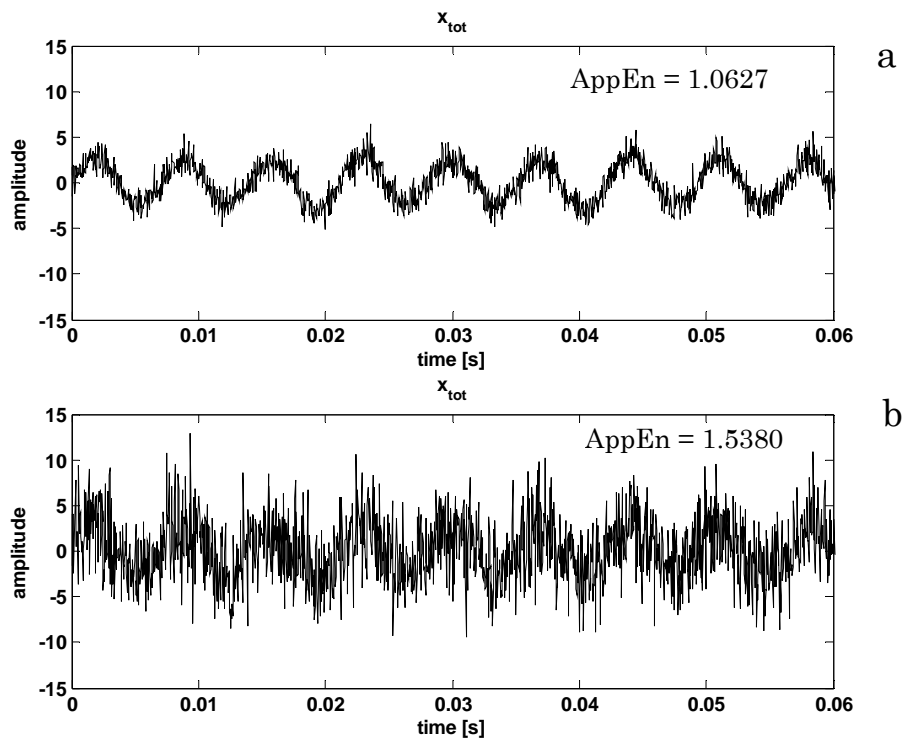


Fig. 3-17 - Synthesized signal: influence of the random noise gain G (see Tab. 3-4) (a) test A, (b) test C.

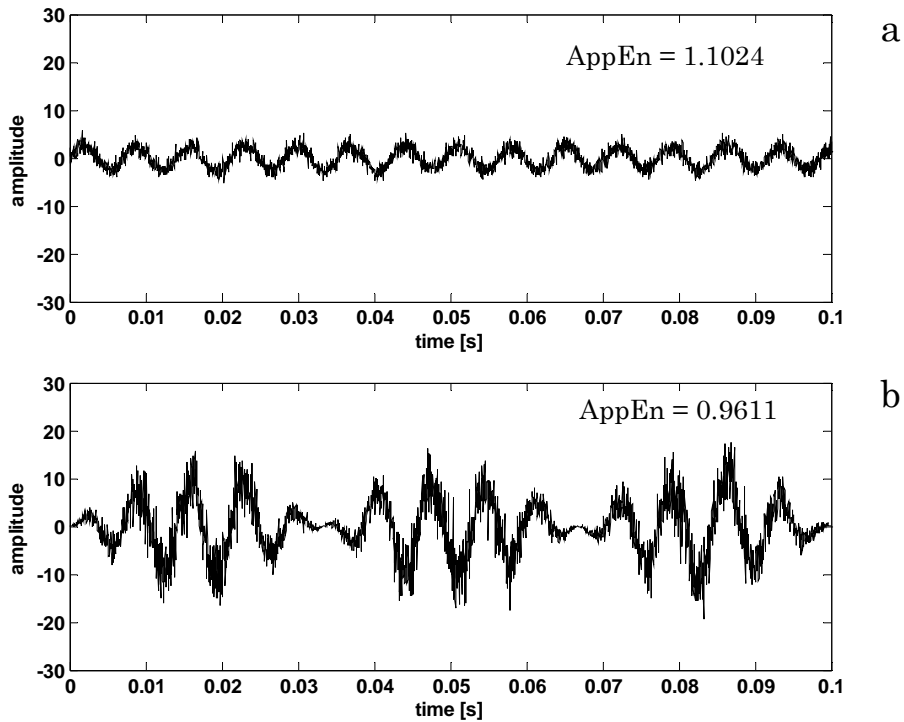


Fig. 3-18 – Synthesized signals: (a) without bursts, (b) with bursts.

At this stage, after presenting the influence of the synthesized signal parameters over the AppEn values, the effects of one parameter that is of key relevance to the AppEn calculation, e.g. the tolerance (r in Equation (3.23)), is discussed. The effect of k on the AppEn value calculation is shown in the next Figures, where, the amplitude A (see Fig. 3-19), the gain of the random noise G (see Fig. 3-20) and the coefficient R (see Fig. 3-21) of the synthesized signal are evaluated to verify the reliability of the AppEn calculation results.

As the k value increases, the variability of the AppEn decreases continually for all the setting parameters of the synthesized signal model such as the amplitude of the deterministic part (A) in Fig. 3-19, the gain of the random noise (G) in Fig. 3-20 and the parameter (R) in Fig. 3-21.

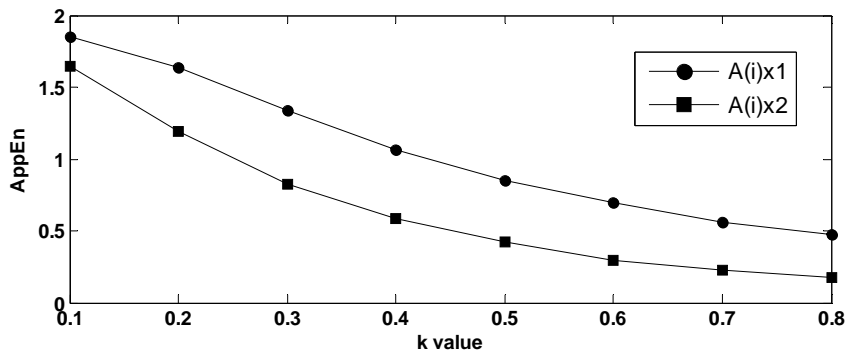


Fig. 3-19 – Effect of k on the AppEn values for two amplitude values of the synthesized signal with $G = 1$ and $R = 0.1$.

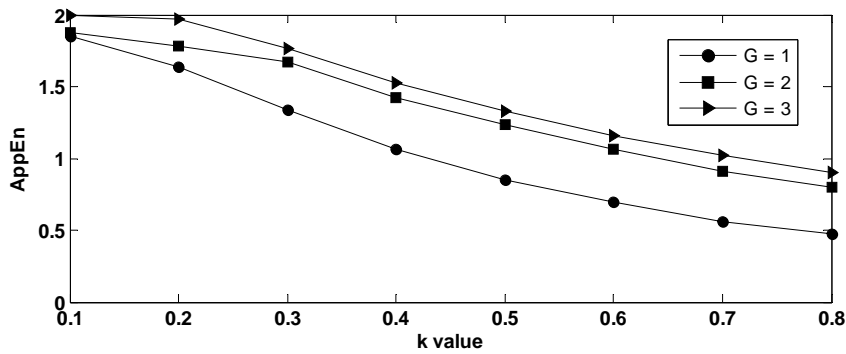


Fig. 3-20 - Effect of k on the AppEn values for three gain values of the synthesized signal with $A(i)x1$ and $R = 0.1$.

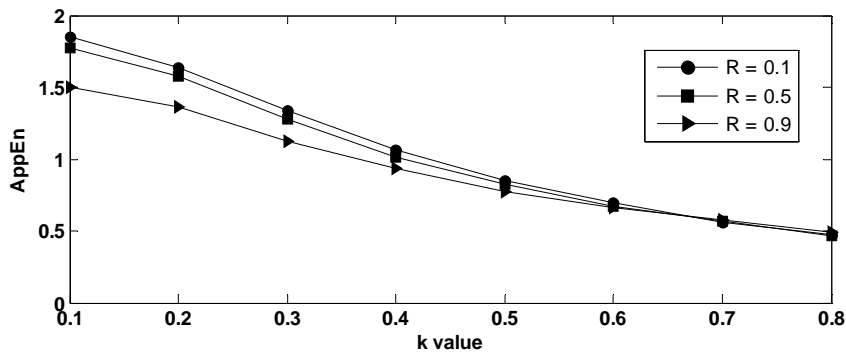


Fig. 3-21 - Effect of k on the AppEn values for three different coefficient R values of the synthesized signal with $A(i)x1$ and $G = 1$.

VIBRO-ACOUSTIC ANALYSIS OF THE THRESHING PROCESS

4.1 Introduction

The results obtained in [4] and [5] show that the concave middle radial vibration signal is the most closely correlated to the threshing process and it can be used for condition monitoring purposes. Thus, in this chapter, all the results concerning the vibration refer to that reference signal acquired in outdoor (field) tests.

In order to evaluate the influence of the operational and efficiency parameters some vibration metrics, such as Root mean Square (RMS) and Approximate Entropy (AppEn), are extracted from the raw vibro-acoustic signals.

Sound quality metrics, such as Loudness and Tonality, have been applied to the threshing and cabin microphone signals.

The cyclostationary approach is applied in order to give a detailed physical explanation of the threshing process mechanisms.

After analysing the signals by means of the above-mentioned techniques, some correlations between vibro-acoustic features and operational parameters are reported.

4.2 Time domain features

In this paragraph, a short review about the correlations between the time domain features (extracted from signals acquired in the field tests) and the operational parameters is shown. As wrote in Chapter 2 the **operational parameters** taken into account are the following:

- capacity (i.e. amount of processed crop expressed in terms of feedrate);
- concave distance (i.e. radial distance between the rotor and the concave);

The features extracted are the following:

- Root Mean Square (RMS), reflecting the energy of the signal;
- Approximate Entropy (AppEn) which reflect the regularity of a time series;
- Sound quality metrics, such as Loudness and Tonality extract information from the sound pressure signal measured from the cabin and threshing microphones.

The RMS values and the Sound Quality metrics are obtained by means of fixed segmentation; the signal (20 s) is divided into time records of 2 seconds. Then, the feature are calculated over these time segments. Thereafter, all the feature values are averaged providing one value for each signal, the so-called Av. “feature”.

The AppEn feature is calculated over 3000 sampling points of the time signal (corresponding to 0.2 s) according to what explained in the Chapter 3.

4.2.1 Influence of the capacity

The influence of the capacity (mass flow rate of the crop estimated with the feedrate signal) on the vibro-acoustic response is evaluated comparing different runs with rotor speed 1420 rpm and several concave distances.

Considering the Av. RMS values at the middle position, it can be noted quite a constant trend thus, the Av. RMS seems not sensitive to the capacity variations (as shown in Fig. 4-1 (a)) confirming the results achieved in [4] and [5].

The averaged values of these two metrics have been correlated as done for the RMS. From Fig. 4-1 (b) it can be noted that Loudness metric assumes high values for higher capacities showing a sort of linear trend. This means that the microphone signal from the cabin is sensitive to the increase of the capacity as achieved in [4] and [5].

Moreover, although the sound measured from the external microphone is produced by all the mechanical parts in operation (i.e. engine, rotor and transmission), the noise due to the threshing mechanism seems to be still relevant.

Tonality metric (see Fig. 4-1 (c)) shows no unique relationship to capacity variation for all concave distance settings. Therefore, the Tonality metric cannot be used to relate the characteristic frequency amplitudes to the capacity.

Loudness and Tonality metrics (see Fig. 4-1 (b) and (c)) confirm the results show in [5]. Loudness increases with the capacity while the Tonality is not sensitive to the capacity variation.

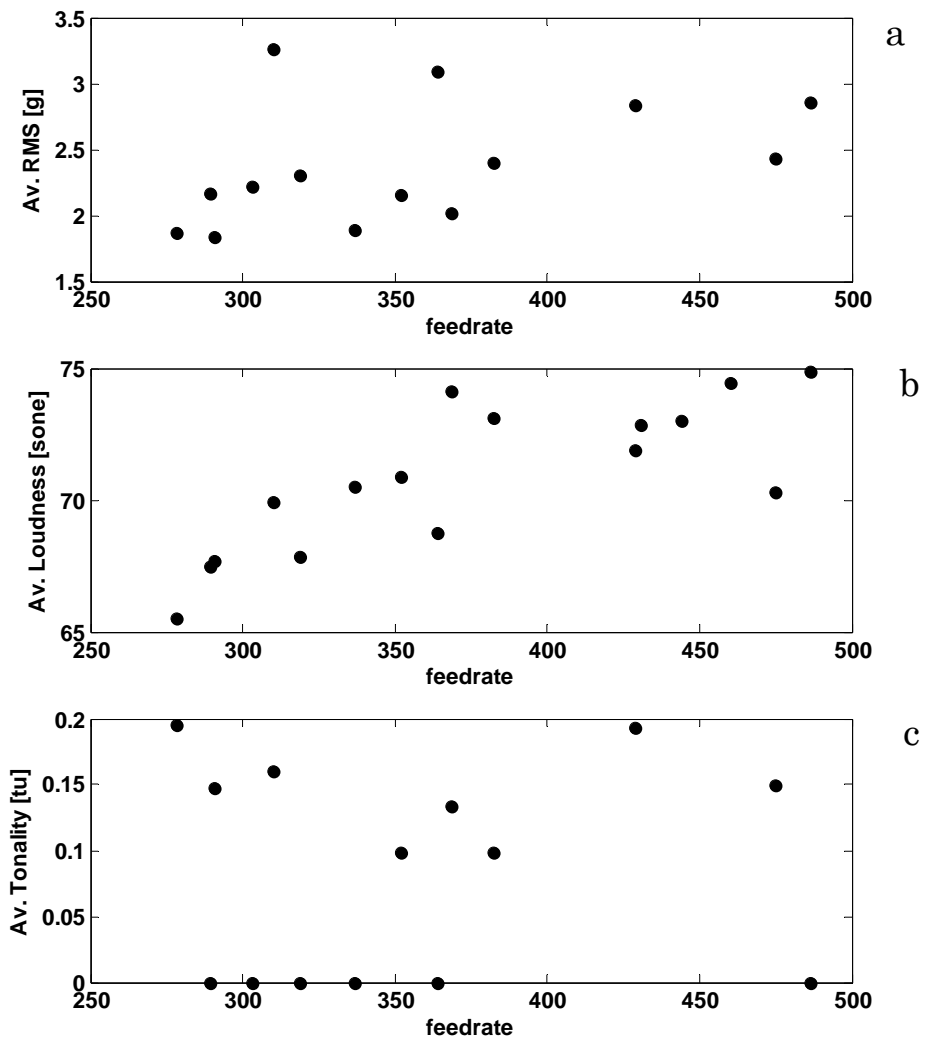


Fig. 4-1 – Features vs. capacity (field nr. 2): (a) Av. RMS at middle position, (b) Av. Loudness cabin microphone, (c) Av. Tonality cabin microphone.

4.2.2 Influence of the concave distance

The concave distance setting parameter is the most important for the user. A good crop distribution and, consequently, the quality of the threshed crop are strongly dependent on this parameter which can be tuned by the user during the on-the-go field operations.

Looking at the Fig. 4-2 (a), it can be noted a correlation existing between the energy of the accelerometer in the middle position and the concave distance. In particular, a trend showing a concavity zone around 20 mm is clearly visible. The Fig. 4-2 (b) and (d) depict the trend obtained for runs at 1420 rpm and average feedrate values 450 V for the field nr. 1 in Fig. 4-2 (a) and 300 V for the field nr. 2 in Fig. 4-2 (b). On one hand, the high RMS value at small concave distances (see runs A and E in Fig. 4-2 (a) and (b)) could be caused by the higher pressure that the crop transmits to the concave. Under this condition the excitation becomes higher and consequently the energy of the signal increases.

On the other hand, the high RMS values for high concave distances (see runs D and I in Fig. 4-2 (a) and (b)) could be explained by the fact that the material distribution, passing through the threshing zone, is irregular. In particular the crop is threshed in bunches instead of a coherent layer causing, probably, an increase of the bursts number in the time signal as shown in Fig. 4-3. At 10 mm concave distance the averaged amplitude of the signal is high as it can be noted in Fig. 4-3 (a) and (b). As consequence the RMS value is around 3 g. Increasing the concave distance to 30 mm, the averaged amplitude of the signal becomes smaller, if compared with the one at 10 mm condition. Due to the presence of the bursts in the signal, clearly visible in Fig. 4-3 (a) and (b), the RMS value is comparable with the ones obtained at 10 mm (around 3 g).

A detailed description of this phenomena it will be given later taking advantage of the angular analysis.

The Loudness and Tonality metrics (see Fig. 4-4 (a) and (b)) from the cabin microphone are insensitive to the concave distance variation.

As a matter of fact the excitation variation in function of the concave distance is not so manifest to be revealed by the microphone outside the cabin.

The AppEn trend depicted in Fig. 4-4 (d), shows a decrease as the concave distance increases. It means that the randomness of the signal decreases (together with the concave distance) with respect of its predictable part. This behaviour is probably linked to the number of bursts present in the signal. As it can be noted in Fig. 4-3, depicting a time segment of 5 seconds for two concave distance values (10 mm and 30 mm for the field nr. 1 in Fig. 4-3 (a) and for the field nr. 2 in Fig. 4-3 (b)), the number of burst increases at 30 mm causing an increase of the signal regularity (which means a decrease of the AppEn value).

It is worth noting that the AppEn, calculated over the time segments, characterized by the presence of bursts in the rectangular windows depicted in Fig. 4-3 (b), are 0.118 and 0.921 for the concave distances 10 mm and 30 mm respectively. These values, are similar to the ones indicated by the arrows in Fig. 4-4 (c) that are referred to the first 0.5 seconds (of the signals in Fig. 4-3 (b)), generally used to evaluate the AppEn for all the runs.

Observing the time frequency analysis in Fig. 4-3 (c) of the time signal in Fig. 4-3 (b) (at 30 mm), it can be noted that the frequency characterized by the highest amplitude is the one at 284 Hz corresponding to the 6th harmonic of the f_{bar} defined in Equation (4.1). Moreover, the amplitude of the $f_{bar} \times 6$ increases in correspondence of the bursts.

As wrote before, the Tonality metric from the cabin microphone is insensitive to the concave distance variations. The tonality algorithm has been applied also to the threshing microphone in order to verify if there is an influence of this operational parameter. Fig. 4-5 ((a) and (b)) and Fig. 4-6 show the trends of the Tonality metric, evaluated over the threshing and cabin microphones respectively, for test runs at 1420 rpm and average federate value of 400 V. The tonality metric from the threshing microphone decreases in a linear way as the concave distance increases.

The algorithm results depicted in Fig. 4-5 (b) show the presence of the tonal components. The SPL excess is higher at 15 mm than the one at 33 mm.

In contrast, the cabin microphone, is insensitive to the concave distance variation (see Fig. 4-6 (a)). It does not show relevant tonal components as confirmed from the algorithm results in Fig. 4-6 (b) where, not tonal components are extracted.

Comparing the Sound Pressure Level A-weighted in the frequency domain, calculated for the threshing and cabin microphones (see Fig. 4-7 (a) and (b)) and referred to the runs marked with the arrows at 15 mm concave distance in Fig. 4-5 (a) and Fig. 4-6 (a), it can be noted that the threshing microphone shows the characteristic frequency defined as following:

$$f_{bar} = \frac{2 \cdot n_{rotor}}{60} \quad (4.1)$$

where n_{rotor} is the nominal rotor speed in rpm and 2 is the number of rasp bars for each rotor section. Concerning the runs used the rotor speed is $n_{rotor} = 1350$ rpm and, consequently, $f_{bar} = 47.3$ Hz.

Moreover, the trend depicted in Fig. 4-5 (a) confirms the results achieved for the synthesized signal (in Chapter 3): increasing the amplitude of the f_{bar} and harmonics (caused by the concave distance reduction) the Tonality metric increases.

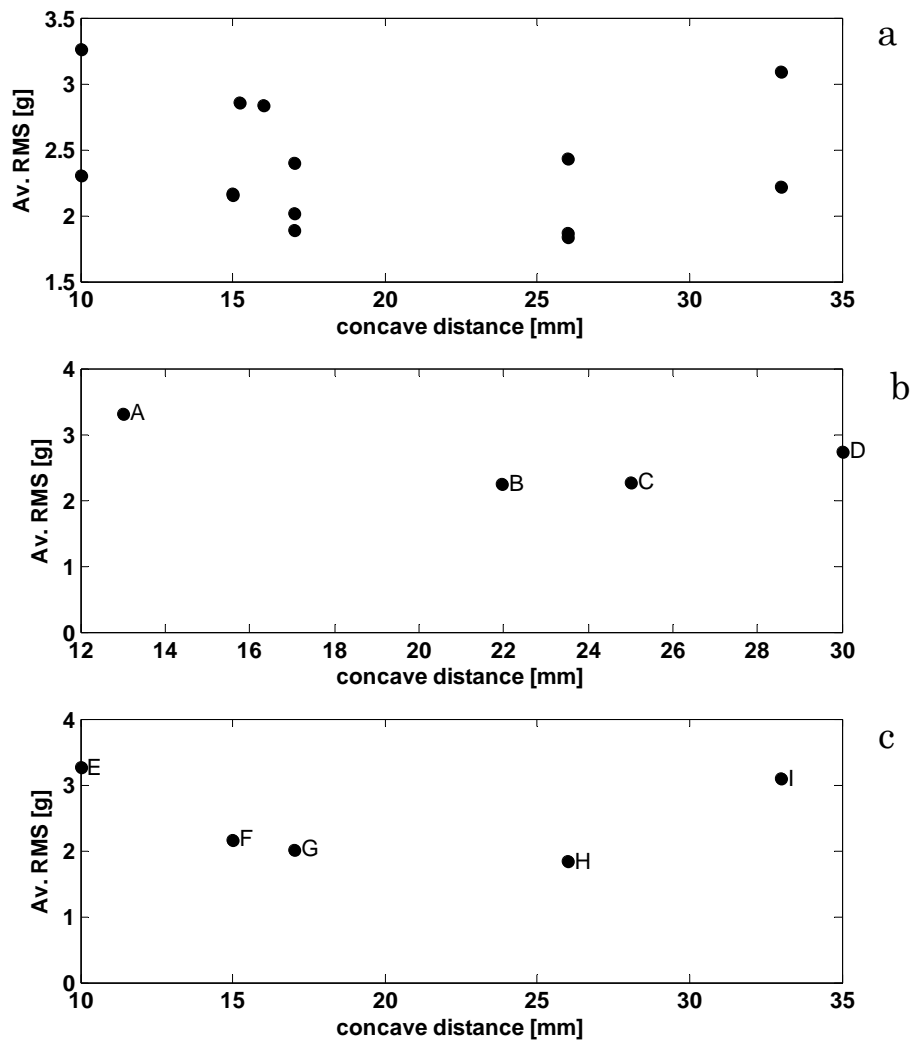


Fig. 4-2 – Av. RMS vs. concave distance: (a) Av. RMS at middle position, (b) wheat field tests nr. 1 and (c) wheat field tests nr. 2.

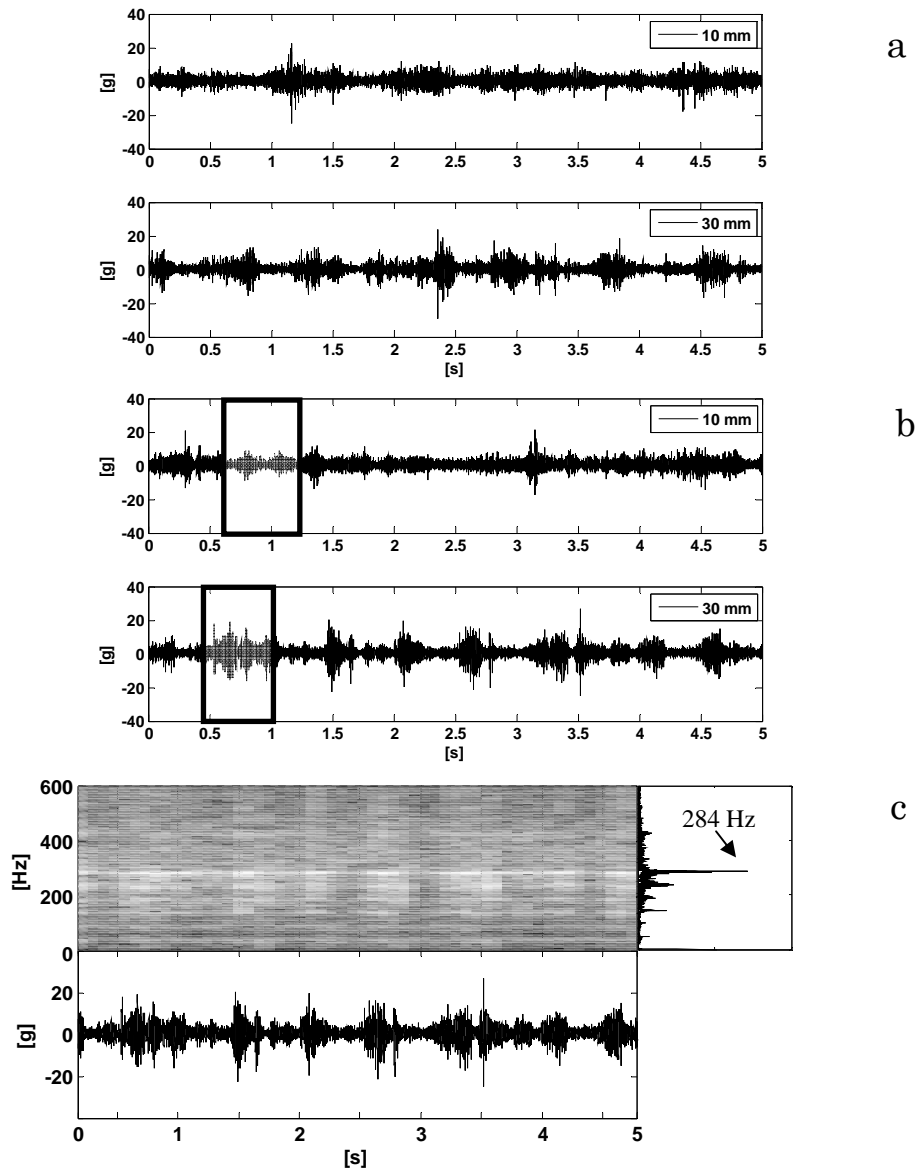


Fig. 4-3 – Time signals comparison for two concave distance values: (a) field tests nr. 1 (runs E and I), (b) field tests nr. 2 (runs A and D), (c) STFT of the signal depicted in (b).

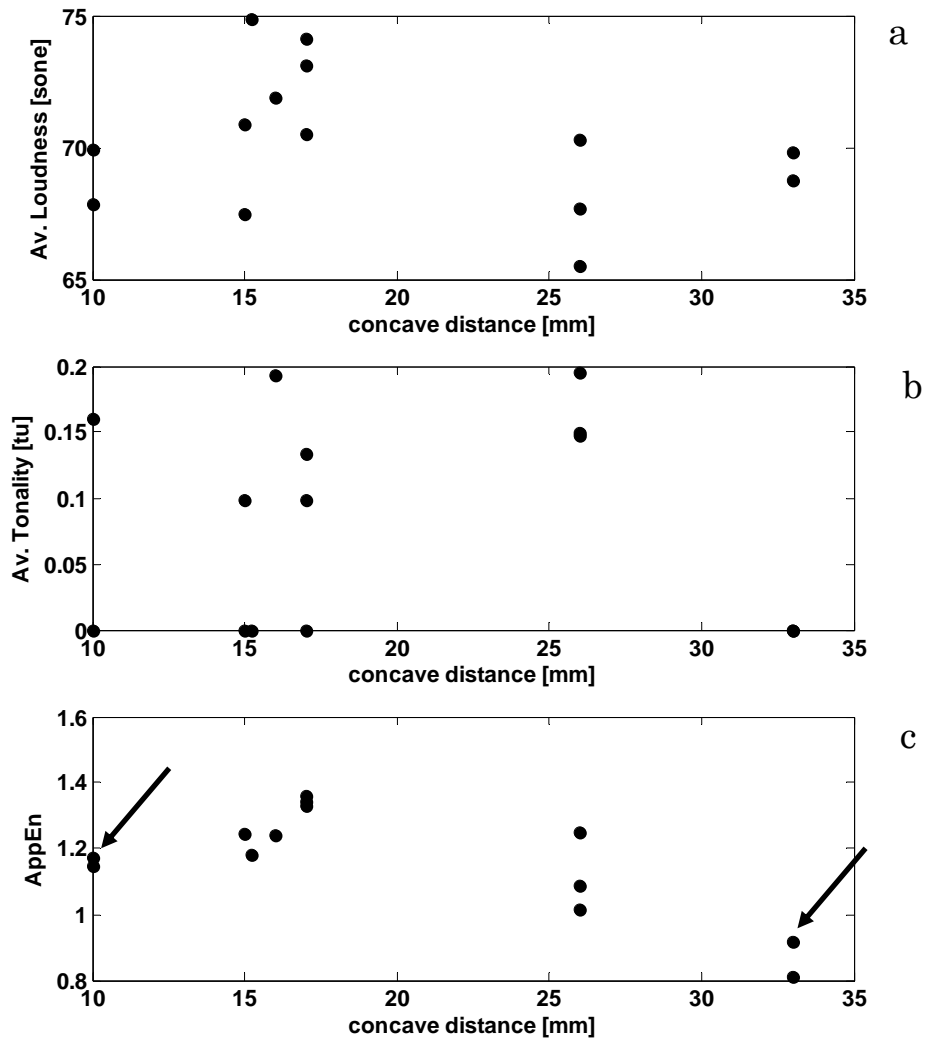


Fig. 4-4 - Features vs. concave distance (field nr. 2): (a) Av. Loudness cabin microphone, (b) Av. Tonality cabin microphone, (c) AppEn at the middle position.

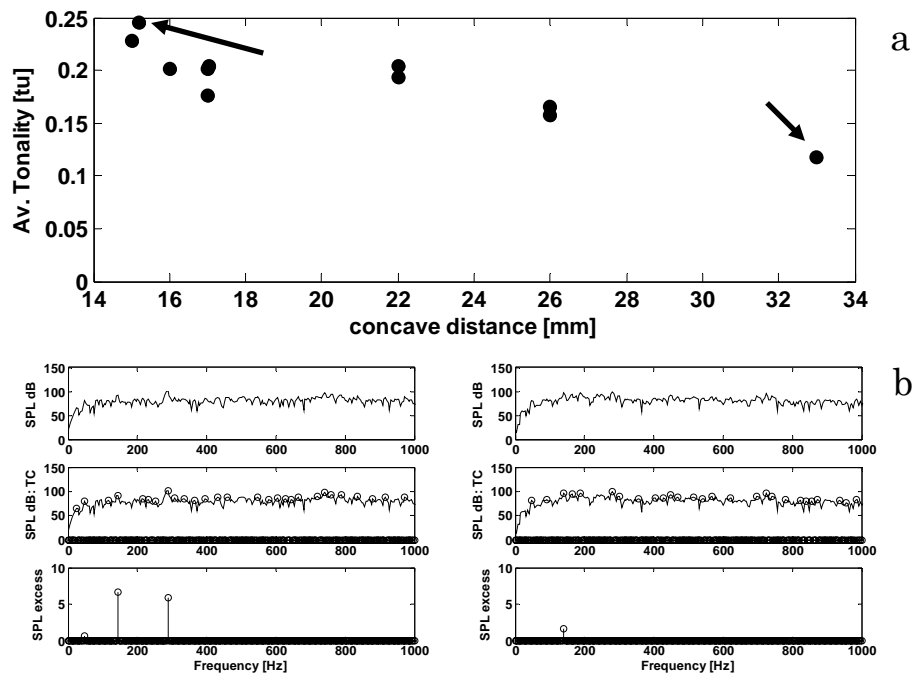


Fig. 4-5 – Threshing microphone, runs at 1420 rpm and 400 V average feedrate: (a) Tonality vs. concave distance, (b) tonality algorithm results for the runs marked by the arrows.

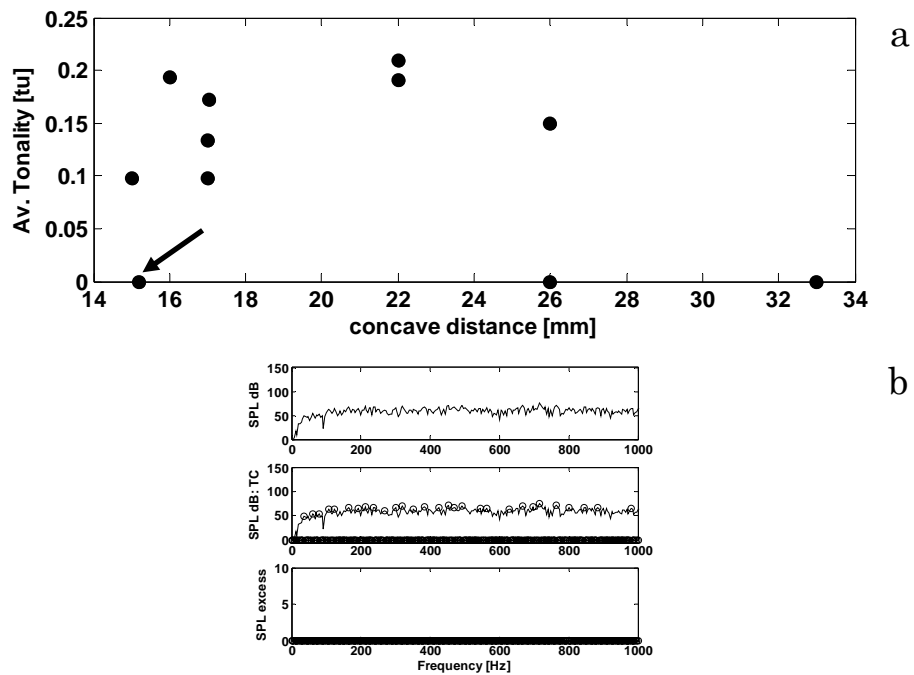


Fig. 4-6 – Cabin microphone, runs at 1420 rpm and 400 V average feedrate: (a) Tonality vs. concave distance, (b) tonality algorithm result for the run marked by the arrow.

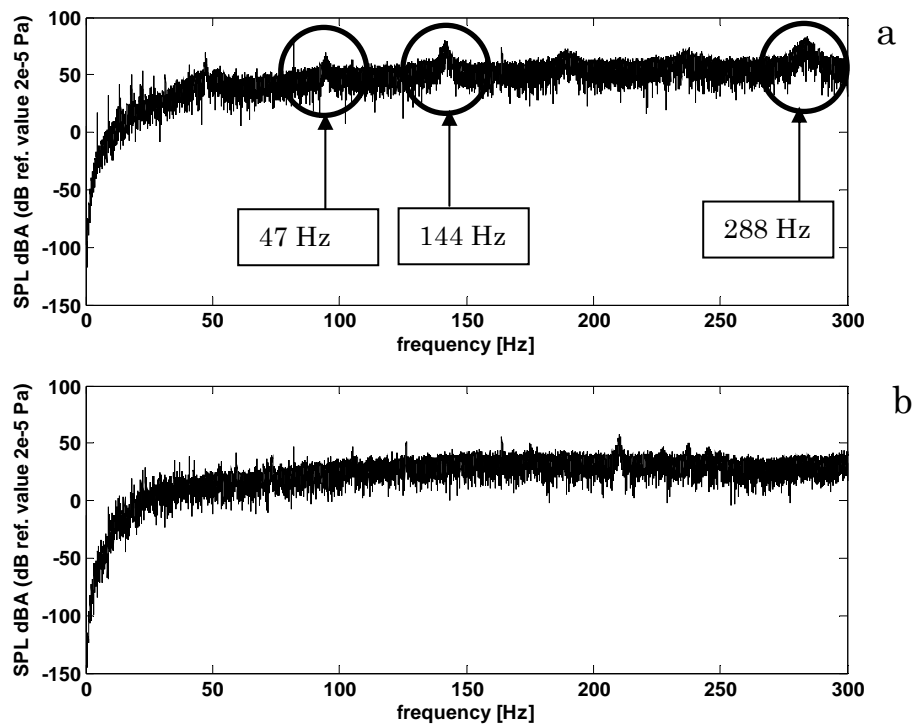


Fig. 4-7 – Sound pressure level at 15 mm concave distance: (a) process microphone, (b) cabin microphone.

4.3 Preliminary angular domain analysis

The aim of this paragraph is the analysis of the signal in the angular domain.

In particular, it will be described how the Time Synchronous Average (TSA) is estimated; then, a detailed analysis of the TSA signals (from the accelerometer and the microphones) will be conducted in order to localize all the events caused by the interaction of the threshing elements (i.e. rasp bars and friction elements).

4.3.1 Time Synchronous Average (TSA) estimation

In order to observe the vibration signal in one revolution of the rotor, the time domain averaging is combined with the order tracking.

Concerning the experimental data the time domain signal is re-sampled in the angular domain, in order to obtain the Time Synchronous Average (TSA) with respect to the rotor revolution. The processing parameters are summarized in Tab. 4-1.

The angular domain signals are calculated by an off-line interpolation post-processing: a tachometer signal (1 pulse/rev in Fig. 4-8 (a)) sampled at 6 kHz is used as a revolution reference in the field tests. In this case the order tracking will compensate for changes in the rotor rpm during the measurement, but not for changes inside the cycle.

The number of points used to calculate the TSA (in outdoor tests) is 120000 corresponding to a time segment of 20 seconds.

By using this method, the angular re-sampled signal is independent of the rotor speed variations as wrote before.

Tab. 4-1 – Order tracking parameters.

| Method | M (points per revolution) | Angular resolution [°] | Order resolution | Order max |
|--------------------------------------|---------------------------|------------------------|------------------|-----------|
| Matlab off line interpolation method | 512 | 0.70 | 1 | 256 |

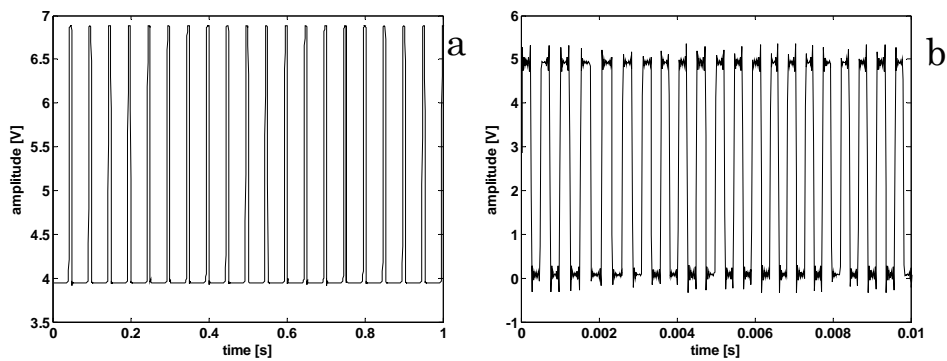


Fig. 4-8 – Tachometer signals: (a) 1 pulse/rev sampled at 6 kHz, (b) 100 pulse/rev sampled at 51 kHz.

In order to check the presence of speed variations in one cycle, a test run at 1350 rpm (141.37 rad/s) is used. The tachometer signal with 100 pulse/rev (see Fig. 4-8 (b)) sampled at 51 kHz is taken as angular reference.

Hereafter, in Fig. 4-9, the speed fluctuations for one cycle is reported; the mean value is 138.25 rad/s; the speed fluctuation is about the 5% of the mean value (at least at 3.6° resolution).

Based on this result it can be confirm that, inside the cycle, the speed variation could be considered negligible thus, the use of the tachometer signal at 1 pulse/rev could be correct in order to obtain a reliable TSA signal.

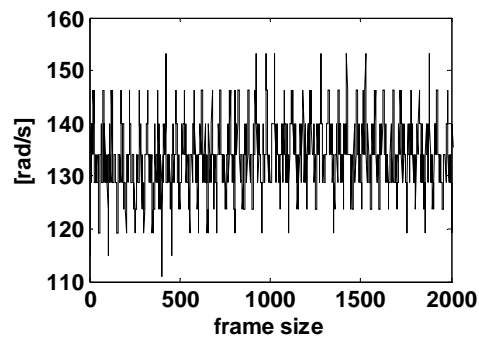


Fig. 4-9 – Instantaneous speed fluctuations.

4.3.2 Identification of the periodical interaction events

The angular position of the elements, like rasp bars and friction elements, can be obtained from the drawing of the rotor used for the field tests. Fig. 4-11 shows the frontal view of the rotor with two rasp bars (RB) and friction elements (FE) for each section equally spaced from each others of 180 degrees.

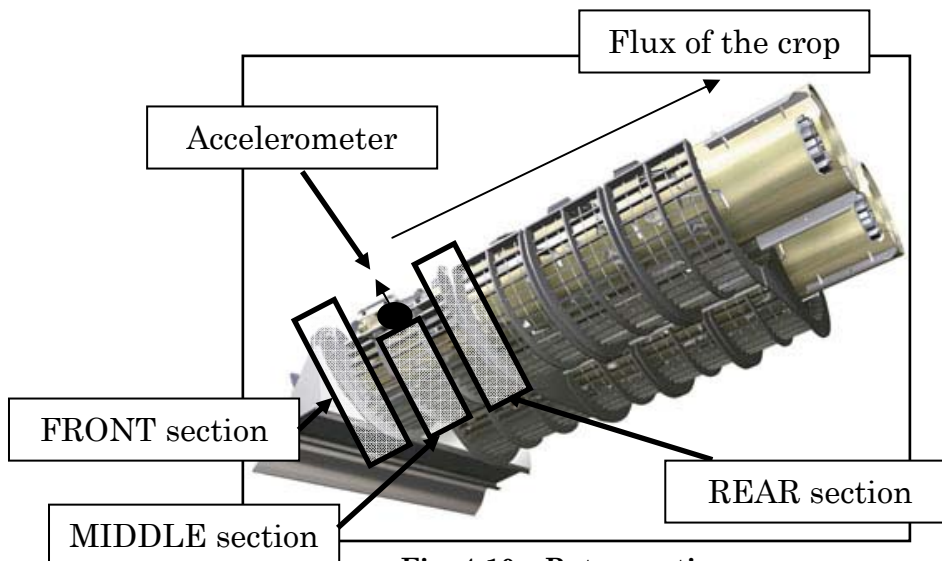


Fig. 4-10 – Rotor sections.

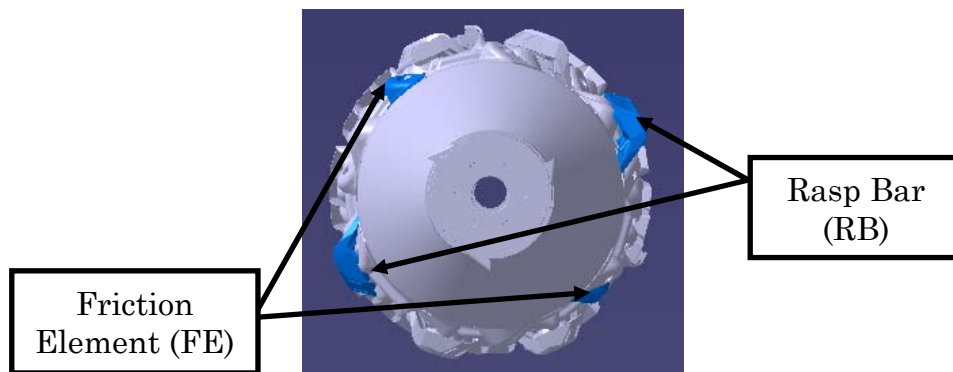


Fig. 4-11 – Field tests rotor drawing.

Keeping as reference the signals of the rasp bar rear and front (see Fig. 4-12) it is possible to recognize the correct position of the rasp bar and friction elements in the accelerometer and microphone signals.

In particular, observing the signal from a test run carried out with 1420 rpm, and 10 mm concave distance (see Fig. 4-13), it can be observed that the concave middle radial and the threshing microphone middle TSA signals are sensitive not only to the rasp bars but also to the friction elements. On the other hand, the threshing microphone TSA signal is only sensitive to the presence of the rasp bars thus, not reliable to show all the interactions between rotor and concave.

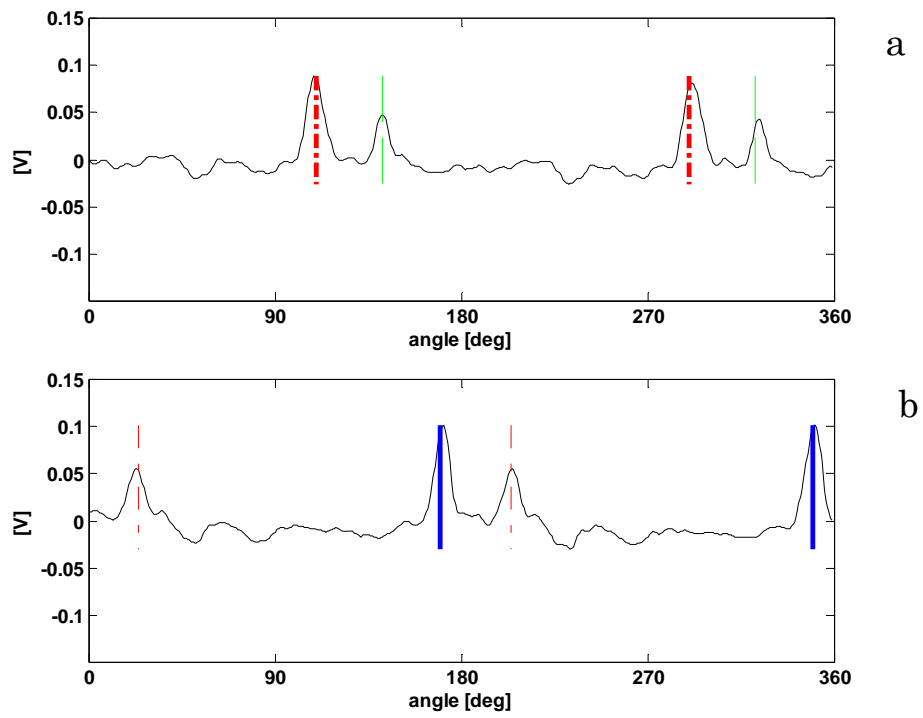


Fig. 4-12 - Field test nr. 1, test run: (a) rasp bars signals rear section and (b) front section.

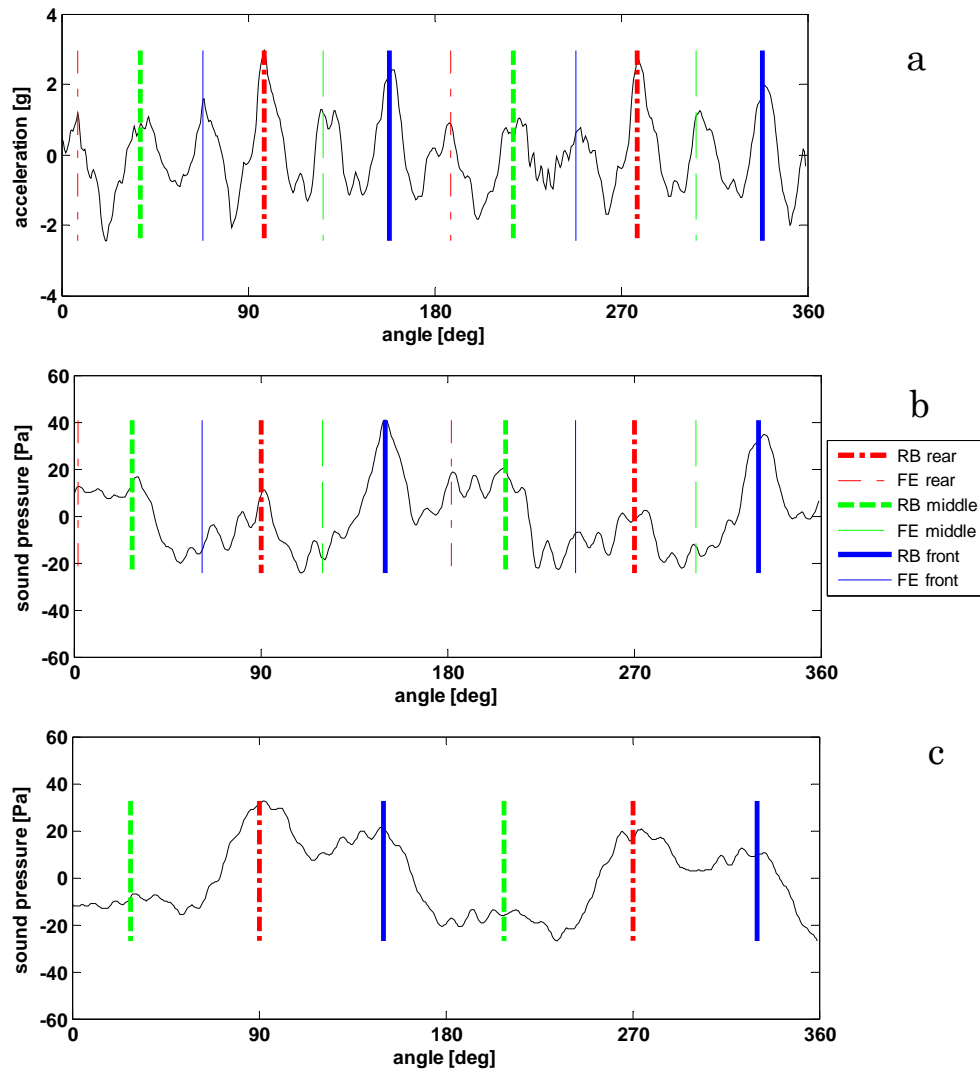


Fig. 4-13 – Field test nr. 1 test run: (a) concave middle radial TSA signal, (b) threshing microphone middle TSA signal, (c) threshing microphone right TSA signal.

4.3.3 Effect of the crop in the threshing zone

Experiments have been conducted comparing the conditions with and without crop passing through the threshing zone. The goal is to see if the main source of noise and vibration comes from the crop which is pushed against the concave by the rasp bars and the friction elements. It can be observed that, the accelerometer signal in Fig. 4-14 (a), is only sensitive to the crop because the amplitude of the TSA signal is almost zero in the tests without crop passing through the machine. In contrast, the microphone, is not only sensitive to the crop, but also to the airborne noise generated by the rasp bars as shown in Fig. 4-14 (b).

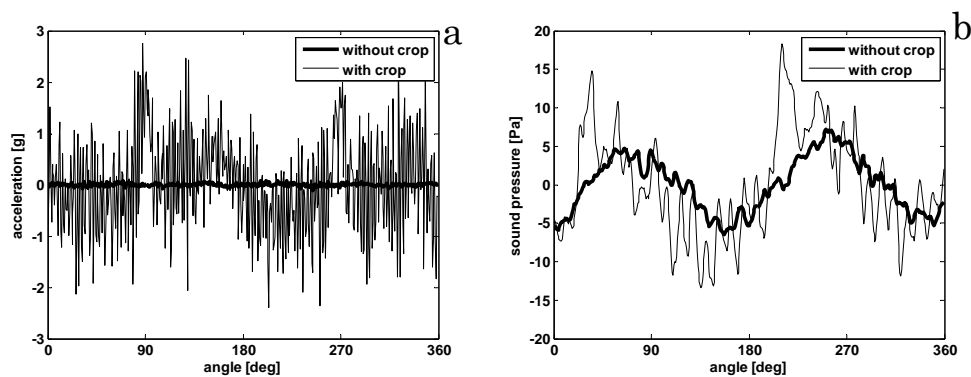


Fig. 4-14 – Comparison based on TSA signals with and without crop for field tests (a) concave middle radial, (b) threshing microphone right.

4.4 Threshing process interpretation by means of the cyclostationary approach

The aim of this paragraph is the detailed description of the process by using the cyclostationary approach which takes advantage of the angular domain analysis.

Moreover, the separation of the signal into the deterministic and residual parts will be treated in order to describe the different phenomena characteristic of the threshing process.

The description of the process starts from the correlation graphs in function of the concave distance. Hereafter, Fig. 4-15 (a) and (b) depict the trend of the RMS from the TSA signal calculated over a time segment of the same length (20 seconds) of the one used to obtain the feature in the time domain. Confirming what found from the correlation in the time domain, reported in paragraph 4.2.2, a concavity trend is clearly visible.

In order to describe the RMS trend in function of the concave distance variation, the comparison between the TSA signals for different distances, constant rotor speed and capacity (feedrate) is analyzed.

As already described in the Chapter 2, the accelerometer is mounted on the concave at the middle section of the threshing zone (see Fig. 4-10). The concave distance is the radial distance between rotor and concave as shown in Fig. 4-16 (a) and (b), depicting the minimum and the maximum concave opening respectively.

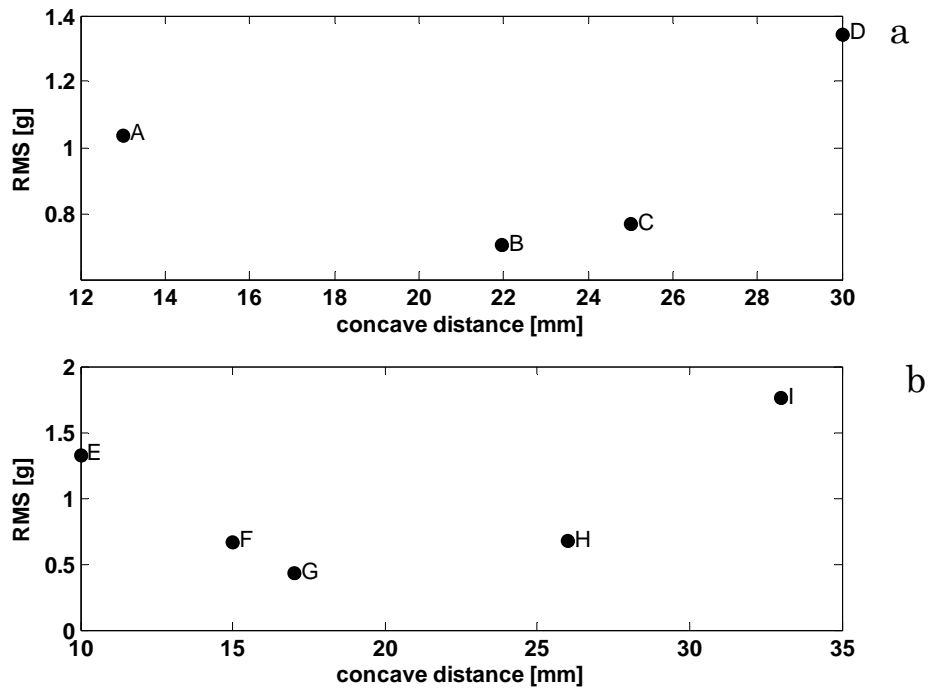


Fig. 4-15 – RMS TSA vs. concave distance: (a) field test nr. 1 and (b) field test nr. 2.

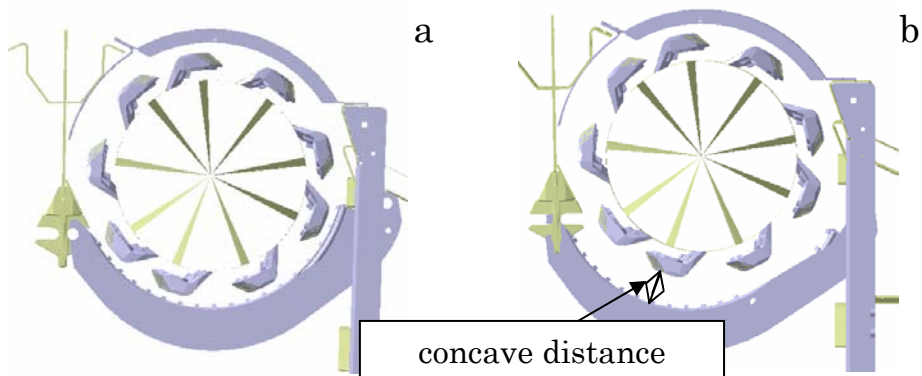


Fig. 4-16 – Front view of the threshing zone: (a) minimum concave distance, (b) maximum concave distance.

A first analysis of the accelerometer TSA signals in Fig. 4-17 shows that the amplitude of all the events is high for the runs at 10 mm and 30 mm concave distances. At 22 mm (see Fig. 4-17 (a)) and 25 mm (see Fig. 4-17 (b)), it seems that the peaks caused by the threshing elements (i.e. rasp bars and friction elements) have similar amplitudes.

In particular, the peaks of the rasp bars front and rear (RBF and RBR in Fig. 4-17 (a) and (b)) show higher amplitude values than the ones of the middle section (RBM).

This phenomena, could be caused by the discontinuity of the material at the beginning and at the end of the threshing section (front (F) and rear (R) sections in Fig. 4-18).

At the front section the material, entering in the threshing zone, is strongly accelerated against the concave, causing a high vibration level as shown in the peaks marked by RBF (Rasp Bar Front) in Fig. 4-17 (a) and (b).

Passing through the middle section (M in Fig. 4-18) the flux of material could be subjected to a stabilization probably due to the fact that, before and after this section, there is a continuity of material. Moreover, the geometry of the rotor and the concave distance is the same of the front and rear sections.

At the rear section (see Fig. 4-10), there is a transition region between the threshing and the separation zones. The separation zones is characterized by fixed concave distance and different geometry of the blades mounted on the rotor. Thus, the material could be again subjected to a strong acceleration that probably causes a high vibration level as shown in the peaks marked by RBR (Rasp bar Rear) in Fig. 4-17 (a) and (b).

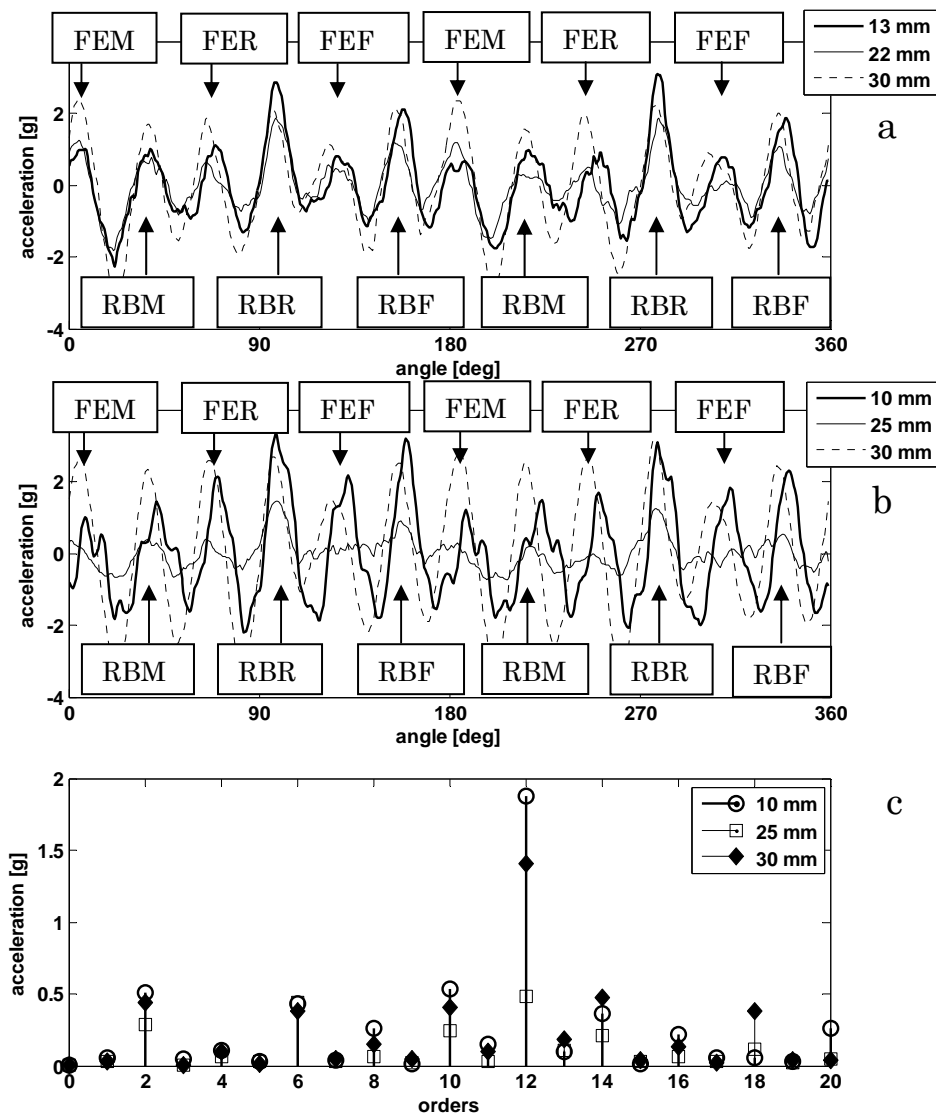


Fig. 4-17 – Influence of the concave distance on the TSA signal: (a) field test nr.1 (A, B and D), (b) field tests nr. 2 (E, G and I) and (c) FFT of the TSA signals in (b).

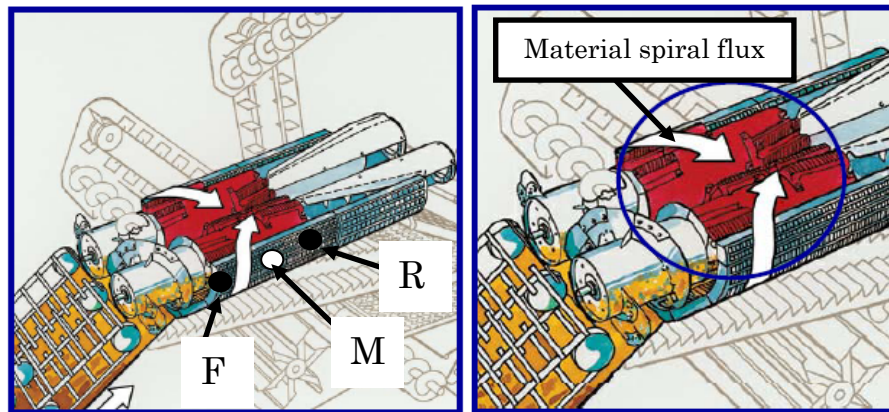


Fig. 4-18 – Material direction inside the threshing zone.

Going further, opening the concave distance (from 13 mm to 30 mm as shown in Fig. 4-17 (a) and (b)) it can be noted that the RMS of the TSA signal increases as depicted in Fig. 4-15.

On one hand, the random sliding interaction of the material with itself and the mechanical components (rotor and concave) would give a vibration signal roughly proportional to the local pressure, and thus higher when the rasp bar is close to the concave at the measurement point (see Fig. 4-19 (a) and Fig. 4-20).

Opening the concave at about 22 mm, the layer becomes looser but the rotor has still enough grip on the crop to move the whole layer rather easily with lower acceleration transferred to the concave as consequence (see Fig. 4-17 peaks at about 22 mm).

On the other hand, increasing the distance, the rotor loses the grip on the crop (see Fig. 4-19 (b)) and consequently it is threshed in bunches instead of a regular layer. When the bunch of material is thick enough to be grabbed by the rasp bars on the rotor, it is accelerated against the concave causing an increase of the acceleration amplitude clearly visible in the TSA signals of Fig. 4-17 (a) and (b) and consequently, on the RMS increases in Fig. 4-15 for runs D and I. The FFT of the TSA depicted in Fig. 4-17 (c) shows that the amplitude of the order 12 is the highest for the settings 10 and 30 mm.

It is worth noting that the order 12 corresponds to the frequency 284 Hz depicted in Fig. 4-3 (c).

Thus, the increase of the TSA signal amplitude, at 30 mm concave distance, could be linked to the bursts observed in the time signal as shown in the previous Fig. 4-3 (a) and (b).

Moreover, if the crop is threshed in bunches of material, the layer passing through the threshing zone should be characterized by high turbulence as wrote before. An explanation of the material turbulence could be given by observing the residual signal (obtained after subtracting the TSA to the raw signal).

In particular, the cyclic power of the residual signal at 30 mm concave distance (see Fig. 4-21 (a) and (b)), shows a clear second order cyclostationary component periodicity at the cyclic order 2 and harmonics which is more clear than the one observed at 10 mm. The 6th order, is clearly visible and it is linked to the six rasp bars spirally mounted over the length of the threshing zone. The local pressure increment (at the measurement point) caused by the material bunches compression, at high concave distance, could give the amplitude modulation of the random residual component as confirmed by the increase of the characteristic cyclic order and harmonics in the cyclic power of the residual signal at 30 mm, depicted in Fig. 4-21 (a) and (b).

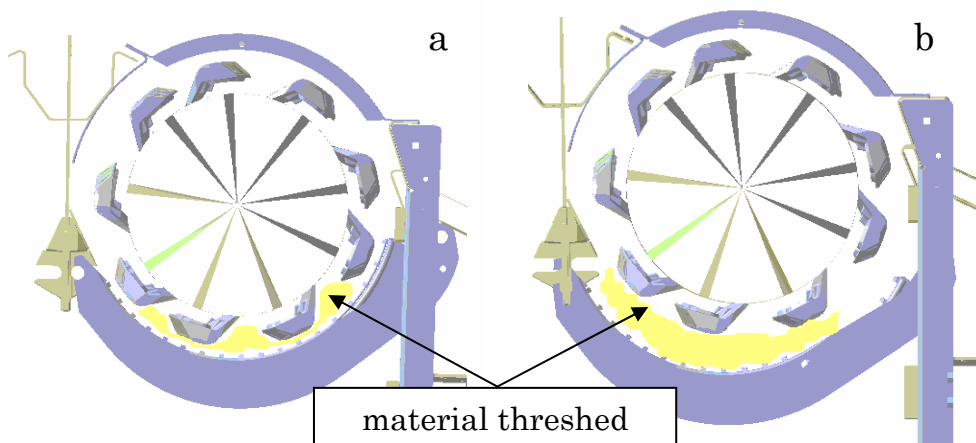


Fig. 4-19 – Material distribution for: (a) minimum concave distance and (b) maximum concave distance.

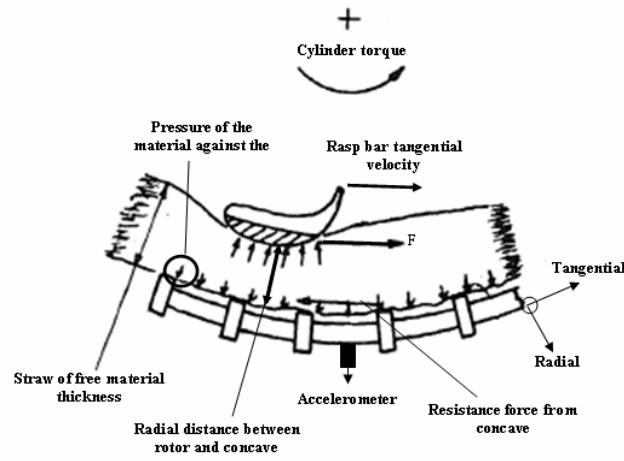


Fig. 4-20 – Pressure given by the material compression on the concave.

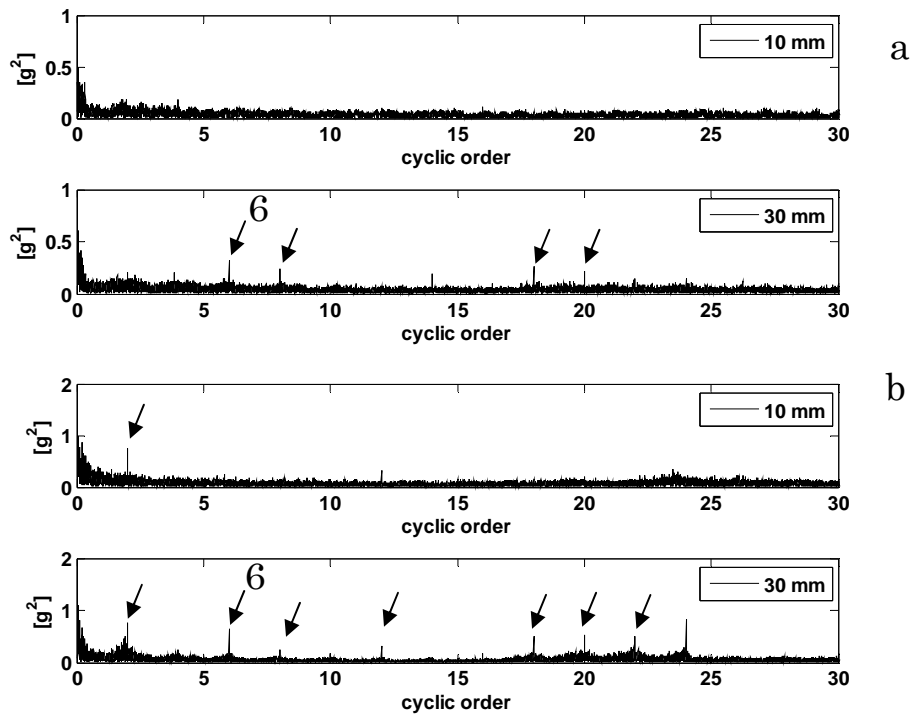


Fig. 4-21 – Cyclic power: (a) field test nr. 1 and (b) field test nr. 2.

4.5 Correlation between signal features and efficiency parameters

This paragraph shows the correlations between the RMS calculated on the time and angular domains, the ICS_{nx} obtained from the cyclostationary approach and the efficiency parameters, such as threshing loss and broken grain percentage, evaluated only for some of the runs carried out during the field tests.

The goal is to investigate the possibility to describe and predict the process efficiency by means of on-line vibration measurements. The efficiency parameters, listed in Chapter 2, try to numerically describe the efficiency of the threshing process.

The correlation coefficient, used as reference to evaluate the correlation is the R square given by the following Equation:

$$R(i, j) = \frac{C(i, j)}{\sqrt{C(i, i) \cdot C(j, j)}} \quad (4.2)$$

Where R is a matrix of correlation coefficients related to the covariance matrix C.

It is well known, from literature [16] that, an increase of the concave distance gives a bigger amount of threshing losses. Moreover, from [17] it can be noted that the un-threshed grains (threshing loss) are caused by the first part of the threshing unit (threshing zone until 0.4 m in Fig. 4-22) which is the rotor section under investigation.

Thus, it is reasonable to think that the concave distance variation of the threshing zone is the major effect that influence the amount of threshing loss at the end of the process. Moreover, as the concave distance decreases the aggressiveness of the process becomes higher causing an increment of the amount of broken grains.

With the aim at pointing out the correlations among the vibration features and finding the correct one, useful to predict the increase or decrease of the threshing loss, several trends, from the time and angular domains, will be reported hereafter.

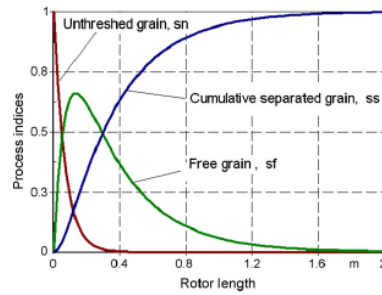


Fig. 4-22 – Variation of un-threshed grains in an axial unit.

The following paragraphs will show the correlation among the vibration features from the time and angular domains and the efficiency parameters.

4.5.1 Time domain features

4.5.1.1 Threshing loss correlation

The runs have been conducted with constant rotor speed of 1420 rpm and different feedrate values for the two fields: the settings are summarized in Tab. 4-2. In the first wheat field (see Fig. 4-23) tests the average feedrate is 450 V corresponding to a machine ground speed of 6 km/h. In the second field test (see Fig. 4-24) the average feedrate value is 300 V corresponding to a ground speed 4 km/h.

Tab. 4-2 - Machine settings wheat field tests.

| Field nr. | Rotor speed [rpm] | Feedrate value [V] |
|-----------|----------------------|-----------------------|
| 1 | 1420 | 450 |
| 2 | 1420 | 300 |

It is interesting to observe a very good correlation, with $R^2 = 0.90$ for the field number 1, between the Av. RMS and the threshing loss (see Fig. 4-23).

On the other hand, the result from the field number 2 are not reliable and characterized by $R^2 = 0.45$. In particular, as it will be shown in the correlation from TSA RMS, the minimum RMS value does not give correct indication about the optimal setting for the machine because it does not correspond with the point characterized by the minimum amount of threshing loss as shown in Fig. 4-23 (b) and Fig. 4-24 (b) (marked by the big arrow).

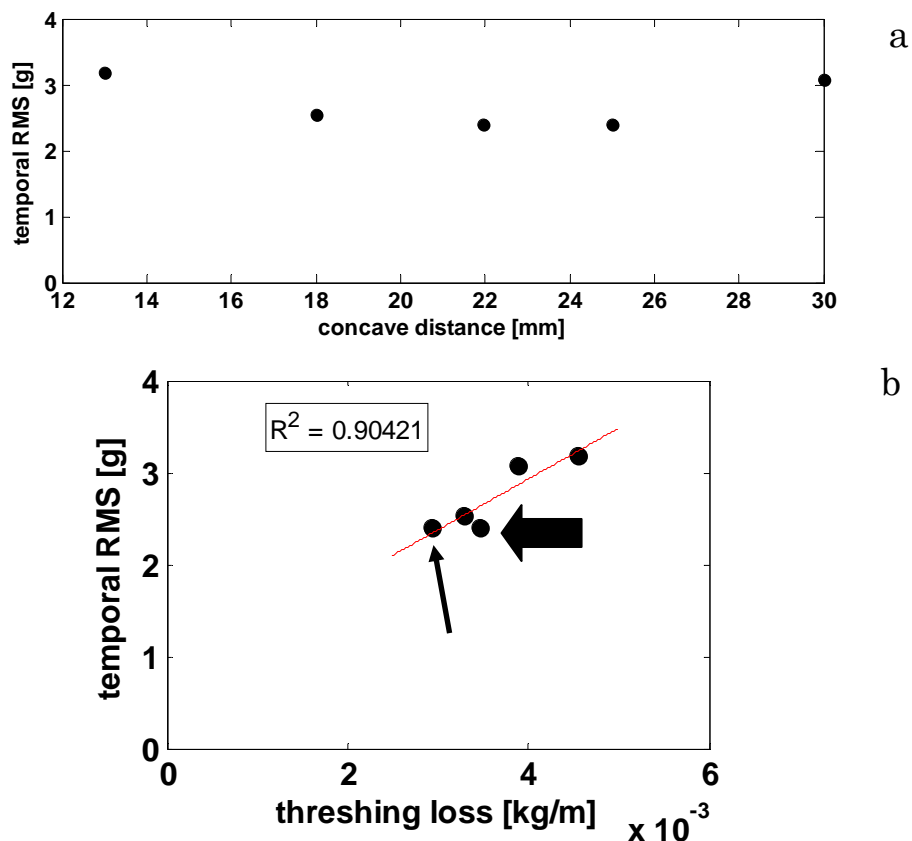


Fig. 4-23 - Efficiency parameter: threshing loss for the field nr. 1. (a) RMS vs. concave distance and (b) RMS vs. threshing loss with $R^2 = 0.90$.

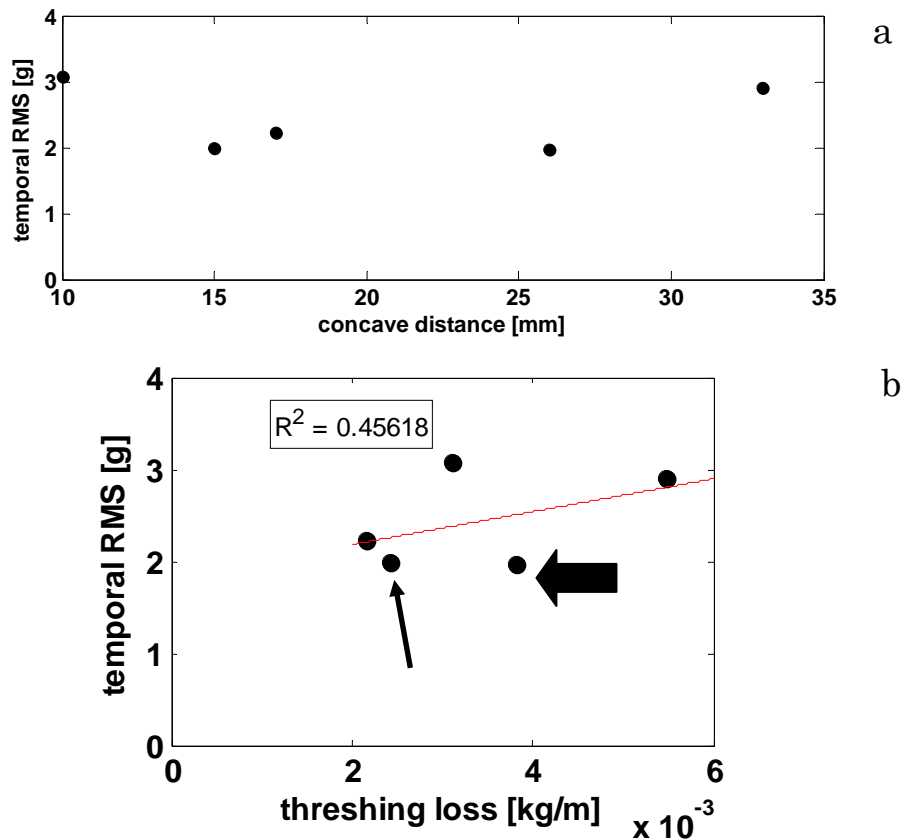


Fig. 4-24 - Efficiency parameter: threshing loss for the field nr. 2. (a) RMS vs. concave distance and (b) RMS vs. threshing loss with $R^2 = 0.45$.

4.5.1.2 Broken grain percentage correlation

The broken grain percentage, estimated for the corn crop, is evaluated on the total loss amount collected from the machine at the end of the process.

Then, in order to objectify the correlation the R^2 coefficient is calculated between the RMS and the broken grain percentage as done before for the threshing loss correlation.

The runs settings are depicted in the following table:

Tab. 4-3 – Machine settings corn field tests.

| Field nr. | Rotor speed [rpm] | Feedrate value [V] |
|-----------|----------------------|-----------------------|
| 1 | 700 | 1500-1700 |
| 2 | 360 | 800-900 |

From the correlations depicted in Fig. 4-25 and Fig. 4-26, it can be supposed that a decrease of the concave distance, which means a major aggressiveness of the process on the crop, causes an increase of RMS. High RMS values correspond to a bigger amount of broken grains, visible in Fig. 4-25 and Fig. 4-26 depicting set of runs not comparable because the rotor speed and the feedrate are different. This hypothesis is confirmed observing the R^2 values equal to 0.95 and 0.87 for the field 1 and 2 respectively.

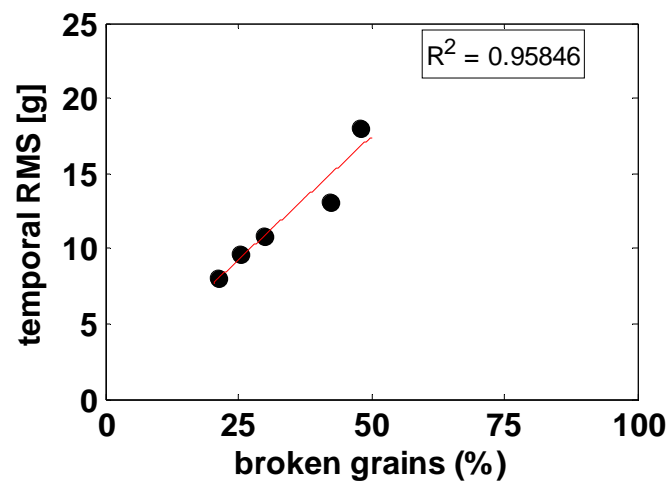


Fig. 4-25 - Efficiency parameter: broken grain for the corn field nr. 1:
Av. RMS vs. broken grain with $R^2 = 0.95$.

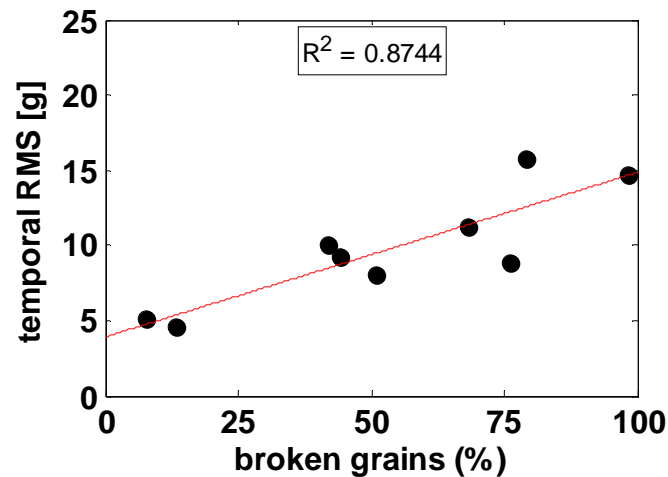


Fig. 4-26 - Efficiency parameter: broken grain for the corn field nr. 2: Av. RMS vs. broken grain with $R^2 = 0.87$.

4.5.2 Angular domain features

4.5.2.1 Statistical parameters from TSA signals

➤ RMS vs. threshing loss correlation

The correlation with the threshing loss is shown in the following Fig. 4-27 and Fig. 4-28. The runs are the same analyzed for the time domain correlations. The parameters are summarized in Tab. 4-2. As expected the minimum point shifts to high concave distances because the ground speed increase: with 4 km/h the concave setting is 18 mm (see Fig. 4-28) while increasing to 6 km/h the minimum concave distance shift to values around 22 mm (see Fig. 4-27).

Compared to the correlation in the time domain (see Fig. 4-23 and Fig. 4-24) the minimum value of the RMS (about 0.5 m/s^2) corresponds quite well to the minimum value of the threshing loss per meter (about 0.003 kg/m).

Moreover, it is important to observe, that the threshing loss value is also influenced by the quantity of material entering in the threshing zone: reducing the capacity the minimum value of threshing loss per meter decreases going from 0.003 kg/m to 0.002 kg/m.

The RMS from the TSA is correlated quite well with the threshing loss. In particular the minimum point detected in the trend of the RMS vs. concave distance could be taken as the optimum setting (concave distance) because it corresponds to the minimum amount of threshing loss per meter. It is not possible to achieve the same results by analysing the correlation in the time domain because, the position of the minimum RMS value does not correspond to the minimum threshing loss value.

In the following table a comparison between the R^2 is reported: it can be noted that the correlations in the time domain show different R^2 values, thus not reliable.

Tab. 4-4 – Comparison between R^2 values from correlation in the time and angular domains.

| Field nr. | R^2 time domain | R^2 angular domain |
|------------------|-------------------------------------|--|
| 1 | 0.93 | 0.66 |
| 2 | 0.47 | 0.80 |

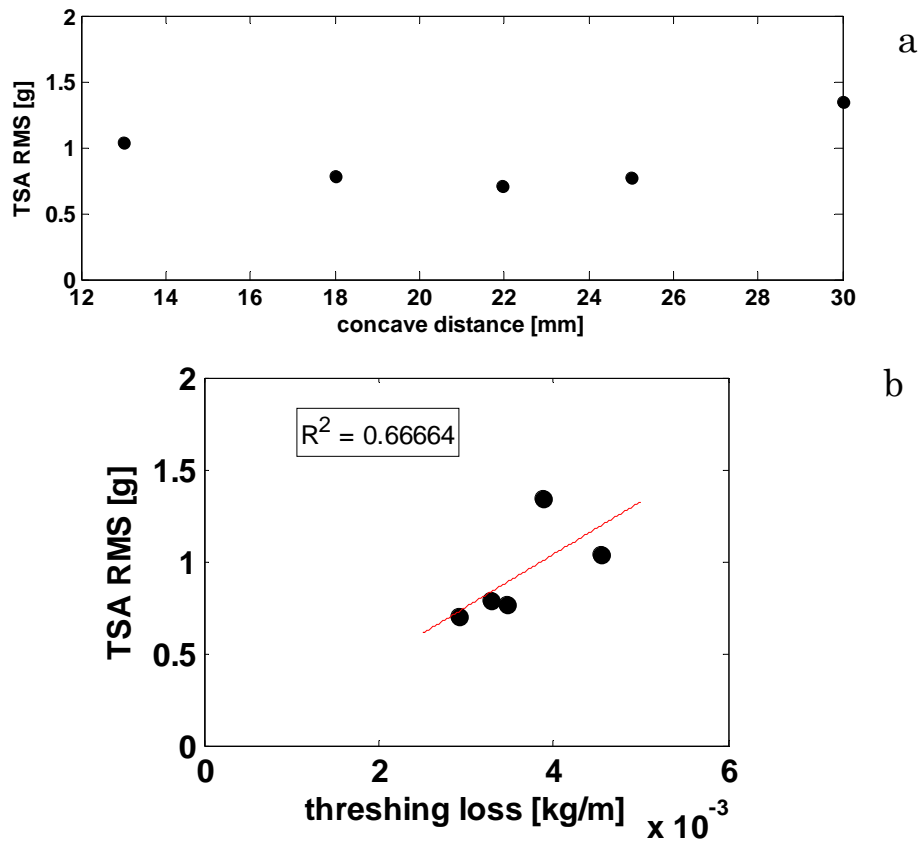


Fig. 4-27 - Efficiency parameter: threshing loss for the field nr. 1. (a) RMS TSA vs. concave distance and (b) RMS TSA vs. threshing loss with $R^2 = 0.66$.

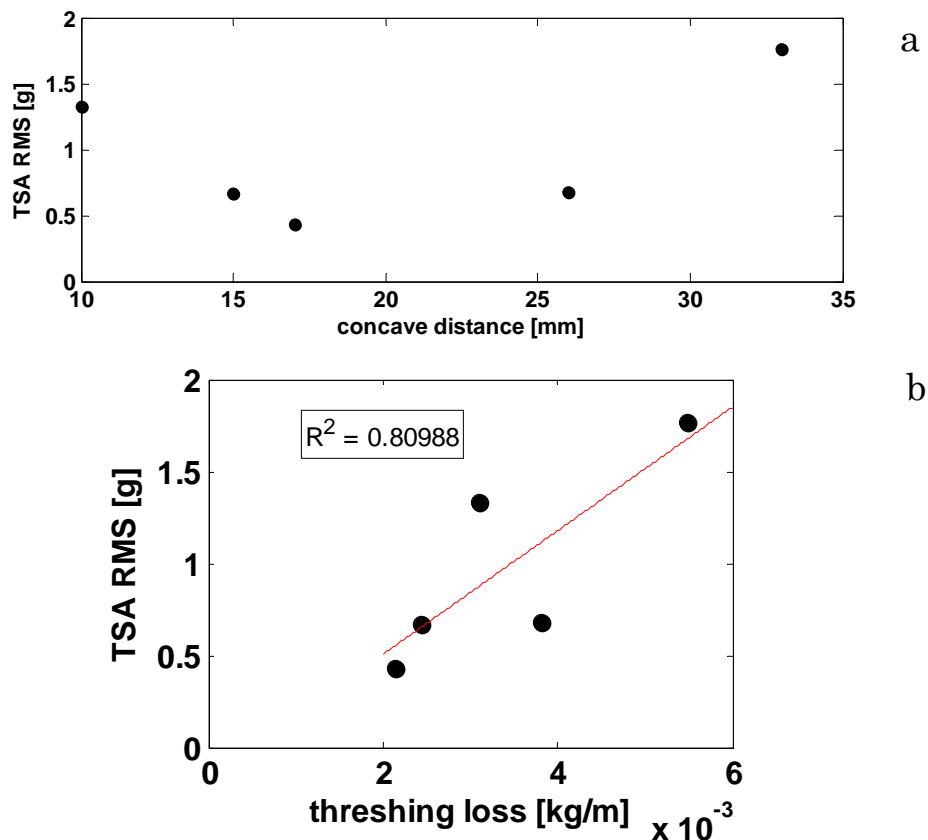


Fig. 4-28 – Efficiency parameter: threshing loss for the field nr. 2: (a) RMS TSA vs. concave distance and (b) RMS TSA vs. threshing loss with $R^2 = 0.80$.

In order to verify the capacity influence over the minimum point, two more correlation graphs have been reported in Fig. 4-29 (a) and (b) depicting the correlation from several test runs carried out with 1420 rpm rotor speed and different average feedrate values. The processed crop is wheat, for Fig. 4-29 (a), while for the Fig. 4-29 (b), is barley.

In particular, it can be noted that the minimum point is still present and it moves to high concave distances as the increase of the feedrate value.

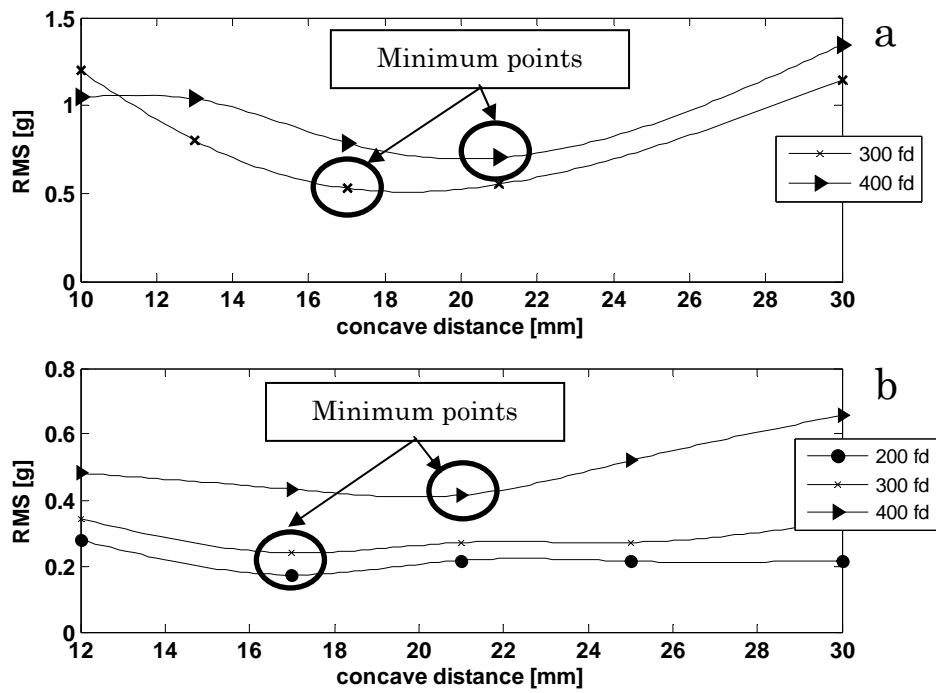


Fig. 4-29 - Influence of the feedrate over the minimum point detected on the RMS correlation vs. concave distance, (a) wheat field tests, (b) barley field tests.

➤ RMS vs. broken grains correlation

Hereafter, Fig. 4-30 and Fig. 4-31 depict the trends of the TSA RMS with the broken grain percentage. Confirming what found in the time domain, as the concave distance decreases the energy given by the process to the crop increases (as wrote before) giving a large amount of broken grains

Looking the R^2 values in the following table it is possible to confirm that the feature from both domains are linked very well to the amount of damaged kernels.

Tab. 4-5 – Comparison between R^2 values from correlation in the time and angular domains.

| Field nr. | R^2 time domain | R^2 angular domain |
|-----------|-------------------|----------------------|
| 1 | 0.87 | 0.96 |
| 2 | 0.95 | 0.86 |

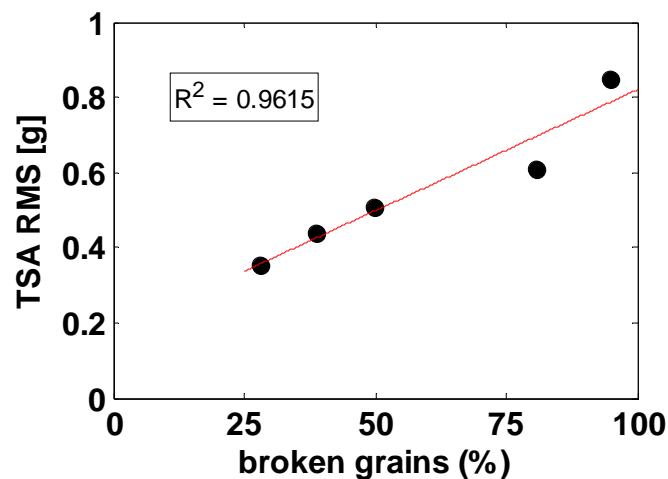


Fig. 4-30 - Efficiency parameter: broken grain for the corn field nr. 1: RMS TSA vs. broken grain with $R^2 = 0.96$.

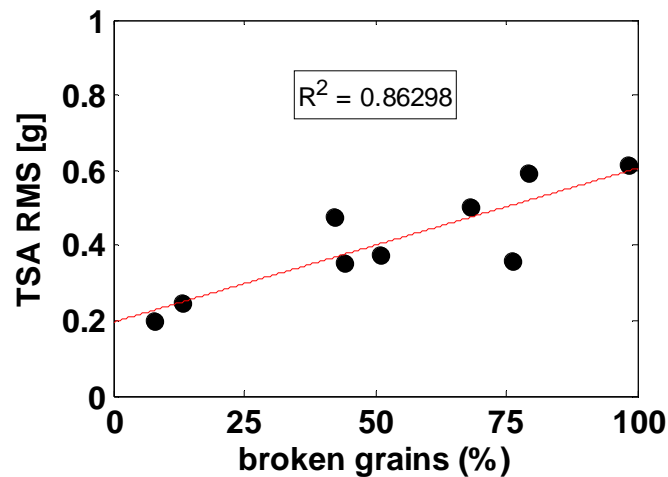


Fig. 4-31 - Efficiency parameter: broken grain for the corn field nr. 2: RMS TSA vs. broken grain with $R^2 = 0.86$.

4.5.2.2 Features from the cyclostationary approach

The indicators of cyclostationarity have been introduced in order to characterize the deterministic (TSA) and the residual parts (obtained by subtracting the TSA to the raw signal as depicted in Chapter 3) of the acceleration signals at the middle position. The ICS_{nx} is useful to verify if some correlations exist among the first and the second cyclostationary contents and efficiency parameters.

Before to proceed with the correlations, all the results obtained from the synthesized signal (in Chapter 3) must be compared with the numerical results in order to check the influence of the concave distance over the ICS_{nx} for $n = 1, 2$.

Hereafter the ICS_{nx} for $n = 1, 2$ have been calculated for four TSA signals at 1420 rpm rotor speed (the runs are referred to the signals in Fig. 4-17 (b)). The set of the cyclic frequencies is kept until 284 Hz corresponding to the order 12. The same range has been considered for the ICS calculation over the synthesized signal.

Tab. 4-6 - Signal parameters and ICS values.

| Concave distance [mm] | Feedrate | ICS_{1x} | ICS_{2x} |
|------------------------------|-----------------|-------------------------|-------------------------|
| 10 | 300 | 30.51 | 1.16 |
| 17 | 300 | 9.49 | 1.19 |
| 26 | 300 | 27.04 | 1.28 |
| 30 | 300 | 56.84 | 1.29 |

As it can be noted from Tab. 4-6, the trend of the ICS_{1x} is confirmed by the experimental data. At high amplitude of the TSA signal (at 10 mm and 30 mm as shown in Fig. 4-17 (b)) corresponds an increase of the ICS_{1x} .

The ICS_{2x} is characterized by small variability, with respect the trend of the ICS_{2x} depicted in Tab. 3-2. It increases from 1.16 to 1.29 going from 10 to 30 mm. This trend is linked to the fact that the second order cyclostationary component is predominant at high concave distances as shown in Fig. 4-21 which means that (at 30 mm concave distance) the amplitude modulation increases.

➤ ICS_{nx} vs. threshing loss correlation

The ICS_{1x} feature confirms the results achieved for the RMS in function of the threshing loss (as depicted in Tab. 4-7). On the other hand, the ICS_{2x} cannot be considered a reliable feature because there is a variability in the R^2 values (0.58 for the field nr. 1 and 0.16 for the nr. 2).

Tab. 4-7 - R^2 values from RMS and ICS correlation.

| Field nr. | R^2 RMS | R^2 ICS _{1x} | R^2 ICS _{2x} |
|--------------|-----------|-------------------------|-------------------------|
| 1 | 0.66 | 0.57 | 0.58 |
| 2 | 0.80 | 0.95 | 0.16 |

➤ ICS_{nx} vs. broken grains correlation

The same comparison shown in the previous paragraph has been done for the broken grain percentage. The ICS_{nx} feature seems not to be linked to the broken grain percentage except for the ICS_{2x} from the field nr. 2 that shows a $R^2 = 0.75$. This result is not confirmed from the field nr. 1. Thus, it is not taken as reference because not repetitive.

Tab. 4-8 – R^2 values from RMS and ICS correlation.

| Field nr. | R^2 RMS | R^2 ICS _{1x} | R^2 ICS _{2x} |
|--------------|-----------|-------------------------|-------------------------|
| 1 | 0.96 | -0.73 | 0.22 |
| 2 | 0.86 | -0.63 | 0.75 |

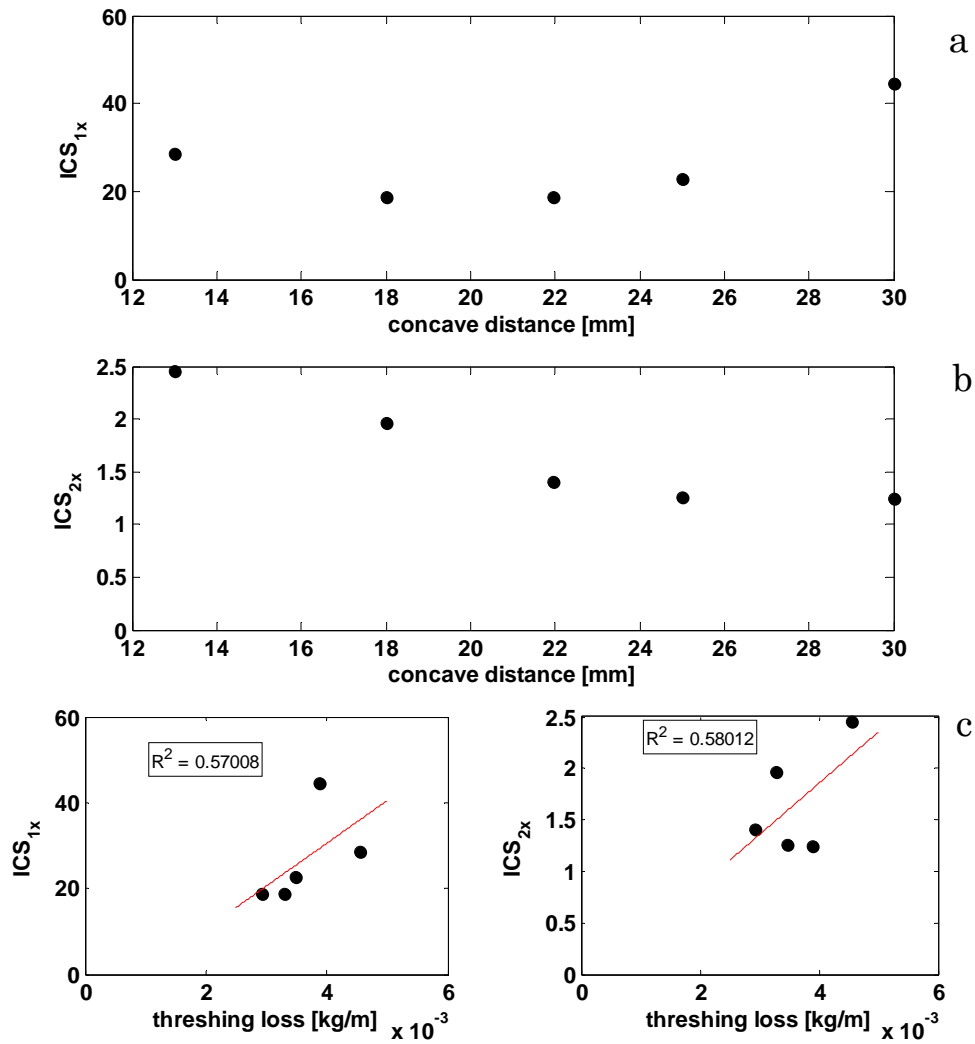


Fig. 4-32 - Efficiency parameter: threshing loss for the field nr. 1. (a) ICS_{1x} vs. concave distance, (b) ICS_{2x} vs. concave distance, (c) ICS_{1x} - ICS_{2x} vs. threshing loss with $R^2 = 0.57$ and 0.58 .

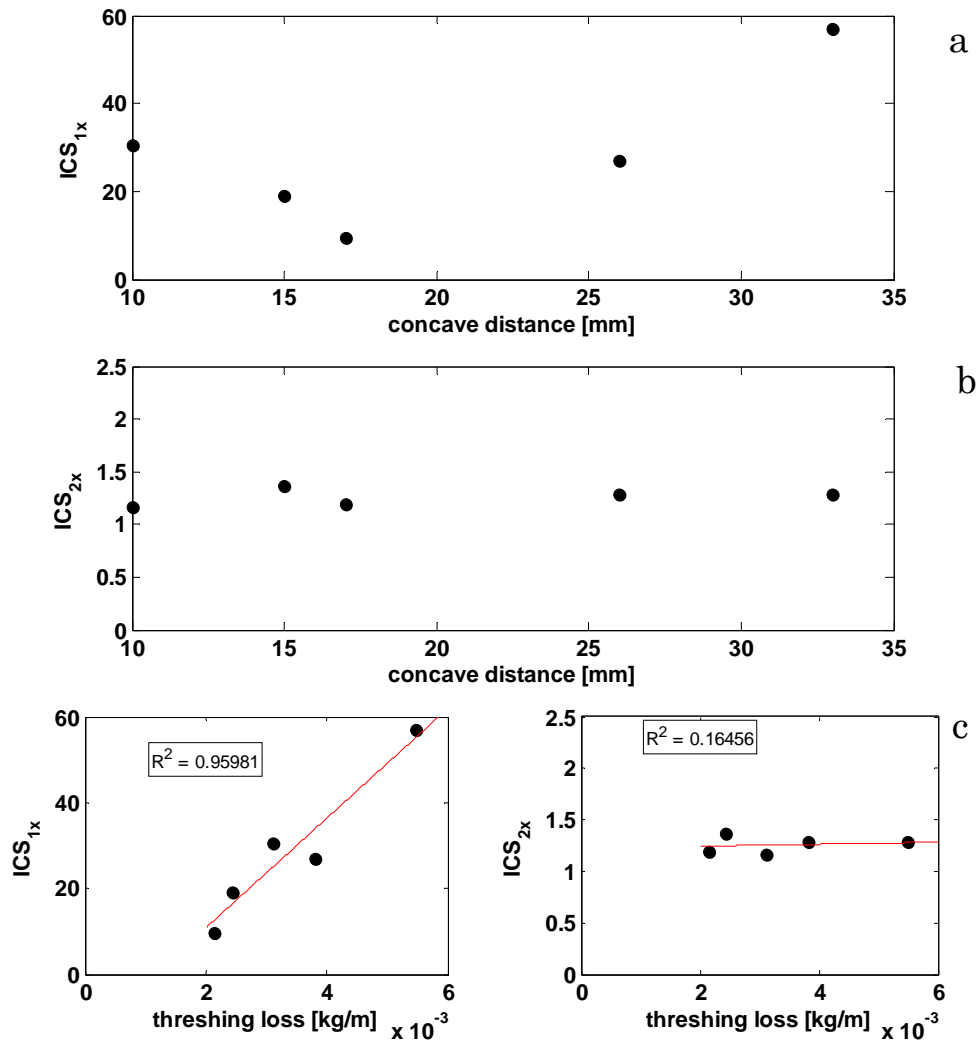


Fig. 4-33 - Efficiency parameter: threshing loss for the field nr. 2. (a) ICS_{1x} vs. concave distance, (b) ICS_{2x} vs. concave distance, (c) ICS_{1x} - ICS_{2x} vs. threshing loss with $R^2 = 0.95$ and 0.16 .

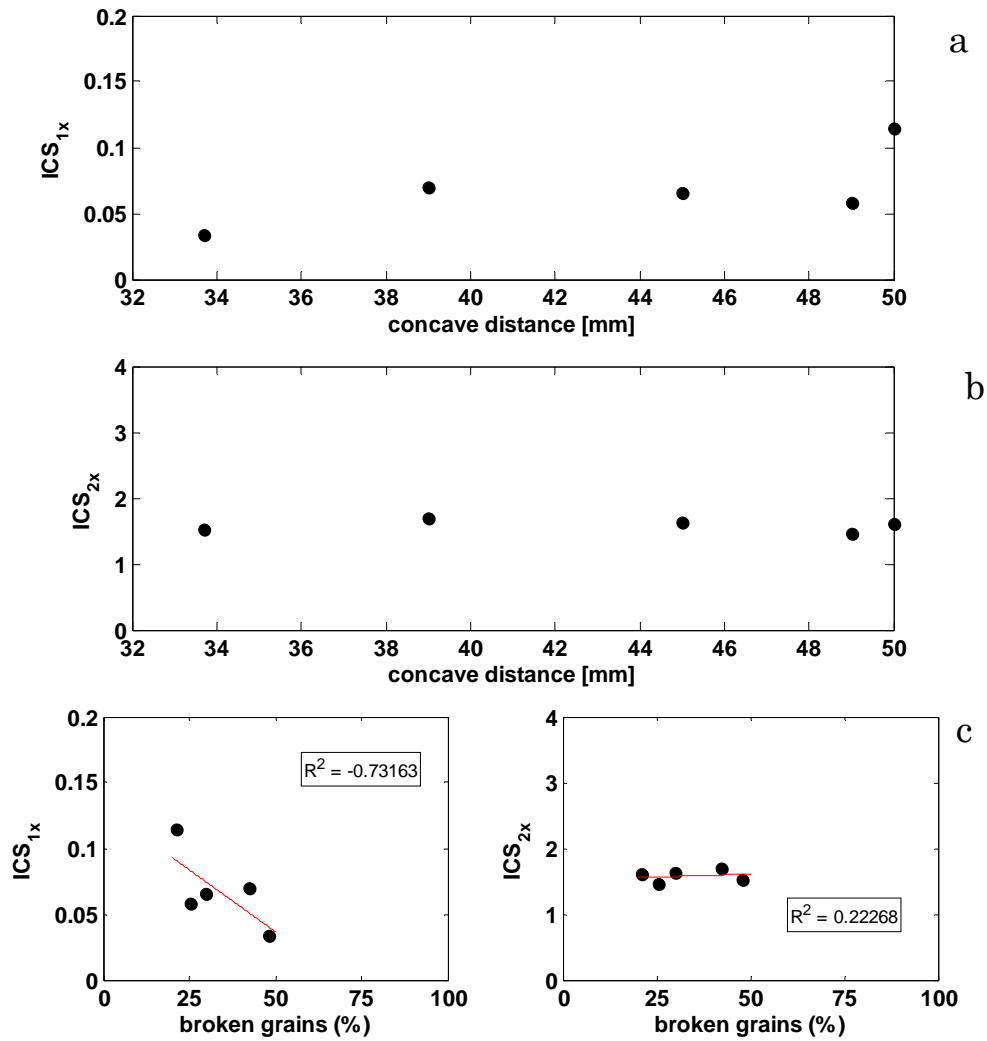


Fig. 4-34 - Efficiency parameter: threshing loss for the field nr. 1. (a) ICS_{1x} vs. concave distance, (b) ICS_{2x} vs. concave distance, (c) ICS_{1x} - ICS_{2x} vs. broken grain with $R^2 = -0.73$ and 0.22 .

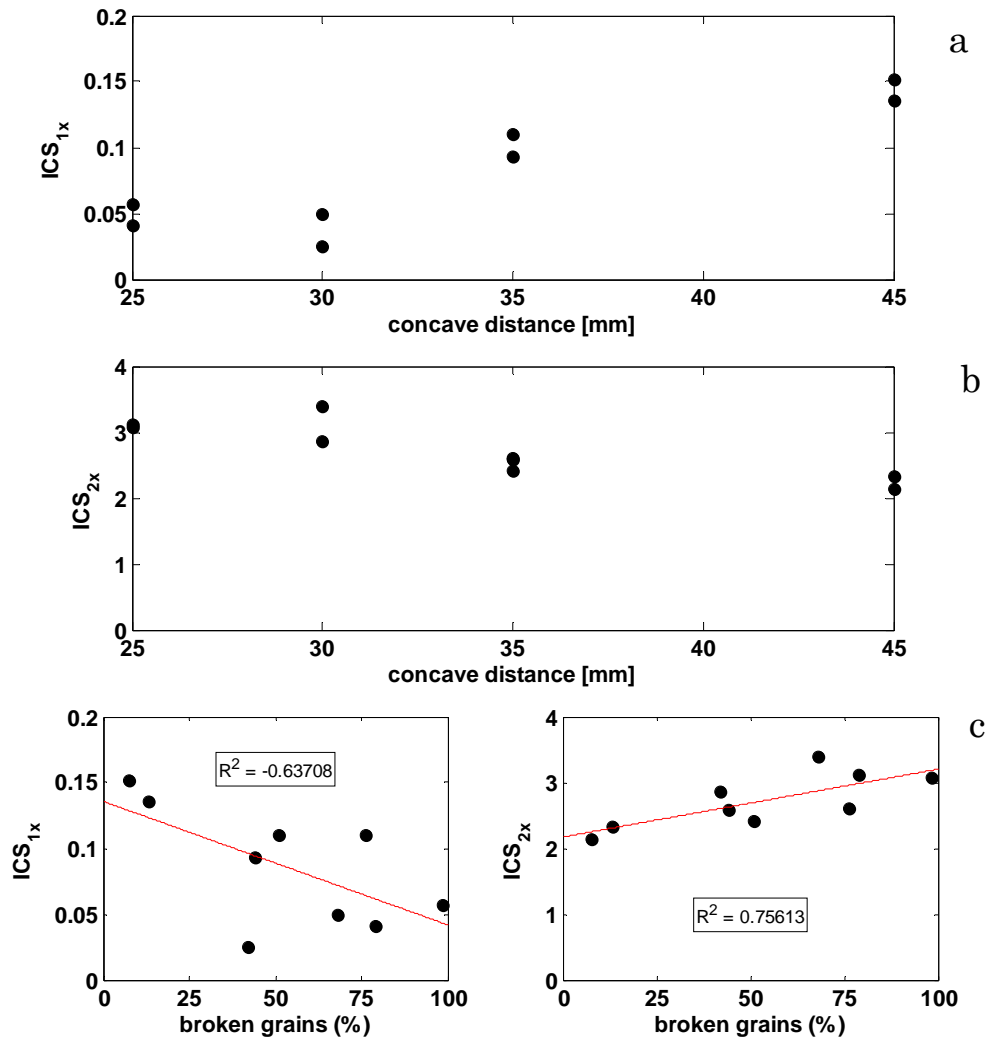


Fig. 4-35 - Efficiency parameter: threshing loss for the field nr. 2. (a) ICS_{1x} vs. concave distance, (b) ICS_{2x} vs. concave distance, (c) ICS_{1x} – ICS_{2x} vs. threshing loss with $R^2 = -0.63$ and 0.7 .

CONCLUSIONS

This thesis deals with the application of advanced signal processing techniques to the monitoring of the threshing process quality in harvesting machines by means of the extraction of indicators from vibro-acoustic signals.

The choice of the proper domain of analysis and the proper techniques has been made with the aim at give a detailed description of the vibration effects of the two main mechanisms of the threshing process influencing the threshing efficiency: (1) the threshing between kernels and concave and (2) the “grain over grain” effect.

The adopted techniques involve the analysis in the time domain and the cyclostationary approach.

Moreover several temporal and cyclostationary indicators have been extracted in order to achieve reliable correlations between vibro-acoustic signals and efficiency/operational parameters.

After a brief introduction in Chapter 1 and a description of the machine in Chapter 2, in Chapter 3 a general overview of the signal processing techniques adopted in this thesis is presented.

In particular two approaches are illustrated: time domain analysis and cyclostationary analysis. Concerning the time domain analysis the following sound metrics have been evaluated: the Loudness which is a perceptual measure of the effect of the energy content of a sound on human’s ear; the Tonality that indicates whether the sound mainly consists of tonal components or broadband noise. Both sound quality metrics have been applied over the threshing middle and cabin microphones.

Moreover, some metrics that reflect the energy (RMS) and the regularity (AppEn) of a time series have been evaluated over the concave middle radial acceleration signal.

The cyclostationary approach, adopted for the analysis of the concave middle radial acceleration signal, has been used in order to evaluate the first order cyclostationarity component of the signal through the calculation of the Time Synchronous Average (TSA) that permits to describe the concave vibration due to the rasp bar action. Then, by subtracting the TSA from the signal re-sampled in the angular domain, the residual signal, representing the second order cyclostationary part of the signal, has been obtained.

Several simple metrics such as Root Mean Square (RMS) and Indicators of Cyclostationarity (ICS_{nx}) have been calculated. The latter tries to quantify the distance of a cyclostationary process from the closest stationary process having similar power spectral density. In particular ICS_{1x} and ICS_{2x} give an indication of the presence of the first-order and second-order cyclostationarity content.

The effectiveness of all the above described techniques is verified on a synthesized signal that tries to reproduce the main characteristics of the actual signals captured on the threshing unit.

Chapter 4 deals with the application of the above mentioned signal processing techniques to the actual signals acquired during several experimental campaigns in outdoor conditions. The attention is particularly focused on the concave distance variation which is the setting that can be tuned by the user during the field operations.

A short review about the correlation between the time domain features and the operational parameters (i.e. capacity and concave distance), introduced in order to confirm the results obtained in [4] and [5], has shown that:

- About the influence of the **capacity** on the vibro-acoustic response (see Fig. 4-1), the results achieved in [4] and [5] are confirmed: only the Loudness metric is sensitive to the capacity variation showing a linear increase as the capacity increases; RMS and Tonality seem to be insensitive to this operational parameter.

- Concerning the influence of the **concave distance** (i.e. radial distance between rotor and concave), only the RMS and AppEn features (see Fig. 4-2 and Fig. 4-4), from the concave middle radial acceleration signal, show reliable correlations. On one hand, the AppEn metric confirms the trend depicted in [4] and [5]: increasing the concave distance the regularity of the time series increases giving a decrease of the AppEn. On the other hand the RMS metric better describes the results in [4] and [5] because a concavity trend is clearly visible. The excitation variation in function of the concave distance is not so manifest to be revealed by the sound quality metrics from the microphone outside the cabin.

The use of the cyclostationary approach permits to analyze the signals captured on the concave more precisely than in [4]. The concave middle radial acceleration signal is the most closely correlated to the threshing process: its first order cyclostationary component, identified by the TSA, clearly shows all the events caused by the presence of the threshing elements such as rasp bars and friction elements.

Moreover, the TSA, because of its sensitivity to the concave distance variation, could be used as reference to describe the periodical rasp bar interaction between rotor, material and concave at different concave distances. In particular, it can be concluded that:

- **At small concave distance (10 mm)** the random sliding interaction of the material with itself and the mechanical components (rotor and concave) would give a vibration signal roughly proportional to the local pressure, i.e. higher when the rasp bar is closer to the concave.
- **At middle concave distance (25 mm)** the crop layer becomes looser but the rotor has still enough grip on the crop to move the whole layer rather easily: as a consequence, lower acceleration is transferred to the concave.

- **At high concave distance (30 mm)** the rotor loses the grip on the crop and consequently it is threshed in bunches of material, not as a regular layer. When the bunch of material is thick enough to be grabbed by the rasp bar on the rotor, it is accelerated against the concave causing an increase of the acceleration amplitude.
- The **RMS** is the most reliable feature to describe the TSA signal evolution in function of the concave distance variation. A concavity trend showing a minimum RMS value is clearly visible in time and angular domains.

The second order cyclostationary component has been treated by using the cyclic power: in particular, it could be concluded that the residual part is linked to the material distribution between rotor and concave. Switching from small to high concave distances, the material distribution changes, going from a regular material layer to bunches of material. This transformation gives an increase of the amplitude modulation of the residual part.

Finally, the correlation between signal features and efficiency parameters, such as threshing loss and broken grain percentage, is described.

The efficiency parameters try to numerically describe the efficiency of the threshing process. Both threshing loss and broken grain percentage are influenced by the setting of the concave distance.

Concerning the threshing loss correlations (evaluated only for wheat field tests) it can be concluded that:

- The **temporal RMS** gives repetitive correlations but the minimum threshing loss value, corresponding to the optimal machine setting, does not correspond to the minimum RMS value.
- the **TSA RMS** value is better correlated to the threshing loss than the temporal one. The correlations obtained show a good repeatability for different field test campaigns.

- The ICS_{1x} shows good correlations to the threshing loss as found for the TSA RMS. On the other hand, the ICS_{2x} does not seem to be correlated to the threshing loss.

Observing the analysis of the broken grain percentage (evaluated for corn field tests), it can be concluded that:

- The **RMS** from the time and angular domains are well correlated to the broken grain percentage.
- The ICS_{nx} , for $n = 1, 2$, are not useful to obtain reliable correlation to the broken grain percentage.

Due to its capability in detecting both rasp bar and friction element interactions, the concave accelerometer signal can be considered more reliable than the threshing microphone in evaluating the local phenomena happening between rotor and concave. Concerning the direction it can be concluded that the concave middle radial acceleration signal is the most closely correlated to the threshing process. Moreover, the TSA RMS is the most robust indicator able to describe and predict the machine efficiency, because it is strongly influenced by the interaction between rasp bars, material and concave which is the first of the two mechanisms of the threshing process above mentioned.

Considering the presented research activity, the main original contribution of this thesis concerns the application of advanced signal processing techniques to the extraction of indicators from vibro-acoustic signals acquired in harvesting machine and the evaluation of their effectiveness in obtaining useful information for the detailed description of the threshing process mechanisms. The RMS of the angular domain signals is a very useful indicator in order to predict the efficiency of the threshing process. Thus, this parameter could be the key parameter to be implemented in a online control system able to adjust the machine setting in order to maximize the process efficiency.

References

- [1] R. B. Randall, “**State of the art in monitoring rotating machinery**”, in proceedings of ISMA 2002, Leuven, Belgium.
- [2] S. J. Braun, “**Mechanical Signature Analysis**”, Academic Press, London (1986).
- [3] McFadden P.D., “**Examination of a technique for the early detection of failure in gears by signal processing of the time domain average of the meshing vibration**”, Mechanical Systems and Signal Processing, 1987, 1:173-183.
- [4] S. Delvecchio, “**Advanced vibration processing techniques for condition monitoring and quality control in I.C. Engines and harvesting machines**”. PhD dissertation, ENDIF, Engineering Department in Ferrara, Ferrara (2009).
- [5] S. Delvecchio, S. Fiorati, B. Missotten, P. Sas, “**Vibro-acoustic analysis of the threshing process in harvesting machine**”, in proceedings of the ISMA 2010, Leuven, Belgium.
- [6] J. Antoni, “**Cyclic spectral analysis in practice**”, Mechanical Systems and Signal Processing, Vol. 21, Elsevier (2007), pp.597-630.
- [7] A. Raad, J. Antoni, M Sidahmed, “**Indicators of cyclostationarity: Theory and application to gear fault monitoring**”, Mechanical System and Signal Processing Vol. 22 (2008), pp. 574-587.
- [8] E. Zwicker, H. Fastl, “**Psycho-acoustics, Facts and Models**”, Springer, 1999.
- [9] E. Terhardt, G. Stoll, M. Seewann, “**Algorithm for extraction of pitch and pitch salience from complex tonal signals**”, The Journal of the Acoustical Society of America 71, 679-688, 1982.
- [10] W. Aures, “**Procedure for Calculating the Sensory Euphony of Arbitrary Sound Signals**”, Acustica 59, 130-141, 1985.
- [11] A. Hastings, P. Davies, “**An examination of Aures’s model of tonality**”, Internoise 2002.

-
- [12] M. Pincus, “**Approximation Entropy as a measure of system complexity**”, *proc. Natl. Acad. Sci. USA*, Vol. 88 (1991), pp. 2297-2301.
- [13] R. Yan, R. X. Gao, “**Approximate Entropy as a diagnostic tool for machine health monitoring**”, *Mechanical System and Signal Processing*, Vol. 21, Elsevier (2007), pp. 824-839.
- [14] W. A. Gardner, “**Cyclostationary in Communications and Signal Processing**”, IEEE Press (1994).
- [15] CNH, “**Non conventional harvesting machines – User manual**”.
- [16] Srivastava, Ajit K., Carroll E.Goering, Roger P. Rorhbach, and Dennis R. Buckmaster. 2006 “**Grain Harvesting**”. Chapter 12 in *Engineering Principles of Agricultural Machines*, 2nd ed., 403-436. St. Joseph, Michigan: ASABE.
- [17] Petre I. Miu, Heinz-Dieter Kutzbach, “**Modelling and simulation of grain threshing and separation in threshing unit**”, *Computers and Electronics in Agriculture*, v. 60 n.1, p. 105-109, January 2009.
- [18] J. Antoni, F. Bonnardot, A. Raad, M.El Badaoui, “**Cyclostationary modelling of rotating machine vibration signals**”, *Mechanical Systems and Signal Processing*, 2004, 18 (6), pp. 1285-1314.
- [19] F. Bonnardot, R. Boustany, A. Ibrahim, K. Sabri, J. Antoni, M. El Badaoui, “**Don’t ignore non-stationarity: use it to advantage**”, in *proceedings of the ISMA 2006*, Leuven, Belgium.



Your E-Mail Address

stefano.fiorati@unife.it

Subject

DICHIARAZIONE DI CONFORMITÀ CON RICHIESTA DI EMBARGO TESI

Io sottoscritto Dott. (Cognome e Nome)

Fiorati Stefano

nato a

Ferrara

Provincia

Ferrara

il giorno

08/09/1982

avendo frequentato il corso di Dottorato di Ricerca in:

Scienze dell'Ingegneria

Ciclo di Dottorato

XXIII

Titolo della tesi in Italiano

MONITORAGGIO DELLA QUALITÀ DEL PROCESSO DI TREBBIATURA ATTRAVERSO L'USO DI INDICATORI VIBRO-ACUSTICI AVANZATI

Titolo della tesi in Inglese

MONITORING OF THE THRESHING PROCESS QUALITY BY USING ADVANCED VIBRO-ACOUSTIC INDICATORS

Titolo della tesi in altra Lingua Straniera

Tutore - Prof:

Giorgio Dalpiaz

Settore Scientifico Disciplinare (SSD)

ING-IND/13

Parole chiave (max 10)

monitoraggio processo di trebbiatura qualità indicatori vibro acustici monitoring threshing process quality vibro acoustic indicators

Consapevole - Dichiaro

CONSAPEVOLE --- 1) del fatto che in caso di dichiarazioni mendaci, oltre alle sanzioni previste dal codice penale e dalle Leggi speciali per l'ipotesi di falsità in atti ed uso di atti falsi, decade fin dall'inizio e senza necessità di alcuna formalità dai benefici conseguenti al provvedimento emanato sulla base di tali dichiarazioni; -- 2) dell'obbligo per l'Università di provvedere al deposito di legge delle tesi di dottorato al fine di assicurarne la conservazione e la consultabilità da parte di terzi; -- 3) della procedura adottata dall'Università di Ferrara ove si richiede che la tesi sia consegnata dal dottorando in 4 copie di cui una in formato cartaceo e tre in formato .pdf, non modificabile su idonei supporti (CD-ROM, DVD) secondo le istruzioni pubblicate sul sito : <http://www.unife.it/dottorati/dottorati.htm> alla voce ESAME FINALE – disposizioni e modulistica; -- 4) del fatto che l'Università sulla base dei dati forniti, archiverà e renderà consultabile in rete il testo completo della tesi di dottorato di cui alla presente dichiarazione attraverso l'Archivio istituzionale ad accesso aperto "EPRINTS.unife.it" oltre che attraverso i Cataloghi delle Biblioteche Nazionali Centrali di Roma e Firenze. --- DICHIARO SOTTO LA MIA

RESPONSABILITA' --- 1) che la copia della tesi depositata presso l'Università di Ferrara in formato cartaceo, è del tutto identica a quelle presentate in formato elettronico (CD-ROM, DVD), a quelle da inviare ai Commissari di esame finale e alla copia che produrrà in seduta d'esame finale. Di conseguenza va esclusa qualsiasi responsabilità dell'Ateneo stesso per quanto riguarda eventuali errori, imprecisioni o omissioni nei contenuti della tesi; -- 2) di prendere atto che la tesi in formato cartaceo è l'unica alla quale farà riferimento l'Università per rilasciare, a mia richiesta, la dichiarazione di conformità di eventuali copie. --- PER ACCETTAZIONE DI QUANTO SOPRA RIPORTATO

Dichiarazione per embargo

36 mesi

Firma Dottorando

Ferrara, li 11/03/2011

Firma del Dottorando

Firma Tutore

Visto: Il Tutore Si approva Firma del Tutore